INAUGURAL - DISSERTATION

zur Erlangung der Doktorwürde
der Naturwissenschaftlich-Mathematischen Gesamtfakultät
der Ruprecht-Karls-Universität Heidelberg

Vorgelegt von
Diplom-Geoökologin Sina Muster
aus Potsdam
Tag der mündlichen Prüfung: 18. Oktober 2013

DECOMPOSING ARCTIC LAND COVER

Implications of heterogeneity and scale for the estimation of energy fluxes in Arctic tundra landscapes

Gutachter
PD Dr. Julia Boike
Prof. Dr. Lucas Menzel

Dedicated to Jan, Raika and Mara.

ABSTRACT

The rapid rate of environmental change in the Arctic alters the exchange of water, carbon, and energy fluxes between the land surface and the atmosphere with global impacts on ecosystems and climate. This thesis investigates the effect of mixed satellite signals on land cover mapping and on the estimation of latent heat fluxes, Q_E, and land surface temperature (LST) in three Arctic tundra environments in the Lena Delta (Siberia, Russia), on Bathurst Island (Canadian High Arctic), and the Barrow Peninsula (Alaska, USA). Land cover maps were derived from optical and radar remote sensing data with resolutions of 4 m or better to decompose satellite mixed pixels with resolutions of 17 m (CHRIS/PROBA) and 30 m (Landsat5-TM). Downscaling land/water cover via Landsat surface albedo increased the total water surface area of the Lena Delta from 13 % to 20 %. Ponds, *i.e.*, water bodies with a surface area smaller than 10^4 m, made over 95 % of the total number of water bodies at all sites. Water body size-distributions deviated from a power law function for ponds and very large lakes which could only be detected with high-resolution water body mapping. Maximum spatial differences of up to 22 Wm^{-2} for Q_E and 10 °C for LST were associated with fair weather perios dominated by high net radiation and little precipitation. Uncertainties of ± 35 % would arise in Landsat-based Q_E mapping, and of ± 30 % in MODIS-based LST mapping when subpixel land cover heterogeneities are not considered. Results of this thesis highlight the importance of integrating detailed field studies with multi-scale remote sensing data to determine fine-scale spatial differences in energy fluxes over larger areas in Arctic tundra landscapes. Land cover maps with spatial resolutions of 2 m or better are necessary to ensure the quality and representativeness of land cover statistics. This thesis proposes to compile improved subpixel land cover statistics in different Arctic ecosytems to facilitate upscaling of the surface energy balance as well as carbon fluxes to larger-scale grids. This is a crucial task regarding the great uncertainty associated with the global estimation of feedbacks between the Arctic surface and the atmosphere under a changing climate.

ZUSAMMENFASSUNG

Die Arktis ist ein wesentlicher Bestandteil des globalen Klimasystems. Der Austausch von Energie-, Wasser- und Kohlenstoffflüssen zwischen der Landoberfläche und der Atmosphäre wird wesentlich von den Eigenschaften der Landbedeckung bestimmt. Die vorliegende Dissertation untersucht die räumliche Heterogenität der Landoberfläche, der Verdunstung und der Oberflächentemperatur in arktischen Tundralandschaften im Lena Delta in Sibirien (Russland), auf der Insel Bathurst in der kanadischen Hocharktis und auf der Barrow Halbinsel in Alaska (USA). Die Landoberfläche wurde auf verschiedenen Skalen kartiert: räumlich hochaufgelöst mit optischen Fernerkundungsdaten und Radardaten (4 m und besser), mäßig aufgelöst mit CHRIS/PROBA (17 m) und Landsat-5 TM (30 m) und grob aufgelöst mit MODIS Satellitendaten (250 m und mehr). Die Oberflächenalbedo wurde erfolgreich genutzt, um den Subpixelanteil von Land und Wasser in Landsatpixeln abzuschätzen, wodurch sich der Wasseranteil im Lena Delta von bisher kartierten 13 % auf 20 % erhöhte. Wasserkörper mit einer Oberfläche kleiner als 10^4 m machten 95 % der Anzahl aller Wasserkörper in allen Untersuchungsgebieten aus. Die Häufigkeitsverteilungen kleiner und sehr großer Seen wichen stark von einer Potenzfunktion ab, was nur durch hochaufgelösten Kartierungen ersichtlich wurde. Es wurden maximale räumliche Unterschiede in der Verdunstung von bis zu $22\,\mathrm{Wm^{-2}}$ und in der Oberflächentemperatur von bis zu $10\,°\mathrm{C}$ gefunden. Verdunstungsabschätzungen basierend auf Landsatdaten können zu einer Unsicherheit von $\pm35\,\%$ führen, wenn die Oberflächenheterogenität innerhalb der Landsatpixel nicht berücksichtigt wird. Analog kann es in der Kartierung von Oberflächentemperaturen basierend auf MODIS zu einer Unsicherheit von $\pm30\,\%$ kommen. Die entwickelten Methoden dieser Arbeit erlauben eine verbesserte Verknüpfung von kleinräumigen Energie- und Kohlenstoffflüssen mit großräumigen Satelliten- und Modelldaten durch (i) räumlich hochaufgelöste Kartierungen (mindestens 2 m) zur Ableitung statistischer Verteilungen verschiedener Oberflächenparameter und (ii) die Integration von Feldmessungen mit multi-skaligen Fernerkundungsdaten, um die räumlichen Unterschiede in den Energieflüssen arktischer Tundralandschaften auch über größere Gebiete zu erfassen.

The author furthermore contributed to the following publications, which are not presented in this thesis:

Langer, M., Westermann, S., **Muster, S.**, Piel, K. and Boike, J. (2011): The surface energy balance of a polygonal tundra site in northern Siberia Part 1: Spring to fall, *The Cryosphere*, 5, pp. 151 171. doi: 10.5194/tc-5-151-2011.

Langer, M., Westermann, S., **Muster, S.**, Piel, K. and Boike, J. (2011): The surface energy balance of a polygonal tundra site in northern Siberia Part 2: Winter, *The Cryosphere*, 5, pp. 509 524. doi: 10.5194/tc-5-509-2011.

Boike, J., Langer, M., Lantuit, H., **Muster, S.**, Roth, K., Sachs, T., Overduin, P., Westermann, S., and McGuire, A. D. (2012). PermafrostPhysical Aspects, Carbon Cycling, Databases and Uncertainties. In *Recarbonization of the Biosphere* (pp. 159-185). Springer Netherlands.

Boike, J., Kattenstroth, B., Abramova, K., Bornemann, N., Chetverova, A., Fedorova, I., Fröb, K., Grigoriev, M., Grüber, M., Kutzbach, L., Langer, M., Minke, M., **Muster, S.**, Piel, K., Pfeiffer, E. M., Stoof, G., Westermann, S., Wischnewski, K., Wille, C. and Hubberten, H. W. (2013): Baseline characteristics of climate, permafrost and land cover from a new permafrost observatory in the Lena River Delta, Siberia (1998 2011), *Biogeosciences*, 10 (3), pp. 2105– 2128. doi: 10.5194/bg-10-2105-2013.

Cresto Aleina, F., Brovkin, V., **Muster, S.**, Boike, J., Kutzbach, L., and others: A stochastic model for the polygonal tundra based on Poisson-Voronoi Diagrams, *Earth System Dynamics Discussion*, 3, 453-483, doi:10.5194/esdd-3-453-2012, 2012.

Yi, S., Wischnewski, K., Langer, M., Muster, S., and Boike, J. (2013). Modeling different freeze/thaw processes in heterogeneous landscapes of the Arctic polygonal tundra using an ecosystem model. *Geoscientific Model Development*, submitted.

ACKNOWLEDGMENTS

CONTENTS

LIST OF TABLES

SYNOPSIS

1.1 INTRODUCTION

1.1.1 *Arctic land cover under a changing climate*

The Arctic is warming at a rate twice as fast compared to the global temperature increase (Hinzman et al., 2005; ACIA, 2005; Parry, 2007; AMAP, 2011) which affects both the Arctic land surface as well as the thermal state of permafrost. Permafrost occupies approximately 24 % of the Northern Hemisphere land area (Brown et al., 1997) and stores about 50 % of the estimated global belowground organic carbon pool (Tarnocai et al., 2009). Permafrost is perennially frozen ground that remains at or below 0 °C for at least two consecutive years (French, 2007). According to model projections, permafrost degradation will affect almost half of the current permafrost area in the northern hemisphere by 2100 (ACIA, 2005). Wetting (Jorgenson et al., 2001; Smith et al., 2005; Watts et al., 2012) and drying of the surface (Yoshikawa and Hinzman, 2003; Smith et al., 2005; Riordan et al., 2006; Carroll et al., 2011) are examples of land surface changes due to permafrost degradation. Other observed land cover changes are the greening of the Arctic which comprises the lengthening of the snow-free season (Chapin et al., 2005), and increases in plant biomass due to shrub and tree expansion (Sturm et al., 2001; Jia et al., 2003; Tape et al., 2006).

The Arctic land surface plays a critical role in the exchange of water, carbon, and energy fluxes between the land and the atmosphere in the Arctic climate system (Chapin III et al., 2000). Some land cover types may be "hot spots" with high process rates that make them more important than their areal extent would suggest (Chapin III et al., 2012). Thaw ponds in Arctic wetlands, for example, have been recognized as hot spots of biological activity (Smol and Douglas, 2007), carbon dioxide (Laurion et al., 2010; Abnizova et al., 2012) and methane emissions (Laurion et al., 2010; Walter et al., 2006). Hot spots may shift due to changes in land cover and alter feedbacks between the land surface and the atmosphere. Increasing surface wetness amplifies high-latitude methane fluxes causing a positive feedback to climate warming (Walter et al., 2006). Similarly, surface drying and a change in dominance from mosses to vascular plants would enhance sensible heat flux and regional warming in tundra (Chapin III et al., 2000). Assessing changes in water, carbon, and energy fluxes between the land and the atmosphere due to a warming climate is therefore inextricably linked with mapping and monitoring land cover.

1.1.2 *Arctic land cover heterogeneity*

The current land surface in the Arctic is the result of past and current feedbacks between climate, local soils and topography, and permafrost. The interplay between water, permafrost and intense freeze-thaw processes create land cover patterns that are highly heterogeneous. Pro-

cesses like frost heave, thaw settlement, as well as contraction and expansion due to temperature changes have caused the formation of microtopography in otherwise flat terrains (French, 2007). Drainage is impeded by the underlying permafrost and water accumulates in cracks and depressions resulting in water-saturated soils or inundated areas whereas raised topographies like hummocks and ridges feature comparatively dry surfaces. Land cover may thus change over the range of a few decimeters in hummocky terrain or over the range of a few meters such as in polygonal tundra landscapes (Fig. 1). Heterogeneity is a function of scale, which is described via the factors grain and extent (Turner et al., 2001). In spatial analysis, grain refers to the minimum patch size of vector data or the pixel size of raster data. Extent is the area encompassed by a study. The extent and resolution of remote sensing imagery is specific to each remote sensing platform and sensor. The degree of heterogeneity of remotely sensed land cover therefore depends on the image scale in relation to the size, shape, and spatial distribution of land cover patches in the landscape (Chapin III et al., 2012). Structural heterogeneity considers the complexity of land cover patterns without reference to any functional effects (Kolasa and Rollo, 1991) while functional heterogeneity refers to the complexity of land cover that can be shown to affect biogeophysical or biogeochemical processes like latent heat fluxes or surface temperature.

1.1.3   *Remote sensing of Arctic land cover and energy fluxes*

Remote sensing offers an invaluable tool to map and monitor land cover and specific land cover properties in the vast and remote regions of the Arctic on a global scale. In order to use land cover classifications for the estimation of energy fluxes, however, two challenges have to be met:

- assessing the impact of individual land cover types on landscape-scale fluxes, and

- understanding the effect of subpixel land cover composition on mixed satellite signals.

1.1.3.1   *Challenge 1: Assessing the impact of individual land cover types on landscape-scale energy fluxes*

The land surface can be grouped into land cover classes. In natural landscapes, land cover classes include different types of vegetation, bare soil and rock, ice, and water, each characterized by a unique ensemble of biophysical attributes. Land surface characteristics that control the surface energy balance are the surface albedo, emissivity, roughness length, near-surface moisture, and vegetation type (Dickinson, 1983; Pitman, 2003). The surface energy balance describes the partitioning of the available net radiation into the sensible and latent heat flux and the ground heat flux (Dickinson, 1983).

   Changes in land cover alter surface controls over the energy fluxes and may thus cause changes in the surface energy balance. The surface energy balance of a landscape can be measured through spatially distributed points measurements in individual land cover types or through micrometeorological methods that deliver spatially averaged

fluxes for a specific footprint area. Sampling designs for both approaches need to consider the land cover composition as well as the existence and distribution of hot spots in order to measure representative landscape-scale fluxes. Land cover composition and associated spatial differences in the surface energy balances are unknown for the majority of the Arctic land surface. The knowledge of the spatial differences in energy fluxes, however, is invaluable for the validation of regional and global climate and ecosystem models. Land surface schemes in most state-of-the-art coupled general circulation models include only considerably simplified descriptions of land surface processes and properties . They generally neglect the effects of sub-grid variability in land cover, which may have a strong influence on large-scale estimations of energy fluxes (Boike et al., 2012).

1.1.3.2 *Challenge 2: The mixed pixel problem*

Satellite sensors with global coverage have resolutions of 1 km or more and cannot resolve the land cover pattern typical for Arctic tundra landscape but instead aggregate the land cover present in the pixel to some mixed type. Mixed pixels are raster elements that contain more than one land cover type (Fig. 1). The classification of mixed pixels leads to inaccuracies in the land cover classifications due to two types of errors, *i.e.,* the allocation error and spectral confusion. Allocating the pixel to one of these classes automatically creates a partial error where the assigned class is overestimated and the neglected classes are equally underestimated (Foody, 2002). Spectral confusion occurs when the spectral signature of the mixed pixel does not actually match any of the spectral signatures within that pixel. The problems associated with the classification of mixed pixels can be circumvented by unmixing procedures, where the mixed pixel is decomposed into its subpixel land cover fractions. The most common and well established unmixing method is the spectral mixture analysis (SMA) which models the mixed spectrum as a linear or nonlinear combination of its spectral endmembers, *i.e.*"pure" spectra of land cover types (Somers et al., 2011). SMA relies on the proper selection of endmembers (Roth et al., 2012). Endmember collection in Arctic regions, however, is complicated due to the lack of homogeneous pixels in remote sensing imagery and increasingly so with coarsening pixel size and extent. The sparse field measurements available cannot account for the spatial and temporal variation of endmember variability. Mapping and monitoring subpixel land cover on the pan-arctic scale would therefore benefit from more simple and robust unmixing approaches that are effective over a wide range of landscape types and can be standardized across platforms and scales.
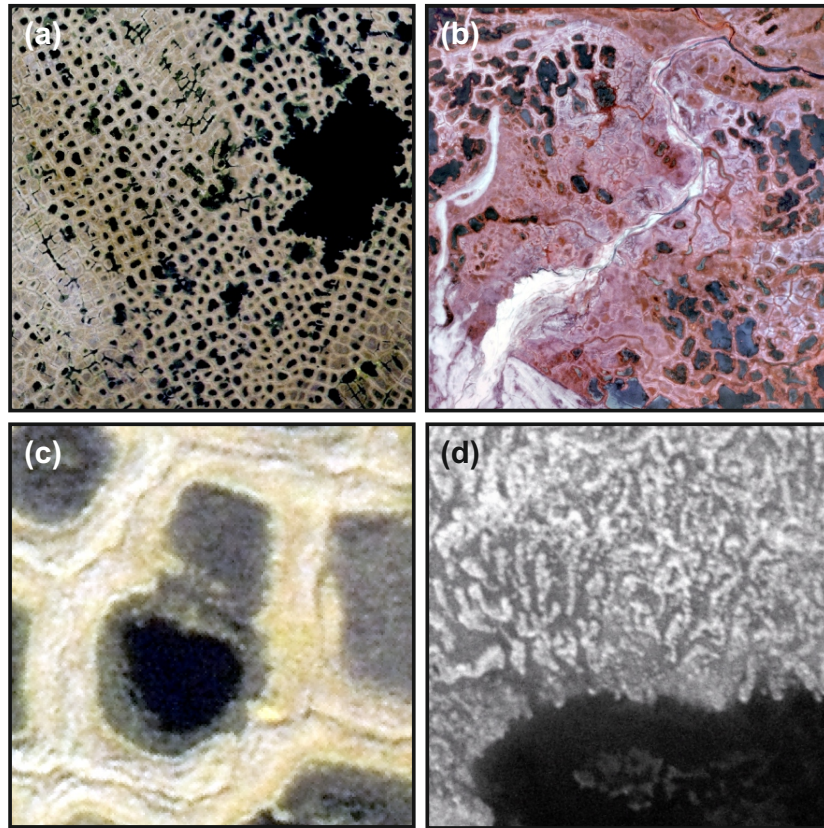
Figure 1: Land cover heterogeneity of mixed pixels on (a, c) Samoylov Island, Lena Delta, Siberia and in (b, d) Polar Bear Pass, Bathurst Island, Canada. Top images show an extent of 10^4 m² and bottom images show an extent of 30 m². (a, c) In the visible aerial photo light colored areas are dry tundra on raised rims. Wet tundra in depressed polygon centers appears darker and open water is black. (b) The landscape of Polar Bear Pass is shown in a false-color infrared aerial photograph from 1973. At the right-hand side both low- and high-centered polygons can be seen. Red areas indicate vegetation whereas white areas feature bare ground. Dark patches are open water bodies. (d) Zooming in on wet tundra at PBP reveals the structure of earth hummocks. Vegetation on theses raised mounds is comparatively dry and appears in lighter colors in the near-infrared image. Darker areas indicate wet vegetation and wet bare soil. The black area in the bottom is part of a pond.

1.1.4 *Research goals and outline*

This thesis aimed to contribute to an improved parameterization of Arctic land cover in global climate modeling and monitoring schemes. This was done through the investigation of both the structural and functional heterogeneity of land cover in three Arctic tundra landscapes in Northern Siberia, the Canadian High Arctic and Northern Alaska. The inter-comparison of different Arctic tundra landscapes allowed for the characterization of ecosystem-specific differences of heterogeneity. Detailed field measurements were integrated with multiscale and multi-sensor remote sensing data in order to assess land cover heterogeneity on multiple scales. Scale involves extents ranging from the plot scale with an extent of 1 m^2, to the regional scale with extents of 100 km^2 or more, as well as resolutions ranging from 0.2 m to 1.7 km.

The following research goals focused on the structural land cover heterogeneity:

- Quantifying structural land cover heterogeneity and the mixed pixel effect on multiple scales (Chapter 2, 3 and 4).

- Investigating the effect of resolution on water body size-distributions (Chapter 3).

- Exploring the use of surface albedo to retrieve the subpixel land/water fractions of Landsat mixed pixels (Chapter 3).

Two case studies assess the functional land cover heterogeneity with regard to latent heat flux and surface temperature:

- Investigation of spatial and temporal variations of latent heat fluxes at the Siberian polygonal tundra site (Chapter 2).

- Investigation of spatial and temporal variations of surface temperature in the Canadian High Arctic (Chapter 4).

1.2 STUDY AREAS

This thesis focused on three Arctic tundra landscapes: the Lena Delta in Siberia in Russia, Bathurst Island in the Canadian High Arctic and the Arctic coastal plain near Barrow, Alaska, USA (Fig. 2). All three regions are characterized by continuous permafrost and feature peat-forming lowland wetlands. Regional climates are characterized by long, dry, cold winters and short, moist, cool summers, with Bathurst Island exhibiting the coldest and driest climate of the study areas (Chapter 3, Table 6). The snow-free period for the Barrow pensinula and Samoylov Island lasts from mid-June to mid-September, but is much shorter at PBP from mid-July until the end of August.

The Lena River Delta is located in the far north of eastern Siberia. The north-western part of the delta is characterized by sandy sediments with a low ice content. It shows little polygonal relief but features many large thermokarst lakes and is classified as sedge, grass, moss wetland by the Circum-Arctic Vegetation Map (CAVM) (Walker et al., 2005). The southern, central and eastern part of the Delta is mainly characterized by ice-wedge polygonal tundra together with large thermokarst lakes and active flood plains. It features relatively

ice-rich sediments and is classified as sedge, moss, dwarf-shrub wetland (Walker et al., 2005). Polygonal tundra represents about 30 % of the Lena River Delta's land surface (Muster et al., 2012). Field measurements and high-resolution land cover mapping were conducted in the polygonal tundra on Samoylov Island which is located in the central part of the Delta about 120 km south of the Arctic Ocean (72° 22′ N, 126° 30′ E). Polygonal tundra is composed of elevated dry polygonal rims interspersed with wet depressed polygonal centers and numerous small polygonal ponds. A few high-centered polygons are typically found along lake margins and on elevated plateaus (Fig. 3a).

Bathurst Island in the Canadian High Arctic (75° 40′ N, 98°30′ W) features sparsely vegetated barren surfaces, graminoid tundra, and prostrate dwarf-shrub, herb tundra (Walker et al., 2005). Locally, however, topography favors the development of wetlands which are similar to the sedge, grass, moss wetlands in the Lena Delta and on the Barrow Peninsula (Fig. 3b). The wetland area of Polar Bear Pass is the largest contiguous wetland on the island with a surface area of about $86.8 * 10^6$ km². It is a shallow valley running east-west across south-central Bathurst Island. The valley is bordered by hills reaching about 240 m above sea level. Runoff from the adjoining hillslopes moves both water and matter into the wetland zone, creating an unusually productive habitat within a polar desert environment (Woo and Young, 2006).

The Barrow study area is located about 10 km south of Barrow on the Arctic Coastal Plain of northern Alaska (71° 15′ N, 156° 33′ W) (Fig. 14). The CAVM classified the peninsula like the Lena Delta as sedge, grass, moss wetland (Walker et al., 2005). The landscape is characterized by polygonal terrain, shallow, oriented thaw lakes, and drained thaw lake basins (Fig. 3c). Drained thaw lake basins of various age cover about 50 % of the surface (Hinkel et al., 2003). Young drained basins are characterized by partially flooded non-polygonal tundra. As basins age, polygonal ground develops covering about 65 % of the land surface including high- and low-centered polygons that can range from a few meters to more than 30 m in diameter (Brown et al., 1980).

Figure 2: Location of study areas in the Arctic. The Lena Delta in Northern Siberia (Russia) Bathurst Island (Canadian High Arctic), and Barrow Peninsula on the Alaskan coastal plain (USA). Map shows the major terrestrial ecozones (Modified from the Global Land Cover 2000 database (Boike et al., 2012)).
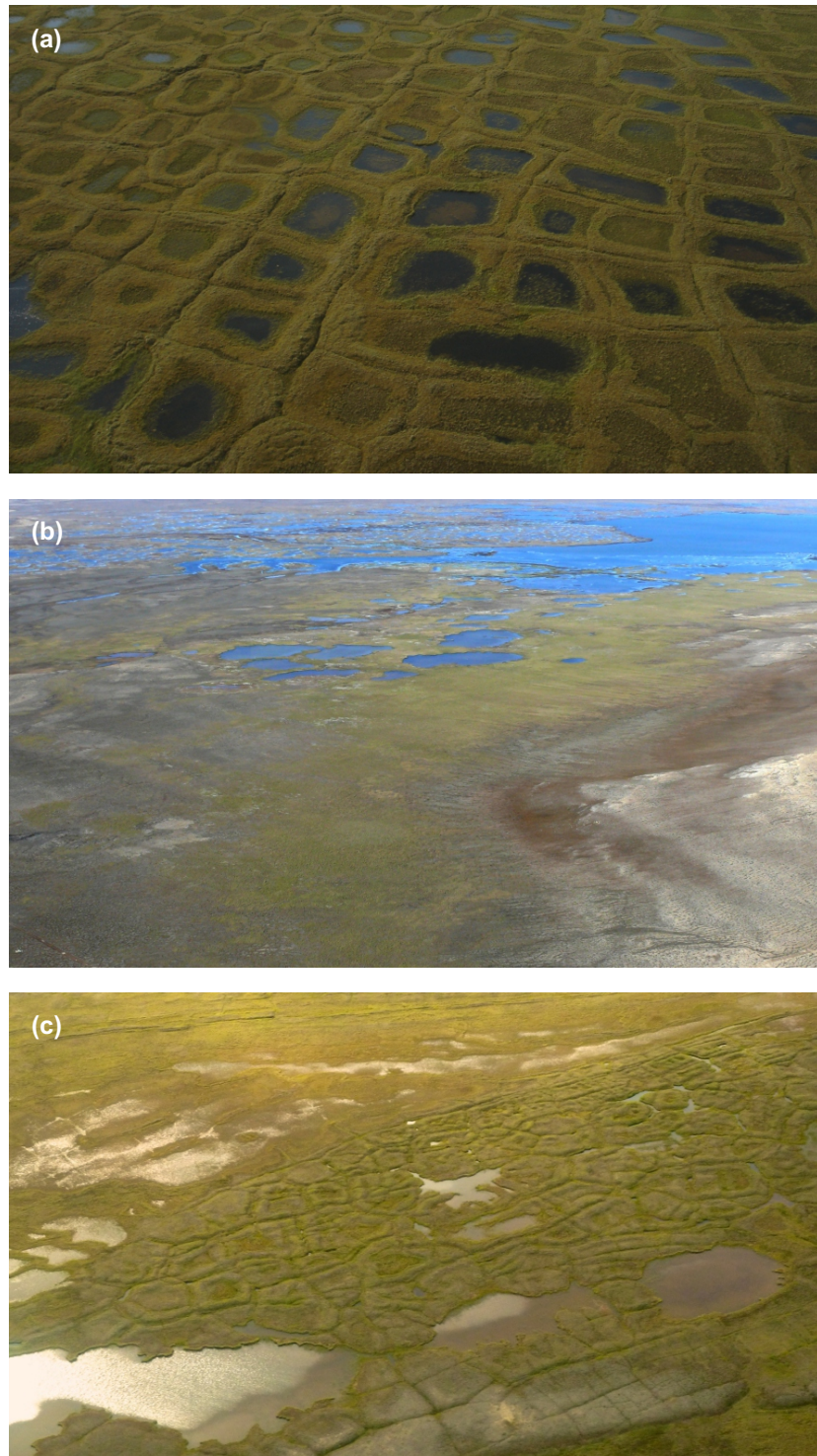
Figure 3: Aerial views of the investigated landscapes. (a) Polygonal tundra on Samoylov Island. Polygons feature an average diameter of 10 m (Photo: Niko Bornemann, AWI). (b) Polar Bear Pass wetland area with adjoining barren ridges on the left. Foremost lakes are about 30 m in diameter. (c) Polygonal and non-polygonal terrain on the Barrow Peninsula. Polygons feature an average diameter of 10 m (Photo: David Graham (ORNL), 2012, DOE Next-Generation Ecosystem Experiments in the Arctic).

Plot-scale field measurements were linked to land cover classifications (LCC) derived from remote sensing imagery with high (4 m or better), medium (30 m) and coarse (250 to 1000 m) resolutions. Field measurements and remote sensing imagery overlapped spatially and whenever possible also temporally. Figure 4 shows the workflow across scales. The workflow from field mapping to multi-resolution LCC is common to all three case studies.
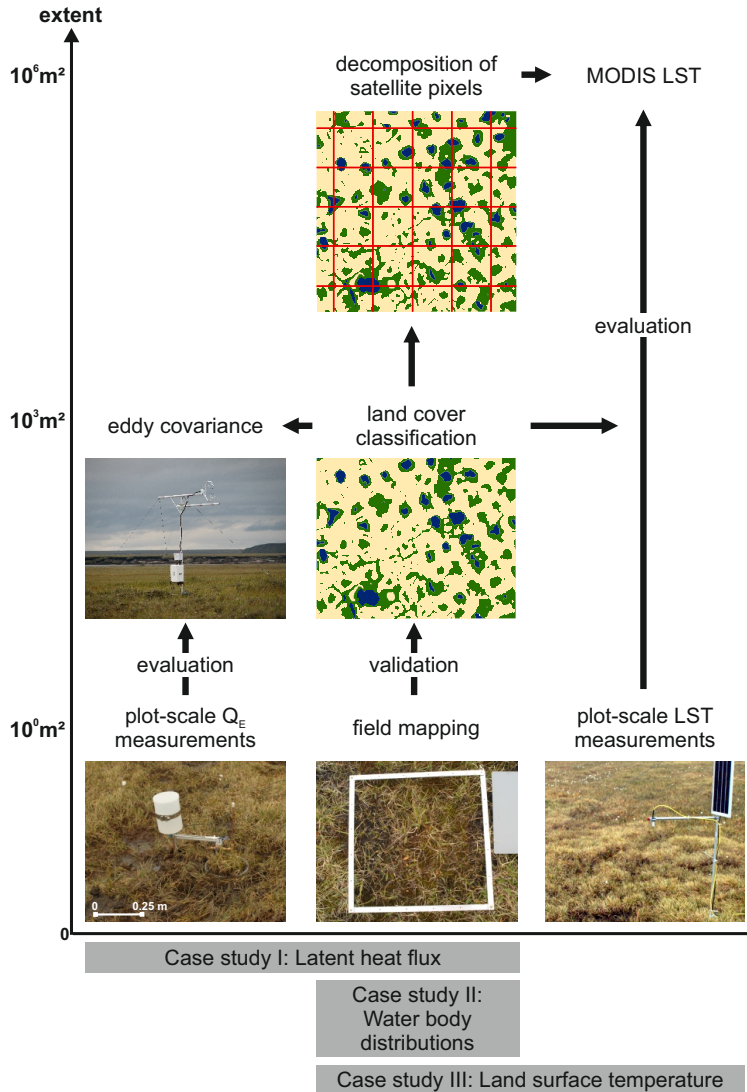
Figure 4: Diagram of multi-scale approach. Plot-scale latent heat flux, Q_E, and land surface temperature (LST) measurements were compared to spatially aggregated measurements. The workflow from field-based land cover mapping to high-resolution land cover classification and satellite pixel decomposition is common to all three case studies.

1.3.1   *Remote sensing imagery*

This study used a variety of aerial and satellite sensors to map land cover at differing spatial scales including both optical sensors and synthetic aperature radar (SAR) (Table 1). Sensor selection depended on the availability and the areal coverage of the imagery. High-resolution land cover maps, *i. e.*, with resolutions of 4 m or better, were obtained from aerial images, Kompsat-2 and TerraSAR-X. Cameras mounted on unmanned aerial vehicles (UAV) provided images with sub-meter resolutions. They were not affected by clouds but their coverage was limited due to their small field-of-view (FOV). Frequent cloudy conditions in the Arctic prevent reliable acquisitions of high-resolution imagery from optical satellites. Synthetic aperture radar like TerraSAR-X is capable of penetrating clouds and provides high-resolution imagery with a large coverage. However, their multi-spectral resolution still surpasses SAR imagery in terms of land cover classification. TerraSAR-X imagery has been successfully used to distinguish between open water, bare soil and vegetated areas but full-range land cover classifiactions of Arctic terrain are still experimental (Banks et al., 2012; Regmi et al., 2012).

Medium-resolution satellite imagery included data from the Landsat and CHRIS Proba platforms. Landsat combines a medium resolution of 30 m with a large coverage of 185 km². Its seven spectral bands include one in the thermal region. Its historic archive dates back to 1972 and is now freely available which makes Landsat a great tool for regional land cover monitoring and long-term change detection. The Landsat repeat cycle, however, does not allow the assessment of daily or weekly land surface developments. The level 3 product of the Moderate Resolution Imaging Spectroradiometers (MODIS) provides land surface temperature (LST) measurements of the Arctic land surface up to four times a day. It has a global coverage but a coarse spatial resolution of about 1 km.

PLATFORM	SENSOR	SWATH WIDTH [km]	SPATIAL RESOLUTION [m]	REPEAT CYCLE [d]	NUMBER OF BANDS: SPECTRAL RANGE [μm]
UAV	Nikon D200		$0.18 - 0.3$	24	4: 0.33 to 1.2
TerraSAR-X	TerraSAR-X	30	2	11	1: $3.1 * 10^4$
Kompsat-2	Multi-Spectral Camera (MSC)	15	4	3	4: 0.45 to 0.85
PROBA-1	Compact High Resolution Imaging Spectrometer (CHRIS)	13	17	7	18: 0.415 to 1.05
Landsat	Thematic Mapper (TM)	185	30	8	7: 0.45 to 2.35
Terra & Aqua	Moderate Resolution Imaging Spectroradiometer (MODIS)	2330	1000	< 1	36: 0.412 to 14.235

Table 1: Characteristics of applied remote sensing imagery. Unmanned aerial vehicles (UAV) included helium-filled blimps, kites and drones.

1.3.2 *Scaling land cover*

Remote sensing imagery was classified in ENVI v4.7 and v4.8 (ITTVIS) using pixel-based classification techniques (Table 2). In the case of case study III (Chapter 4), the Northern Land Cover Classification (NLCC) by Olthof et al. (2008) was used.

Remote sensing imagery and derived LCC were integrated into ArcGIS v10 (ESRI). High-resolution LCC were used to quantify the subpixel land cover composition of Landsat and MODIS imagery. Data were vectorized so that subpixel land cover fractions could be extracted for each Landsat and MODIS pixel. This allowed for the quantification of homogeneous and mixed pixels in Landsat and MODIS data as well as for the investigation of subpixel land cover heterogeneity on mixed spectral signals.

IMAGERY	LAND COVER CLASS	APPLIED METHOD	CHAPTER
Aerial imagery	wet, and dry tundra, overgrown water	supervised maximum likelihood	2
Aerial imagery	open water	NIR threshold	2 & 3
Kompsat-2	open water	NIR threshold	3
TerraSAR-X	open water	HH threshold	3
Landsat & CHRIS/PROBA	open water, bare areas, and tundra types	unsupervised *k*-means	2

Table 2: Applied classifications methods. Further information about classification validation and accuracy can be found in the indicated chapters.

1.3.3 *Scaling latent heat fluxes*

Case study I assessed spatial differences in latent heat flux, Q_E, for a polygonal tundra landscape in the Lena Delta in Northern Siberia using plot measurements and eddy covariance measurement (Chapter 2). Q_E was measured with manual and automated weighing lysimeters along a 1 km transect at seven wet polygon centers and ten dry polygon rims. Q_E from polygonal ponds, *i.e.,* water bodies smaller than 0.1 ha, were estimated using a flux gradient approach based on the difference between the specific humidity at the measurement height, $q(z_m)$, and at the water surface, $q(z_{surf})$:

$$Q_E = \frac{-\rho_{air} L_v}{r_a} (q(z_m) - q(z_{surf})), \tag{1}$$

where ρ_{air} is the density of air, L_v is the latent heat of vaporization and r_a is the aerodynamic resistance (Garratt, 1994).

The specific humidity at a saturated surface, $q(z_{surf})$, was inferred from measured temperatures of the water surface, T_{surf}, using the Magnus formula, which gives the water vapor pressure over a water surface (Sonntag, 1990). The specific humidity of air, $q(z_m)$, at the measuring height, $(z_m = 2\,m)$, is calculated from the air temperature, T_{air}, applying the Magnus formula in combination with the relative humidity, RH, at the measuring height.

Plot measurements were upscaled to eddy covariance measurements and the total mapped extent of polygonal tundra by averaging the plot-scale fluxes weighted with their respective surface fraction.

The total latent heat flux, $Q_{E,total}$, over *i* land cover types was calculated using

$$Q_{E,total} = \sum \left(A_i \times Q_{E,i} \right), \tag{2}$$

where A_i is the total areal fraction of land cover type *i*, and $Q_{E,i}$ is the latent heat flux per unit area from the land cover type *i*. Areally weighted plot-scale measurements of Q_E for the eddy footprint were then compared to the measured eddy covariance data.

1.3.4 *Scaling land surface temperature*

MODIS land surface temperature (LST) was used to investigate spatial and temporal differences in summer LST for three consecutive years in the Polar Bear Pass watershed on Bathurst Island in the Canadian High Arctic (Chapter 4). Ground-based LST measurements were conducted over a patch of wet tundra. However, a completely homogeneous MODIS pixel with a subpixel ratio of 100 % wet tundra did not exist. MODIS LST was evaluated by comparing *in-situ* radiometer measurements over wet tundra to a MODIS pixel composed of 70 % wet tundra and 30 % sparsely vegetated and water surfaces. The effect of subpixel land cover heterogeneity on MODIS LST was estimated by studying the case of a binary mixed pixel composed of the land cover classes *wet sedge* and dry *bare soil* according to the Northern Land Cover Classiciation (NLCC). Emissivity values of 0.963 for *wet sedge* and 0.977 for *bare soil* were chosen. Radiances were calculated

separately for each land cover fraction within the MODIS pixel and subsequently summed to an aggregated radiance according to Kirchhoff's law

$$L_{out} = \epsilon \sigma_{sb} T_{surf}^4 + (1 - \epsilon) L_{in} \,. \tag{3}$$

where L_{out} is the outgoing long-wave radiation (Wm^{-2}), σ is the Stefan-Boltzman constant ($5.67 * 10^{-8}$ Wm^{-2}K^{-4}), T is the absolute temperature (K), and ϵ is the surface emissivity. Inverting equation 3 with the aggregated radiance and an average emissivity yields the aggregated MODIS surface temperature which is compared to the plot-scale temperature.

MODIS LST spatial variation was assessed by comparing MODIS pixel with a comparatively homogeneous subpixel land cover composition including *wet sedge, bare soil, barren, open water* surfaces and a mixed type composed to equal parts of *wet sedge, wetland*, and *open water*.

1.4 MAIN RESULTS AND DISCUSSION

1.4.1 *Structural land cover heterogeneity*

Land cover fractionation was highest for polygonal tundra, *i.e.*, land cover types appeared in small patches and alternated over a range of a few meters. Mean patch size in polygonal tundra on Samoylov Island was 22.5 m² for *wet tundra*. Wet tundra surfaces in non-polygonal tundra on Bathurst Island were dominated by patch sizes larger than 10^4 m². Similar to polygonal tundra, microtopography modified the overall landscape units but over distances of 10 to 100 m rather than a few meters. Ponds were a common feature in both polygonal and non-polygonal wet tundra surfaces. Ponds located in non-polygonal tundra at PBP were largest with a mean patch size of 364 m² compared to polygonal ponds on the Barrow Peninsula with 177 m² or on Samoylov Island with 71 m². Image resolutions of 4 m or better were necessary to map the polygonal pattern as well as ponds in non-polygonal wetland complexes.

Satellite sensors like Landsat with a resolution of 30 m cannot resolve the land cover patterns of these landscapes (Chapter, 2, Fig. 12). The proportion of Landsat mixed pixels in polygonal tundra on Samoylov Island was 90 %. The same spectral signature of a mixed pixel may result from various combinations of the underlying subpixel land cover composition. This is likely due to the spectral similarity between the land cover classes *wet tundra* and *overgrown water*. Nevertheless, Landsat *k*-means classes showed a clear linear trend of the subpixel land/water ratio. The method was further developed and Landsat spectral groups could be related to the surface albedo (Chapter 3, Fig. 21). The relationship between Landsat albedo and subpixel water cover (SWC) appeared linear for mixed pixels of all sites, which is why similar results can be expected in other Arctic tundra environments. However, separate analyses of landscape subtypes like polygonal terrain and vegetated, drained thaw lake basin on the Barrow Peninsula indicate that the albedo-SWC relationship requires regional calibration.

While unmixing methods estimate only the subpixel-scale areal land cover fractions, probability distribution functions (PDF) describe land cover variability in statistical terms, *i. e.*, the mean, standard deviation and skew of *e. g.*, patch size or the surface roughness. Correct and representative land cover statistics strongly depend on the quality and resolution of the land cover classification. Abundance-size distributions of water bodies, for example, that were derived from high-resolution LCC showed a curved pattern on a log-log scale (Chapter 3, Fig. 17). The specific shape of the distribution was not apparent in Landsat- and MODIS-based water body size distributions due to the omission of small water bodies. As a result, Landsat- and MODIS-based water body size distributions could be mistaken to follow a power law function which would lead to a large overestimation of the number of small water bodies.

State-of-the-art global land cover maps like ECOCLIMAP (Masson et al., 2003) or the Global Land Cover Classification 2000 (GLC2000) (Bartholomé and Belward, 2005) are used to represent the land surface in the soil-vegetation-atmosphere transfer schemes of meteorological and climate models. Naturally, these land cover maps with resolutions of 1 km do not account for the fine-scale land cover heterogeneity. Moreover, land cover types in the polar regions are attributed with a low plant cover. Within ECOCLIMAP most of the Lena Delta is classified as *polar open shrubland* which is defined as shrub cover of more than 10 % and less 40 % with shrubs less than 2 m in height (Fig. 5a). The remaining cover is either barren or of annual herbaceaous type (Hansen et al., 2000). In GLC2000 the wetland is described as sparse vegetation with less than 15 % plant cover (Fig. 5b). Both classifications do not account for the extensive moss cover which is characteristic for Arctic tundra regions and plays a key role in the vertical and horizontal exchange of water, energy, and carbon fluxes in Arctic tundra environments (Blok et al., 2011). It remains an open question whether or not the wrong parameterization of plant cover in Arctic tundra landscapes impairs the derivation of land surface properties and consequently the estimation of surface energy fluxes.

Lena Delta, Siberia, Russia

Bathurst Island, Nunavut, Canada

Ecoclimap

- polar closed shrubland
- polar open shrubland
- bare soil with sparse polar vegetation
- subpolar wetlands
- water

GLC2000

- shrub cover, closed-open, deciduous
- sparse herbaceous or sparse shrub cover
- regularly flooded shrub and/or herbaceous cover
- bare areas
- water
- snow and ice
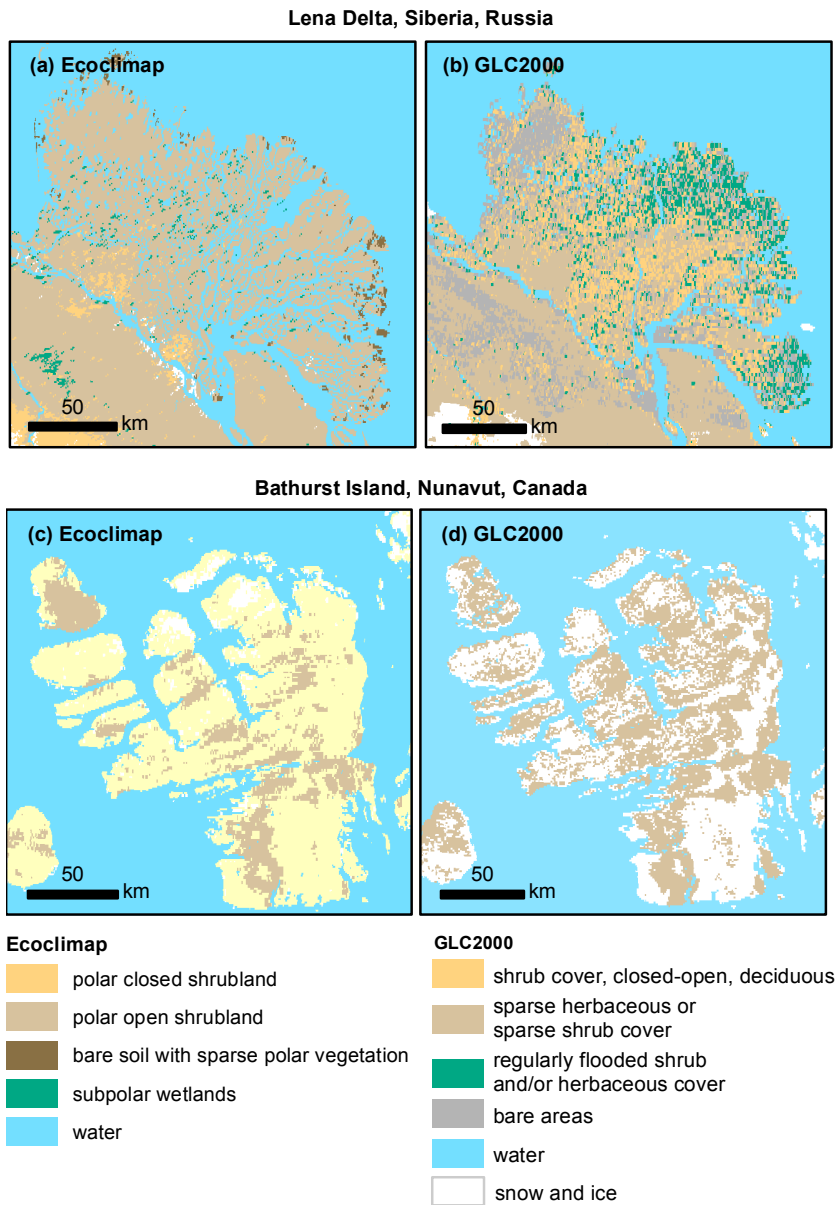
Figure 5: The global land cover classifications ECOCLIMAP and GLC2000 for (a, b) the Lena Delta in Northern Siberia (Russia) and (c, d) for Bathurst Island (Canadian High Arctic).

1.4.2 *Functional land cover heterogeneity of latent heat flux and surface temperature*

Uncertainty of MODIS LST due to subpixel land cover heterogeneity was estimated to range between 0.2 and 3.1 °C. Deviations between *in-situ* and MODIS measurements larger than 5 °C were consequently not attributed to subpixel land cover heterogeneity but interpreted as MODIS errors. Overall, *in-situ* radiometer measurements agreed well with MODIS LST. The total mean difference between *in-situ* LST and MODIS LST of 1.8 °C is within the range of deviations found at other Arctic sites (Westermann et al., 2011; Langer et al., 2010).

Spatial variations in both latent heat fluxes and surface temperature were highest during periods of high net radiation and little precipitation. Wet tundra showed highest rates of latent heat fluxes during summer followed by open water surfaces, and dry tundra. Although the soil remains saturated throughout the season in the wetland complexes, the moss surface that dominates the plant cover dries out. Consequently, the surface resistance increases which limits the latent heat flux so that more energy is available for the sensible heat flux and thus for warming the surface. This explains both the lower latent heat flux over *dry tundra* on Samoylov Island as well as the comparatively high surface temperature of *wet sedge* surfaces at Polar Bear Pass during warm and dry periods. Spatial variations in both latent heat fluxes and surface temperature diminished during overcast periods with low net radiation and frequent precipitation. LST variations at Polar Bear Pass were smaller than 2 °C for all land cover types. On Samoylov Island, differences in latent heat flux between wet tundra and open water were also negligible during the wet and cool period. Dry tundra, however, featured a latent heat flux twice as high than both wet tundra and open water. Possible causes are a higher surface roughness of dry tundra and a higher exposure to wind on the elevated rims, all of which could lead to generally increased turbulent heat fluxes at the polygonal rims with a shift towards higher latent heat fluxes.

1.5 CONCLUSIONS

An ideal land cover classification of the Arctic would be characterized by a resolution of 4 m or better to resolve the present fine-scale land cover patterns and would be updated each week to reflect land surface seasonal and inter-annual changes. Although satellite sensors are rapidly evolving, there still remains an inherent trade-off between high spatial resolutions and large coverage and/or high temporal resolution. Land surface monitoring with MODIS or similar sensors combines high temporal and spectral resolution with a global coverage but is impaired by the coarse resolution of about 1 km or more. Landsat-scale land cover classifications with resolutions of 30 m are already prone to large errors in the estimation of both the structural and the functional land cover heterogeneity in Arctic tundra landscapes. Both latent heat fluxes in polygonal tundra in Northern Siberia and land surface temperature in the Canadian High Arctic showed sustained spatial differences. The neglect of subpixel land cover heterogeneities would cause uncertainties in latent heat flux mapping of ±35 % and ±30 % in land surface temperature mapping. Subpixel- or subgrid-

scale land cover heterogeneities therefore have to be considered in the evaluation of spatially integrated flux measurements, land cover monitoring schemes and in the parameterization of the land surface in meteorological and ecosystem models. To meet these challenges, future Arctic land cover mapping will continue to rely on high-resolution remote sensing imagery. On the one hand, high-resolution land cover mapping ensures the quality of unmixing approaches. Downscaling land/water cover via Landsat surface albedo proved to be a robust approach in Arctic tundra wetlands but its applicability in other Arctic terrains requires further investigation. A refined disctinction between different vegetation types as well as types of bare areas would be desirable with regard to observed differences in the surface energy balance. While unmixing approaches deliver the areal land cover fractions, they cannot describe the probability of subpixel variation in land cover parameters, such as the distribution of patch size. Multi-scale analysis of water body abundance-size distributions in this study demonstrates the necessity of high-resolution land cover mapping for producing representative and correct land cover statistics. The classification techniques presented in this thesis can be used to compile improved fractional distributions for land cover classes within a larger-scale grid, which will facilitate upscaling of the surface energy balance as well as carbon fluxes computed for individual land cover types. This approach would account for subpixel-scale heterogeneity of land cover on a meter scale, simply by reproducing the correct land cover statistics within a grid cell.

The results of this thesis allow the following considerations for improving global land cover classifications of Arctic tundra environments. Future research efforts should focus on

- an improved parameterization of vegetation cover, especially the presence of moss,

- the further development of robust decomposition methods adapted for Arctic land surfaces to implement subpixel land cover fractions, and

- the further derivation of landscape-specific probability distribution functions for land cover parameters.

Next to an improved global Arctic land cover parameterization, multi-scale frameworks should be set up in representative regions of the Arctic that allow the monitoring of land surface processes from field measurements and high-resolution remote sensing imagery. This is of high importance considering the currently rapid rate of change of both radiative forcing and land surface processes in the Arctic.

2

SUBPIXEL HETEROGENEITY OF ICE-WEDGE POLYGONAL TUNDRA: A MULTI-SCALE ANALYSIS OF LAND COVER AND EVAPOTRANSPIRATION IN THE LENA RIVER DELTA, SIBERIA

2.1 ABSTRACT

Ignoring small-scale heterogeneities in Arctic land cover may bias estimates of water, heat and carbon fluxes in large-scale climate and ecosystem models. We investigated subpixel-scale heterogeneity in CHRIS Proba and Landsat-7 ETM+ satellite imagery over ice-wedge polygonal tundra in the Lena Delta of Siberia, and associated implications for evapotranspiration estimation. Field measurements were combined with aerial and satellite data to link fine-scale (0.3 m resolution) with coarse-scale (up to 30 m resolution) land cover data. A large portion of the total wet tundra (80 %) and water body area (30 %) appeared in form of patches less than 0.1 ha in size which could not be resolved with satellite data. Wet tundra and small water bodies represented about half of the total evapotranspiration in summer. Their contribution was reduced to 20 % in fall, during which ET rates from dry tundra were highest instead. Including subpixel-scale water bodies increased the total water surface area of the Lena Delta from 13 % to 20 %. The actual land/water proportions within each composite pixel was best captured with Landsat data using a statistical downscaling approach, which is recommended for reliable large-scale modeling of water, heat and carbon exchange from permafrost landscapes.

2.2 INTRODUCTION

Arctic terrestrial ecosystems affect the earth's climate system through the exchange of water and energy regionally, and the exchange of long-lived greenhouse gases globally (Chapin III et al., 2000). The exchange of water, energy and carbon between the surface and the atmosphere is determined by biogeophysical properties of the surface such as hydrology, albedo, and biogeochemical properties such as biomass, and vegetation type (Bonan et al., 1995; Chapin et al., 2005; McGuire et al., 2007). In both regional and global land surface and climate models, the biogeophysical parameters are estimated on the basis of land cover classifications. For large areas these land cover classifications are derived from satellite systems such as MODIS or AVHHR. Their resolutions between 250 m and 1 km do not resolve surface heterogeneities with dimensions over a few meters or even tens of meters. Fine-scale landscape heterogeneity on the scale of meters results in satellite pixels whose spectral characteristics are a composite of the different land cover types within the area covered by each pixel (Lillesand et al., 2004). This is especially true for patterned ground, which is a common phenomenon of the Arctic land surface (French, 2007; Walker et al., 2008). Ice-wedge polygonal tundra, for example, forms a network of small polygonal ponds and patches of wet or dry tundra that are 5 to 20 m

in diameter. Such features cover large areas in the Arctic coastal plains of Alaska, in the Canadian Mackenzie delta, and in the low-lying wetlands of northern Siberia (Tarnocai and Zoltai, 1988; Ping et al., 2004; Naumov, 2004). The various polygonal landscape elements have distinctly different water, heat and carbon fluxes. *Wet tundra* and *overgrown water* have been found to have the highest summer methane flux (Kutzbach et al., 2004; Sachs et al., 2010). Small water bodies show sensible and latent heat fluxes that are significantly different from the surrounding tundra in summer and winter (Langer et al., 2011b). Our understanding of the influence that these local effects have on large-scale models, however, remains limited (Chapin III et al., 2000). Whether and to which extent the aggregation of such fine-scale land cover heterogeneity introduces errors and uncertainties into extrapolation and model schemes remains a crucial matter for further research (Salmun et al., 2009). Moreover, the directions and magnitudes of these feedbacks are in a constant process of change as a result of the rapidly warming Arctic climate (Serreze et al., 2000; Hinzman et al., 2005). The resulting land surface changes in the Arctic coastal plain include an increase in above ground biomass through, for example, increased shrub cover (Sturm et al., 2001; Hinzman et al., 2005), prolongation of the snow-free season (Chapin et al., 2005) and changes in the surface water balance (Hinzman et al., 2005).

Evapotranspiration (ET), or latent heat flux, plays a key role in coupling the water and energy budget in Arctic wetlands underlain by permafrost such as the Lena Delta. Together, the precipitation (P) and the ET determine the net moisture input to a surface (P-ET), which consequently affects water fluxes and storage. Regional and local variations of P-ET affect the duration and degree of wetland saturation (Woo et al., 2008; Boike et al., 2008) with implications for the freshwater budget of the Arctic Ocean (Kattsov et al., 2007; White et al., 2007) as well as the regional and local atmospheric circulation (Rouse, 2000; Rouse et al., 2003; Serreze et al., 2003; Gutowski et al., 2007; Woo et al., 2008). Precipitation and evapotranspiration measurements are, however, sparse despite recent efforts to establish a circum-Arctic network of flux measurement stations (Euskirchen and Bret-Harte, 2009). The current distribution patterns of precipitation and evapotranspiration therefore remain largely uncertain, rendering any evaluation of recent variations and trends extremely difficult (Woo et al., 2008; Kattsov et al., 2007; Serreze et al., 2003). Flux measurements using eddy covariance techniques or standard meteorological methods deliver spatially averaged fluxes for a specific footprint area.

In this study we have investigated the effect of fine-scale variations in land cover on evapotranspiration from mid-summer to late fall in ice-wedge polygonal tundra in the Siberian Lena Delta. We used a multi-scale data set of field-based measurements together with aerial and satellite data to scale land cover and evapotranspiration from the plot (0.1 to 100 m²) to the landscape scale (100 to 10^6 m²). The objectives of the study were (i) to map the spatial variability in land cover and evapotranspiration in ice-wedge polygonal tundra, (ii) to assess the subpixel-scale spatial heterogeneity of CHRIS Proba and Landsat-7 ETM+ satellite imagery and (iii) to consider the implications of subpixel-scale variability for the landscape-scale estimation of water, energy and carbon fluxes in general, and evapotranspiration in parti-

cular. In the end, we present an empirical downscaling approach for incorporating fine-scale land cover patterns into coarse-scale climate and ecosystem models.

2.3 STUDY AREA

The study area is located on Samoylov Island in the Lena River Delta, 120 km south of the Arctic Ocean (72° 22′N, 126° 30′E) (Fig. 6a). The Lena Delta is the largest river delta in the Arctic, covering an area of about 29,036 km² (Schneider et al., 2009), of which 21,719 km² represent land and the remaining areas are occupied by rivers and coastal zones. It forms a wetland complex that is dominated by sedges, grasses, mosses, and dwarf-shrubs less than 40 cm high (Walker et al., 2005). The region is characterized by an arctic-continental climate with a mean annual air temperature of about −13 °C and a mean annual precipitation of about 140 mm. Snow melt usually starts at the beginning of June and the growing season lasts from mid-June to mid-September (Boike et al., 2008). The region is underlain by continuous permafrost that reaches depths of 500 to 600 m (Grigoriev, 1960).
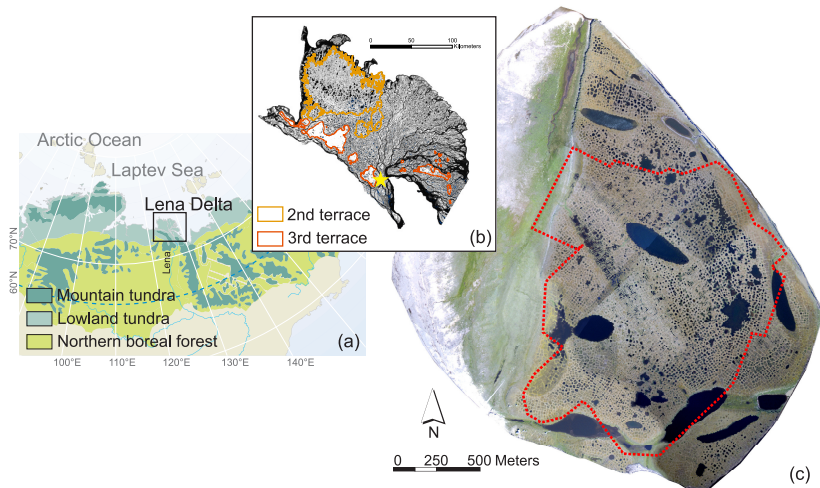
Figure 6: (a) Location of the Lena River Delta in northern Siberia. (modified from *Vegetation zones in the Arctic - UNEP/GRID-Arendal Maps and Graphics Library*) (b) Near-infrared Landsat mosaic of the Lena River Delta. The third terrace of the delta is outlined in orange and the second terrace in red, with the remaining area representing the first terrace. The yellow star indicates the location of Samoylov Island, on the first terrace. (c) Aerial image mosaic of Samoylov Island with a flood plain in the west and an elevated river terrace in the east. The red dotted line indicates the total mapped area of ice-wedge polygonal tundra.

Three main geomorphological units, *i.e.*, river terraces, were identified in the Lena Delta (Grigoriev, 1993; Schwamborn et al., 2002) (Fig. 6b). Samoylov Island is located on the first terrace (1−12 m a.s.l.), which was formed during the Middle Holocene and occupies most of the central and eastern parts of the delta with a surface area of about

$15,840\,\mathrm{km}^{-2}$ (Morgenstern et al., 2008). The first terrace is characterized by ice-wedge polygonal tundra together with large thermokarst lakes and active flood plains, and features relatively ice-rich sediments. The second terrace ($20 - 30\,\mathrm{m}$ a.s.l.) in the north-western part of the delta formed between the Late Pleistocene and Early Holocene and is characterized by sandy sediments with a low ice content. It shows little polygonal relief but features many large thermokarst lakes. The third and oldest terrace ($30 - 55\,\mathrm{m}$ a.s.l.) is an erosional remnant of a Late Pleistocene plain consisting of finegrained, organic-rich and ice-rich sediments characterized by polygonal ground and thermokarst processes.

Samoylov Island consists of an active floodplain in the west ($1.49\,\mathrm{km}^2$) that is flooded annually during spring, and an elevated river terrace ($2.85\,\mathrm{km}^2$) in the east (Fig. 6c). The terrace is characterized by large thermokarst lakes (larger than $10\,\mathrm{ha}$) surrounded by ice-wedge polygonal tundra. It has an extremely low-gradient landscape relief with slopes of less than $0.2\,\%$. The ice-wedge polygons, however, form a prominent microrelief: the growth of ice wedges in frost cracks leads to raised rims on either side of the crack that are between $0.2\,\mathrm{m}$ to $1.0\,\mathrm{m}$ higher than the low-lying polygon centers. The water table is close to the surface and drainage is greatly impeded by the underlying permafrost, resulting in water-saturated soils or inundated depressed polygon centers whereas the elevated rims and any high-centered polygons are relatively dry. High-centered polygons are typically found along lake margins and on elevated plateaus. In the following, we refer to inundated ice-wedge polygonal centers as polygonal ponds, which are shallow water bodies with depths of 0.5 to $1.0\,\mathrm{m}$.

Boike et al. (2008) and Langer et al. (2011b) conducted intensive studies into the water and energy balance on Samoylov Island. They found that about $50\,\%$ of the available net radiation is consumed by the latent heat flux, while the sensible and the ground heat fluxes make about 20 to $30\,\%$. The maximum thaw depths reach 0.4 to $0.5\,\mathrm{m}$ during summer months. Evapotranspiration is a major component of the site's water and energy budget ranging between $31\,\%$ of the total water budget in dry years and $61\,\%$ in wet years (Boike et al., 2008).
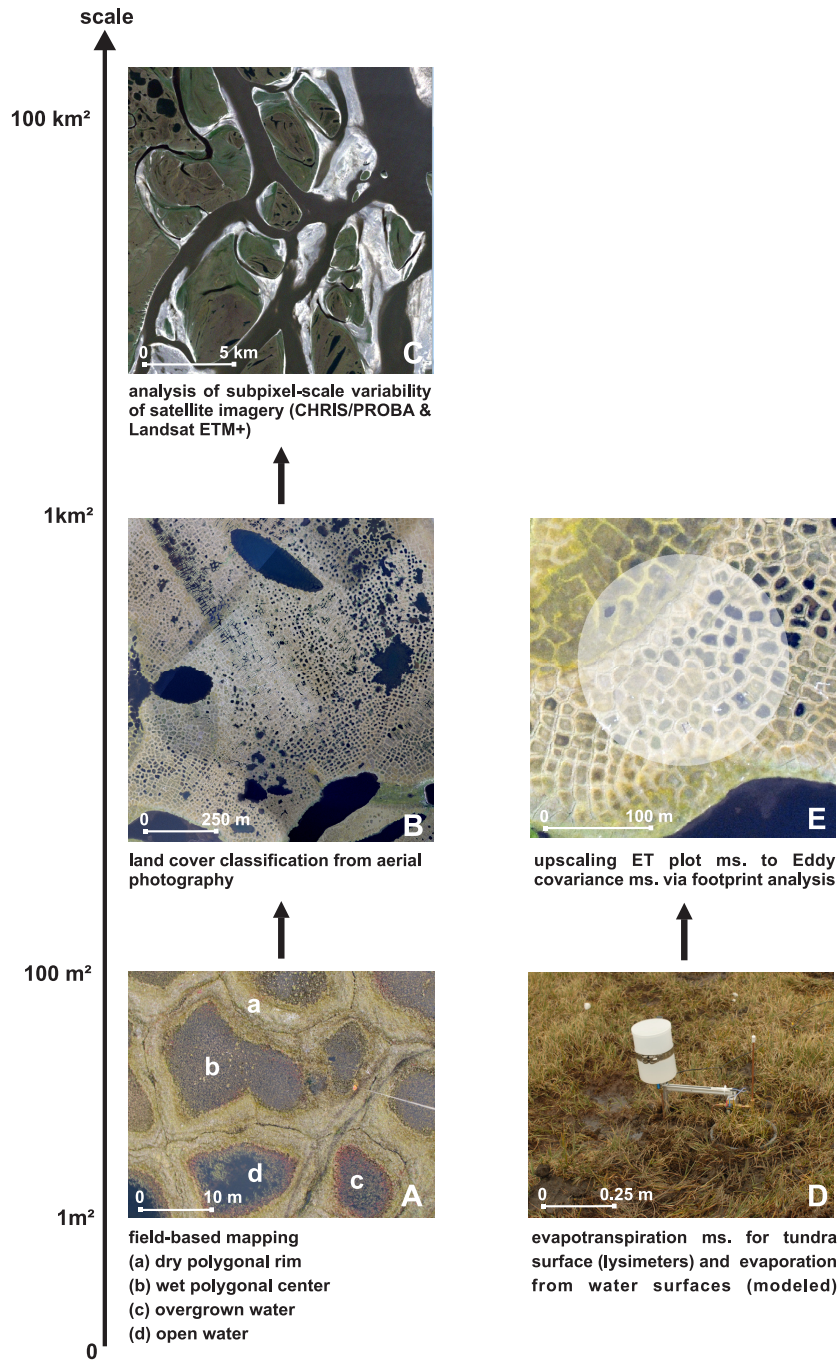
Figure 7: Scaling approach. Left hand side: Upscaling land cover from (A) field based mapping to (B) high-resolution land cover classification from aerial images, and (C) satellite imagery. Domains (A), (B) and (C) show the effect of scale on extent and resolution as investigated in the study - from the plot scale with a high resolution but limited spatial extent (A, B) to the regional scale with low resolution but a large coverage (C). Right hand side: Upscaling evapotranspiration rates from (D) plot measurements (ms.) to (E) eddy covariance measurements through aerial land cover classification of the eddy footprint.

2.4   METHODS

We used a multi-scale data set to upscale land cover and evapotranspiration (ET) from the plot scale (0.1 to 100 m²) to the landscape scale (100 to 10^6 m²). Visible and near-infrared aerial imagery was used to map the land cover in the ice-wedge polygonal tundra of Samoylov Island with a sub-meter resolution. The total mapped area encompasses about 1.76 km² of the polygonal tundra (Fig. 6). The four land cover types used were *dry tundra*, *wet tundra*, *overgrown water*, and *open water*. The aerial land cover classification was then compared with the spectral classification of CHRIS Proba and Landsat-7 ETM+ satellite images with a resolution of 17 and 30 m, respectively (Fig. 7a). The relative importance of each land cover type with regard to ET was also assessed. The plot scale ET from tundra surfaces was measured using manual and automatic lysimeters while evaporation from ponds was modeled using available climate data. Plot scale estimates of ET were then compared with eddy covariance measurements using the high-resolution land cover classification over the eddy footprint area (Fig. 7b). The lysimeter measurements, eddy covariance measurements, and the other ancillary measurements overlapped both spatially and temporally with the remote sensing data (Table 3). The spatial distribution of measuring plots and stations is shown in Figure 8.

2.4.1   *Field measurements*

2.4.1.1   *Field based land cover mapping*

Mapping of the ice-wedge polygonal tundra on Samoylov Island identified the different land cover types on the basis of an extensive field inventory of vegetation composition, vegetation structure, microtopography, and near-surface moisture.

The vegetation survey, which was completed in the summer of 2006, followed the phytosociological approach of Braun-Blanquet (Braun-Blanquet, 1932). Plant communities were recorded from 101 plots with relatively homogeneous vegetation and topography, with the plot sizes ranging from 12 to 100 m². Species presence and areal cover, *i. e.,* the relative area covered by the different plant species in a plot, were assessed visually for each plot using the standard Braun-Blanquet scale. The plots were clustered according to species cover using the *K*-means2 partitioning program by Legendre (2001) in order to obtain vegetation types.

The volumetric water content (VWC) was measured daily from August 13 to September 24, 2008, in 11 polygon centers and on their adjacent rims inserting a Campbell Hydrosense soil moisture sensor with a 12 cm fork vertically into the ground. Square plots (50x50 cm) of relatively homogeneous vegetation were identified at each site for the measurements and the average of three measurements was recorded for each of the plots.

The microtopography of each measurement site was classified as elevated or collapsed polygon rim, elevated or depressed polygon centers, and trench or crack.

Table 3: Observation periods and number of plots for field measurements of volumetric water content (VWC), evapotranspiration (ET), and vegetation surveys in *wet tundra* and *dry tundra*. Details of aerial and satellite data, including image acquisition dates.

FIELD & REMOTE MEASUREMENTS	DATE/TIME PERIOD	NUMBER OF PLOTS
VWC	August 13 to September 24, 2008	*dry tundra*: 11, *wet tundra*: 11
ET	July 21 to September 14, 2008	*dry tundra*: 7, *wet tundra*: 10
vegetation survey	July, 2006	*dry tundra*: 51, *wet tundra*: 50
aerial imagery	August 1, August 9 and August 15, 2008	
CHRIS Proba	July 23, 2008	
Landsat-7 ETM+, North and South of Delta, including area of study site	July 27, 2000	
Landsat-7 ETM+, West of Delta	July 26, 2001	

2.4.1.2 *ET measurements from lysimeters*

ET from tundra surfaces was measured at the plot scale from July 21 to September 14, 2008, using both manual and automatic weighing lysimeters. Seventeen lysimeters were installed along a 1 km transect (Fig. 8), seven in wet polygon centers and ten on dry polygon rims.

Automatic lysimeters consisted of two cylindrical containers nested inside each other. The inner container had an internal diameter of 0.21 m and a height of 0.10 m. A load cell (Soemer 1006) was installed centrally at the base, between the inner and outer cylinders. This load cell had a measurement range of 2 to 5 kg with an accuracy of 0.03 %: a 3-point calibration was conducted in the field. A sample of the upper layer of soil and vegetation was excavated and carved by hand to fit into the inner cylinder, providing a relatively undisturbed sample. Automatic lysimeter weights were recorded every half hour using a CR1000 Campbell Scientific Logger. Mean daily values for the automatic lysimeters were calculated from noon to noon.

Manual lysimeters also consisted of two nested cylindrical containers, with internal dimensions of 0.14 m diameter and 0.12 m height. Weights from the manual lysimeters were recorded daily at noon using a Kern MH5K5 pocket balance, which had an accuracy of ± 5 g.

Measurements from manual lysimeters were rejected on days that had measurable precipitation, and those from automatic lysimeters were rejected for any periods of precipitation. The observed drying and wetting of the samples was in general agreement with surrounding surface conditions throughout the observation period. Mean daily ET rates for both dry rims and their associated wet centers were derived by averaging both manual and automatic lysimeters measurements provided that at least 3 observations were available from the

dry and wet sites, respectively. A total of 40 daily ET observations were thus obtained from *dry tundra* and 44 from *wet tundra* during the 56-day observation period.

2.4.1.3 *Evaporation from water surfaces*

We used a flux gradient approach to estimate evaporation (E) from small water bodies (smaller than 0.1 ha. The latent heat flux, Q_E, can be related to the difference between the specific humidity at the measurement height, $q(z_m)$, and at the water surface, $q(z_{surf})$, as follows:

$$Q_E = \frac{-\rho_{air}L_v}{r_a}(q(z_m) - q(z_{surf})),$$ (4)

where ρ_{air} is the density of air, L_v is the latent heat of vaporization and r_a is the aerodynamic resistance (Garratt, 1994).

The specific humidity at a saturated surface, $q(z_{surf})$, can be inferred from the surface temperature, T_{surf}, using the Magnus formula, which gives the water vapor pressure over a water surface (Sonntag, 1990). The specific humidity of air, $q(z_m)$, at the measuring height, ($z_m = 2\,m$), is calculated from the air temperature, T_{air}, applying the Magnus formula in combination with the relative humidity, RH, at the measuring height.

The aerodynamic resistance, r_a, can be expressed as

$$r_a = \frac{\left[\ln\left(\frac{z_m}{z_o}\right)\right]^2}{\kappa^2 u_{zm}},$$ (5)

where u_{zm} is the horizontal wind speed at measuring height z_m, $\kappa = 0.4$ is the von Kármán constant, and $z_o = 10^{-4}\,m$ is the roughness length for a calm water surface (Garratt, 1994). Equation (2) is only valid for neutral conditions, which dominated the atmospheric stratification at the study site in 2008 (Langer et al., 2011b), and provides a first-order approximation for the turbulence characteristics at this site.

E (mm) is related to Q_E through the latent heat of vaporization, L_v, as follows:

$$Q_E = \rho_{air}L_v E.$$ (6)

The water surface temperature was measured about 1 cm below the water surface of a shallow polygonal pond (total depth of about 0.8 m) using a PT100 temperature sensor, protected from radiation. We considered these water temperatures to be representative of all small water bodies with a surface area of less than 0.1 ha. Air temperature was measured in 2 m height at the eddy covariance measurement site, again using a PT100 sensor. Both PT100 sensors had an accuracy of 0.1 to 0.2 °C. Relative humidity was measured at the eddy covariance measurement site with an MP-100 humidity-temperature meteorological probe with an accuracy of ±1 % (Rotronic, Switzerland). Daily mean values were used for all parameters in order to calculate evaporation. The evaporation model was applied to both surfaces of *open water* and *overgrown water* (with up to 15 % areal plant cover).

2.4.1.4 *ET measurements from eddy covariance*

The ET at the landscape scale was determined using the eddy covariance method in summer 2008 as described by Langer et al. (2011b). The eddy covariance system consisted of a Campbell C-SAT 3D sonic anemometer and an open path LI-COR LI-7500 CO_2 and H_2O gas analyzer mounted on a 2.4 m mast. Data was processed according to a standard quality assessment (Mauder and Foken, 2004; Mauder et al., 2008) resulting in an estimated measurement accuracy for ET of about 15 % (Mauder et al., 2006). The quality assessment resulted in a data reduction of about 4 %. A further data reduction of about 14 % occurred as a result of exclusion of the area on the leeward side of the mast ($263 - 277°$). No gap filling was applied. Missing values were randomly distributed throughout the eddy data set and we therefore considered the average latent heat flux value to be representative for the observation period. Further details on measurement equipment setup and data processing can be found in Langer et al. (2011b).

The source area for the latent heat flux was determined for each half-hour value using the footprint model of Schmid (1994). A constant aerodynamic roughness length of $z_0 = 10^{-3}$ m was assumed for the area of the footprint that included both tundra and water surfaces. The average footprint for the observation period broadly resembled a circle with a diameter of 100 m as shown in Figure 7. During the observation period from July to September 2008, wind directions showed only a slight predominance in the NW and ESE directions, and ratios of land cover types within the footprints showed only minor variations (± 5 %) (Langer et al., 2011b).

Ancillary measurements were collected at a standard climate tower in the vicinity of the eddy covariance system, including net radiation (using a CNR1 Net Radiometer from Kipp & Zonen, Netherlands) with an accuracy of 10 %, and precipitation (using a tipping bucket rain gauge - Model 52203 from R.M. Young Company, USA) with an accuracy of 2 % (Boike et al., 2008).

2.4.1.5 *Upscaling ET measurements*

A 'measure and multiply' approach was used to extrapolate plot measurements of ET per unit area for each land cover type to the eddy footprint area and to the total mapped area of ice-wedge polygonal tundra (Fig. 8 on Samoylov Island. The total ET over *i* land cover types was calculated using

$$ ET = \sum \left(\% A_i \times ET_i \right) , \tag{7} $$

where ET is the total evapotranspiration, A_i is the total area of land cover type *i*, and ET_i is the evapotranspiration per unit area from the land cover type *i*. Areally weighted plot-scale measurements of ET for the eddy footprint were then compared to the measured eddy covariance data.

2.4.2   *Remote sensing data*

2.4.2.1   *Aerial imagery*

We obtained sub-meter resolution aerial images of Samoylov Island by mounting two Nikon D200 cameras on a helium-filled dirigible. Images were acquired in the visible (VIS) and near-infrared (NIR) ranges (together referred to as the VNIR range). The internal IR-filters were removed from the cameras in a laboratory (LPD LLC, USA), allowing them to capture a maximum range from about 330 to 1200 nm. A Schneider Kreuznach B+W 486 UV-IR cut filter was used for one of the cameras to obtain images in the VIS range, from about 400 to 690 nm, while the second camera was fitted with a Schneider Kreuznach B+W IR-filter 093 to acquire images in the NIR range, above about 830 nm.

The flights took place at noon on sunny, cloudless days (August 1, August 9 and August 15, 2008). The total precipitation during the flying period (from July 31 to August 15) was 6.5 mm with a daily maximum of 1.6 m on August 10. An average flying altitude of 750 m resulted in a pixel size of about 0.18 m.

The aerial image data were processed using ENVI 4.7 image processing software. NIR images were registered onto VIS images using the automatic image-to-image registration with an average root mean square error (RMSE) of 0.53 pixels. The resulting VNIR images were then georeferenced using an orthomosaic of the island from 2007 with a resolution of 0.3 m. We chose the nearest neighbor algorithm for all resampling operations.

Sixteen images were used to map the ice-wedge polygonal tundra on Samoylov Island, with an image overlap of about 25 %. Land cover classification was carried out individually for each VNIR image. *Open water* surfaces were extracted using a density slice classification applied to the NIR band. The NIR range is especially suited for detecting water bodies as most of the incoming energy is absorbed and thus a marked difference exists between the reflectance from *open water* surfaces and that from vegetated surfaces. We chose a threshold that most effectively separated the image pixel values for water from those for vegetated surfaces. *Open water* surfaces were subsequently masked and the remaining three vegetated land cover types, *i.e.*, *wet tundra*, *dry tundra* and *overgrown water*, were classified using a supervised maximum likelihood classifier. Training areas and areas for accuracy assessment were selected from field based mapping completed in 2006, 2008 and 2010. Spurious pixels within a class were changed to conform to that class by applying a majority filter of 11x11 pixels. The relative classification accuracy was calculated by comparing the classifications for overlapping areas of adjacent images. In order to determine the overall classification accuracy we compared a total of 147 ground-based plots to the final aerial land cover classification. Areas smaller than 0.5 x 0.5 m were not included in subsequent analyses.

2.4.2.2   *Satellite imagery*

We used CHRIS Proba imagery with a resolution of 17 m per pixel, and Landsat-7 ETM+ imagery with a resolution of 30 m, to investigate the effect of coarse resolutions on land cover mapping in ice-wedge polygonal tundra.

The CHRIS Proba image was acquired on July 23, 2008. The image was taken in CHRIS Proba operation mode 3 with 18 spectral bands covering the VNIR range from 400 to 1050 nm. The image was corrected for noise and atmospheric effects using the noise reduction (Gómez-Chova et al., 2008) and the atmospheric correction tool (Guanter et al., 2006) available in the BEAM VISAT 4.6.1 software.

An atmospherically corrected Landsat mosaic processed by Schneider et al. (2009) was used to classify the entire Lena Delta. Schneider et al. (2009) identified nine land cover classes for the Lena Delta, five of which are present in the ice-wedge polygonal tundra on Samoylov Island. We therefore performed classification for these five classes only, which together make up 70 % of the total land area in the Lena Delta. The Landsat mosaic consists of three images aqcuired on July 27, 2000 (featuring Samoylov Island) and July 26, 2001. Bands 1 to 5 and band 7 were used for classification covering a spectral range in the VNIR and short-wave infrared (SWIR) from 450 to 2350 nm.

Both the CHRIS Proba image and the Landsat mosaic were classified using a *k*-means unsupervised algorithm in the ENVI 4.7 software. Unsupervised classifications are based solely on the natural groupings within the image, *i. e.*, the spectral properties of the surface, and as such return spectral classes containing spectrally similar pixels (Lillesand et al., 2004). The *k*-means algorithm is an iterative clustering algorithm that maximizes the between-cluster variance and minimizes the within-cluster variability (MacKay, 2003). The within cluster variability is expressed as the sums of squared distances, *SS*, between each pixel *x* and its assigned cluster center *C(x)* (MacKay, 2003):

$$SS = \sum_{\forall x} [x - C(x)]^2 . \tag{8}$$

Classification was performed with 9 clusters and 15 iterations. For Samoylov Island, we compared the satellite spectral classifications (*k*-means) from CHRIS Proba data and Landsat data with the aerial land cover classification, in order to assess the fine-scale land cover variability within each satellite pixel and *k*-means class. *k*-means classifications of the satellite data were registered onto the aerial land cover classification in ArcGIS 10, with an RMSE of less than 1 pixel.

2.5 RESULTS

2.5.1 *Land cover classification from field mapping*

The ice-wedge polygonal tundra on Samoylov Island exhibits four distinct land cover types comprising two types of tundra and two types of water bodies. The tundra shows distinct characteristics related to microtopography and through variations in vegetation and surface wetness, which resulted in a classification into *dry tundra* or *wet tundra*. The *dry tundra* had a mean volumetric water content (VWC) of about 25 % in the upper 10 cm of the soil, whereas the *wet tundra* had a mean VWC of about 93 % throughout the observation period from August 13 to September 24, 2008. Both *dry tundra* and *wet tundra* did not show significant differences in VWC for the summer and fall period. *Dry tundra* was found on polygon ridges, well drained plateaus and elevated

polygon centers, while *wet tundra* land cover was found in depressed polygon centers, in trenches and on collapsed ridges. Both *wet tundra* and *dry tundra* were dominated by mosses, which comprised up to 98 % of the cover. They differed, however, with regard to key species and plant functional types (Table 4).

Water surfaces were classified as either *overgrown water*(with up to 15 % areal plant cover), or *open water* with no emersed vegetation. *Overgrown water* was found in frost cracks and in polygon centers with transient water accumulations, as well as close to the banks of ponds and lakes.

Table 4: Volumetric water content (VWC) of the upper surface (10 cm), plant functional types, and key species for wet and *dry tundra*, derived from field measurements. The VWC is shown as the range of surface moisture (in percentages) across all plots, for *dry tundra* and *wet tundra*.

	DRY TUNDRA	WET TUNDRA
VWC [range in %]	7 - 51	55 - 100
key species	*Hylocomium splendens, Dryas punctata*	*Drepanocladus revolvens, Meesia triquetra, Rhizomnium punctatum*
plant functional type [cover in %]		
moss	96	98
forb	8	2
shrub	3	1
grass	2	1
sedge	5	16
lichen	2	smaller than 1

2.5.2 *Land cover classification from aerial photography*

High-resolution aerial photography during the observation period between July and September, 2008, revealed the total mapped area of Samoylov Island to be composed of 58 % *dry tundra*, 17 % *wet tundra*, and 25 % water surfaces, thereof 10 % *overgrown water* and 15 % *open water* (Fig. 8a). Excluding large thermokarst lakes (larger than 0.1 ha), the ice-wedge polygonal tundra was composed of 65 % *dry tundra*, 19 % *wet tundra*, and 16 % water bodies (Table 5). The average footprint area of the eddy covariance station had a much higher proportion of *wet tundra* with 37 %, and a lower proportion of water bodies with 10 %.

Both field observations and the aerial classification showed that the extent of surface water varied by about ±5 % over the observation period (July 21 to September 14, 2008), which is a negligible figure compared to the overall classification accuracy. In areas where aerial photographs overlap, the land cover classification varied by about 3 % on average. The overall accuracy of the classification was 84 %, with the *open water* class showing the highest level of accuracy with 100 %, followed by the *wet tundra* with 91 %. The *overgrown water* and *dry tundra*

classes showed the lowest accuracy (62 % and 75 %, respectively) with most of the misclassified sites categorized as *wet tundra*.
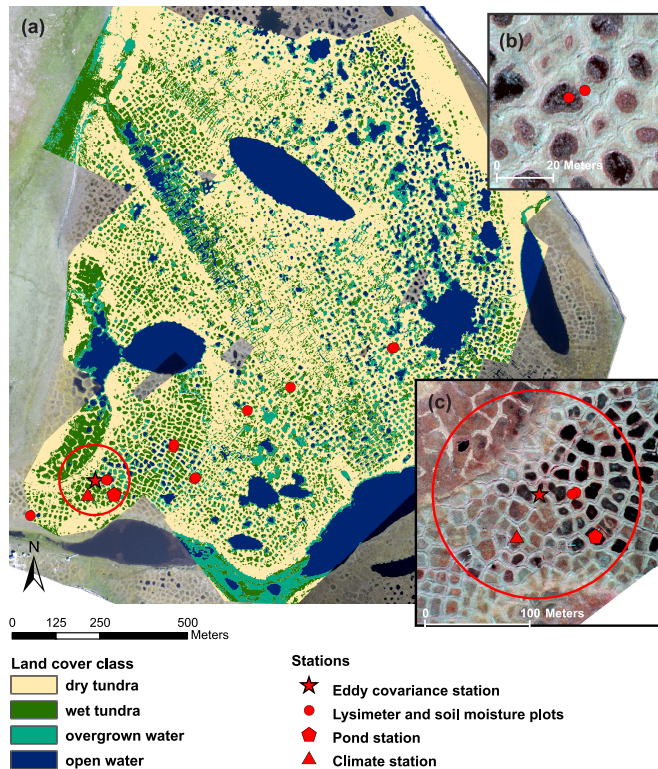
Figure 8: (a) Aerial land cover classification of the ice-wedge polygonal tundra on Samoylov Island, showing the polygonal pattern of low-lying centers of *wet tundra* and polygonal ponds, separated by elevated polygonal rims of *dry tundra*. Locations of measurement stations are marked in red. The red circle indicates the approximate footprint area of the eddy covariance station. (b) Close-up view of a near-infrared aerial image showing a typical lysimeter and soil moisture measurement, set-up with one lysimeter installed in a wet polygon center and another on on a dry polygon rim. (c) Close-up view of the eddy footprint area and the measurement stations within.

In the discussions below we use the term water bodies to refer to both *overgrown* and *open water* with surface areas greater than 5 m². Water bodies ranged from ice-wedge polygonal ponds (smaller than 0.1 ha) to large thermokarst lakes (larger than 10 ha) with a mean surface area of 108 m². Polygonal ponds with a surface area between 0.003 and 0.1 ha are abundant in the ice-wedge polygonal tundra on Samoylov Island, amounting to 748 water bodies per square kilometer. More than 90 % of the total number of water bodies had a surface area less than 500 m². About 50 % of the total number of water bodies had a surface area less than 10 m², but despite their large number they contributed only about 1 % to the total water surface area. Large thermokarst lakes were not common and represent less than 1 % of the total number of water bodies, while contributing over 45 % to the total water surface area (Fig. 9).

Table 5: Land cover percentages and ET ratio for the eddy footprint, the total mapped area on Samoylov Island, and the Lena Delta. Land cover percentages of the Lena Delta represent the subpixel-scale heterogeneity as derived from Figure 12. Land surface percentages exclude water bodies with surface areas greater than 0.1 ha, *i.e.*, water bodies that can be mapped directly with Landsat data. ET ratio is the contribution of the different land cover types to the areally weighted evapotranspiration based on the mean daily ET rates for the whole observation period as well as for the summer and fall period (Fig. 11).

STUDY AREA, PERIOD	LAND COVER RATIO [%]			ET RATIO [%]		
	dry tundra	*wet tundra*	*open water*	ET_{dry}	ET_{wet}	E_{water}
Eddy footprint, summer & fall	54	37	9	52	40	8
SAM, summer & fall	65	19	16	65	21	14
SAM, summer				53	29	18
SAM, fall				79	13	9
Lena Delta	72	16	12			

The frequency distribution of *wet tundra* patches was similar to the frequency distribution of water bodies but the mean surface area of *wet tundra* patches was much smaller with 22.5 m². About 99 % of the *wet tundra* patches were smaller than 500 m², making up 80 % of the total surface area of *wet tundra*.

No mean patch size could be given for *dry tundra*. The aerial land cover classification did not resolve cracks and troughs in full detail, so that *dry tundra* appears as an interconnected surfaces of dry rims and high-centered polgyons on the map which together make up 94 % of the total area of *dry tundra*.
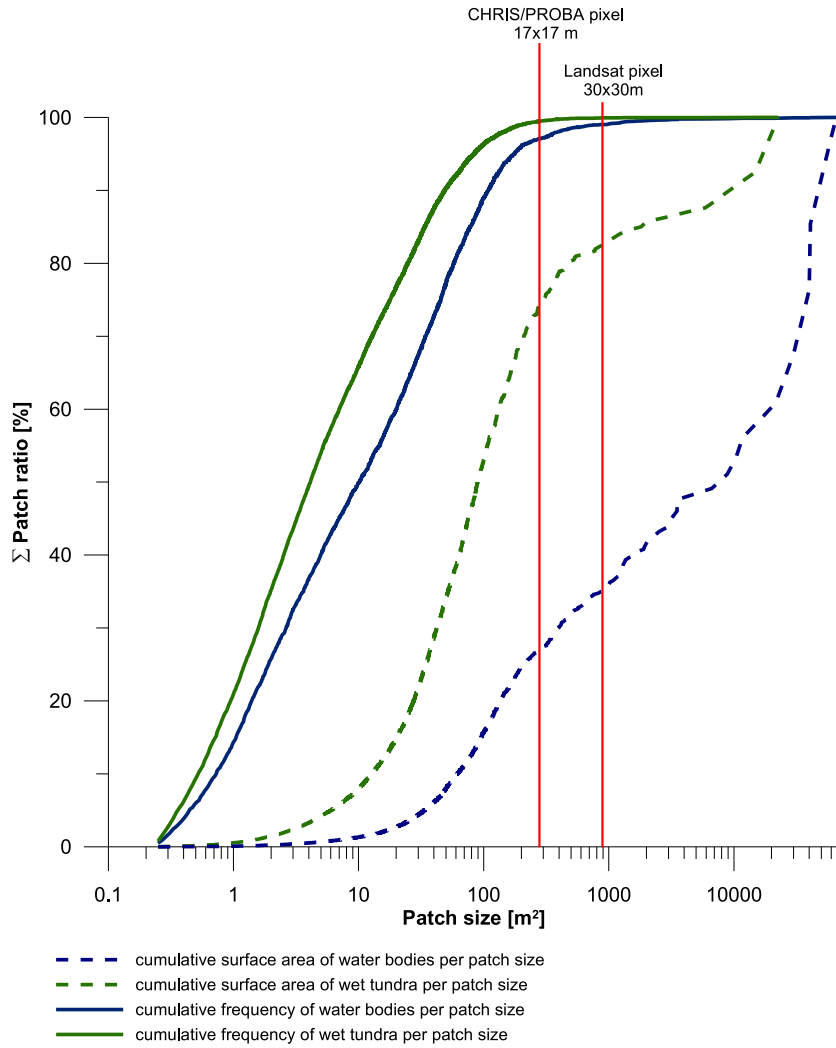
Figure 9: Cumulative percentage plots of surface areas (broken lines) and frequencies (continuous lines) for water bodies and *wet tundra* patches. Vertical lines indicate the pixel size of CHRIS Proba data (17 × 17 m) and Landsat data (30 × 30 m).

2.5.3   *Spatial and seasonal characteristics of evapotranspiration*

The observation period was characterized by two main synoptic periods: a relatively dry summer period (21 July to 21 August) with low precipitation and high net radiation, followed by a period of frequent heavy rain events and low net radiation during the fall (22 August to 14 September) (Fig. 10). The precipitation input (67 mm) and net evaporative output (68 mm) during the observation period were in overall balance. Negative latent heat fluxes were measured on 20 nights during the 56-day observation period with a mean of $-21.4\,\mathrm{Wm^{-2}}$.
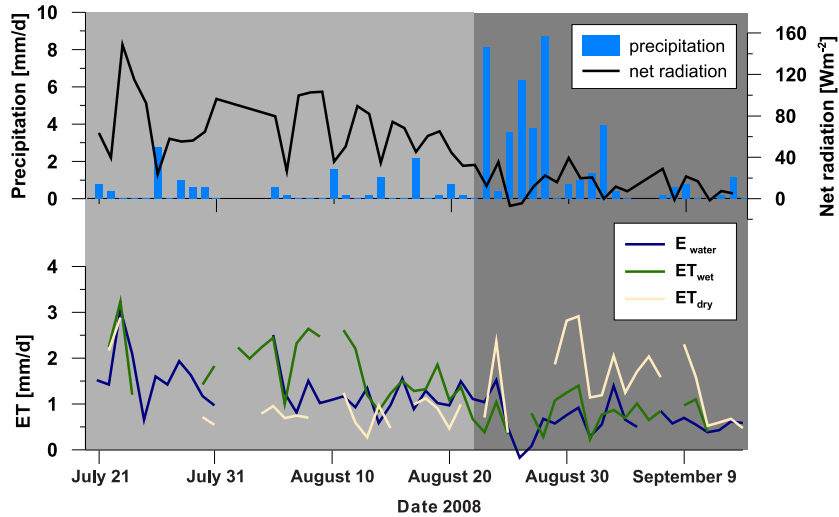
Figure 10: Daily precipitation, net radiation and evapotranspiration (ET) from wet (ET_{wet}) and *dry tundra* (ET_{dry}) and evaporation from water bodies (E_{water}) during the observation period from July 21 to September 14, 2008. Summer and fall are represented by light grey and dark grey backgrounds, respectively.

Evapotranspiration from *wet tundra* (ET_{wet}) and water bodies (E_{water}) was highest during the summer period (Fig. 11). E_{water} and ET_{wet} were higher than ET from *dry tundra* (ET_{dry}) by 40 and 80 %, respectively. In summer, ET_{wet} was about 20 % higher than E_{water}. Both E_{water} and ET_{wet} decreased from summer to fall by 52 and 57 %, respectively, whereas ET_{dry} increased by 47 %. ET_{dry} was twice as high than ET_{water} and ET_{wet} in fall. Over the whole observation period the effect of the different synoptic periods was canceled out and ET rates from *dry tundra* ($1.2\,\mathrm{mmd^{-1}}$) with a standard deviation (SD) of $0.8\,\mathrm{mmd^{-1}}$) were almost the same as ET rates from *wet tundra* ($1.3\,\mathrm{mmd^{-1}}$; SD = $0.9\,\mathrm{mmd^{1}}$) and water bodies ($1.0\,\mathrm{mmd^{-1}}$; SD = $0.6\,\mathrm{mmd^{-1}}$).

ET rates of *wet tundra* and *dry tundra*, together with those for water bodies, were used to derive the area-weighted average ET rate of $1.2\,\mathrm{mmd^{-1}}$ (SD = $0.7\,\mathrm{mmd^{-1}}$) for the eddy footprint. Direct measurements of ET using the eddy covariance system during the observation period showed an average rate of $1.2\,\mathrm{mmd^{-1}}$ (SD = $0.6\,\mathrm{mmd^{-1}}$). The average area-weighted ET rate for the whole area of ice-wedge polygonal tundra on Samoylov Island (excluding large thermokarst lakes) was $1.2\,\mathrm{mmd^{-1}}$ (SD = $0.6\,\mathrm{mmd^{-1}}$) (Table 5). The contribution from *wet tundra*, *dry tundra* and water bodies to total landscape-scale ET

varied considerably for summer and fall. In summer, *wet tundra* and water surfaces together contributed about half to total ET of the ice-wedge polygonal tundra on Samoylov Island (excluding lakes larger than 0.1 ha), whereas their contribution was reduced to about 20 % in fall.

Summer period (July 21 to August 21)			Fall period (August 22 to September 14)		
wet tundra	dry tundra	water	wet tundra	dry tundra	water

	Summer period			Fall period		
	wet tundra	dry tundra	water	wet tundra	dry tundra	water
average ET rate	1.8	1.0	1.4	0.8	1.4	0.7
standard deviation	1.0	0.7	0.7	0.4	0.9	0.4
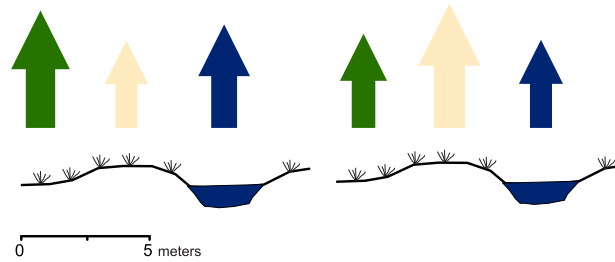
Figure 11: ET rates for *wet tundra*, *dry tundra*, and water surfaces during summer and fall, as derived from plot measurements. The size of the arrows is proportional to the ET rates.

2.5.4 *Downscaling mixed satellite pixels*

Satellite pixels could be decomposed into their respective subpixel components by intersecting the aerial land cover and the satellite imagery classifications. A pixel-by-pixel analysis yielded the proportion of each aerial land cover classes within each satellite pixel (Fig.12). Only 9 % of all Landsat pixels mapped on Samoylov Island can be considered as homogeneous, containing 95 % or more of one land cover type. The remaining 91 % of the pixels were composed of patches or fragments of *dry tundra* and *wet tundra* as well as water surfaces.

Figure 12a and b show the ratio of each aerial land cover class in each of the nine *k*-means classes of the CHRIS Proba and the Landsat images. For both CHRIS Proba and Landsat, the spectral classification of the satellite pixels was determined by the proportions of *open water* and *dry tundra* within each pixel. Class 1 was a water class with a mean ratio of 93 % *open water* for CHRIS Proba and 86 % for Landsat. Classes 2 to 9 were then characterized by a gradual decrease in *open water* and an increase in *dry tundra*. Class 1 and Class 4 to 10 in particular showed clear differences in the ratio of *open water* and *dry tundra*. The proportions of the different land cover types within each satellite pixel in Class 2 and Class 3, however, showed considerable variation.

Only 8 % of the total mapped area on Samoylov Island could be classified as water bodies (including large thermokarst lakes) from CHRIS Proba and Landsat data (Fig.12c and d) compared to 25 % from high-resolution aerial images. Over 90 % of the number of both water bodies and *wet tundra* patches in the ice-wedge polygonal tundra of Samoylov Island were smaller than either the CHRIS Proba or the Landsat pixels (Fig. 9). Thus 27 % of the total surface area of water bodies was not resolved by CHRIS Proba and 35 % was not resolved by Landsat

imagery. Similarly, 75 % of the total surface area of *wet tundra* could not be resolved from CHRIS Proba data and 83 % from Landsat data.

The relative proportions of the different land cover types within the satellite pixels were very similar for CHRIS Proba and Landsat in the *k*-means Class 1 to Class 7 (Fig.12a and b). The main difference between the two types of imagery could be seen in Class 8 and Class 9. Class 8 showed an increasing proportion of *overgrown water* in the Landsat imagery but this was at a minimum in the CHRIS Proba imagery. Landsat Class 8, however, made up only 1 % of the total mapped area and subpixel composition may therefore not have been representative (Fig. 12d). In Landsat Class 9, the proportion of *dry tundra* increased while the proportions of *wet tundra* and water surfaces were negligible. In contrast, CHRIS Proba Class 9 showed a decreasing proportion of *dry tundra* and increasing proportions of *wet tundra* and water surfaces.
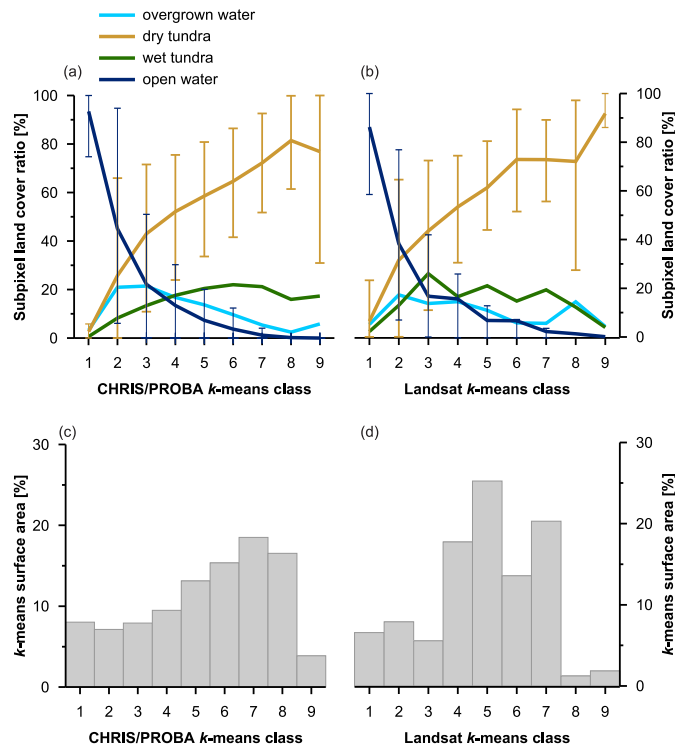
Figure 12: Mean subpixel-scale land cover percentages shown for each *k*-means class from (a) CHRIS Proba data collected on July 23, 2008 and (b) Landsat-7 ETM+ collected on July 23, 2000 of the total mapped area on Samoylov Island. Vertical lines indicate the lower 10 %- and the upper 90 %-quantile for the relative proportions of subpixel-scale *open water* and *dry tundra*. *Open water* and *overgrown water* (quantiles not shown) show a good separability from *dry tundra* in both CHRIS Proba and Landsat data. Subpixel-scale ratios of *wet tundra* (quantiles not shown) can be clearly separated from the other land cover classes in Landsat but not in CHRIS Proba data. (c) and (d): Grey bars show the percentage of the total mapped area covered by each of the *k*-means classes for (c) CHRIS Proba and (d) Landsat.

2.5.5 *Landsat subpixel heterogeneity of the Lena River Delta*

The Landsat subpixel heterogeneity as shown in Figure 12b was used to assess the proportions of land and water within each Landsat pixel across the entire Lena Delta (Fig. 13). Large thermokarst lakes and Lena River channels were represented in *k*-means Class 1. With 60 % water and 40 % land, *k*-means Class 2 could not clearly be categorized as either a water or land class; it covered mainly riparian and coastal areas. Class 3 to Class 9, on the other hand, had proportions of about 1/3 or less water surfaces and were therfore considered to be land classes. These classes covered a total area of 12781 km², which made up about 70 % of the total land area in the delta. Water surfaces within Class 3 to Class 9 (as derived from Figure 12b) amounted to an area of 1577 km², representing about 7 % of the total land area in the delta. The area covered by water surfaces was divided into 971 km² *overgrown water* and 606 km² *open water*. The overall proportions of *dry tundra*, *wet tundra*, and water surfaces within Landsat pixels for the entire Lena Delta were similar to those for ice-wedge polygonal tundra on Samoylov Island (Table 5).

The distribution of the *k*-means classes within the Lena Delta reflected the main geomorphological terraces (Fig. 13). Class 9 dominated the second terrace in the north-western part of the delta, whereas the third terrace was characterized by Class 9 together with Class 8, both of which have little or no subpixel-scale heterogeneity. The first terrace, in the central and eastern part of the delta, was dominated by Class 3 to Class 7, which had high proportions of water surfaces and *wet tundra* and were therefore likely to indicate the presence of polygonal tundra. These classes occupied an area of 6192 km², representing about 30 % of the total land area of the delta.

We tested the downscaling approach in an area in the south-western part of the Lena Delta, in which Grosse et al. (2008) mapped about 239 ha of small open water bodies (0.003 to 0.1 ha) from panchromatic SPOT-5 data with a 2.5 m resolution. Decomposing composite Landsat pixels via the downscaling function in this study yielded 88 ha of *open water* and 305 ha of combined *open water* and *overgrown water*.
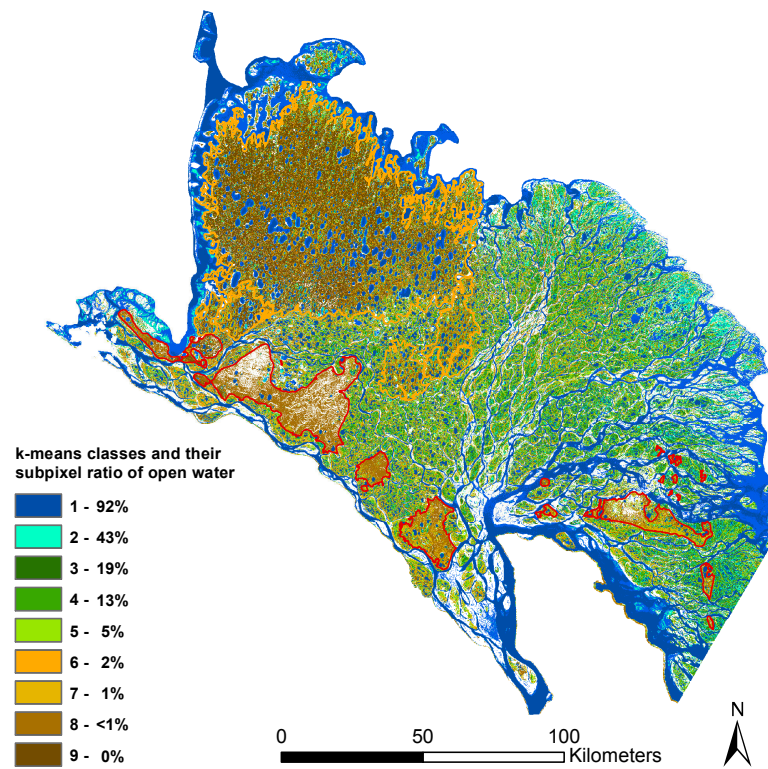
Figure 13: Percentage of subpixel-scale *open water* for each of the nine *k*-means classes in the Lena Delta. The spectral grouping of the *k*-means classes is determined by the the relative proportions of subpixel-scale *open water* versus *dry tundra* as shown in Figure 12. White areas were not included in the classification as they are not spectrally representative of the ice-wedge polygonal tundra on Samoylov Island. Orange boundaries indicate the second terrace, red boundaries the third terrace of the Delta. The remaining area belongs to the first terrace.

2.6 DISCUSSION

2.6.1 *Plot-scale evapotranspiration characteristics*

Plot measurements of ET were successfully scaled to eddy covariance measurements. The total ET of $1.2 \, \text{mm} \, \text{d}^{-1}$ for ice-wegde polygonal tundra on Samoylov Island using lysimeter measurements and evaporation modeling is well within the range of previously reported values for polygonal tundra, which lie between 1.0 and $1.8 \, \text{mm} \, \text{d}^{-1}$ (Eugster et al., 2000). Summer ET rates (July to August) of *wet tundra* and *dry tundra* found in this study are in good agreement with values presented by Langer et al. (2011b), who found ET rates of $1.0 \, \text{mm} \, \text{d}^{-1}$ (SD=$1.1 \, \text{mm} \, \text{d}^{-1}$) for *dry tundra* and $2.2 \, \text{mm} \, \text{d}^{-1}$ (SD=$1.1 \, \text{mm} \, \text{d}^{-1}$) for *wet tundra* for a period from June to August. The summer evaporation rate from water surfaces of $1.4 \, \text{mm} \, \text{d}^{-1}$ in this study falls at the lower range of values reported in other studies on the Alaskan coastal plain (2.0 to $2.3 \, \text{mm} \, \text{d}^{-1}$) (Kane and Carlson, 1973; Rovansek et al., 1996; Mendez et al., 1998) and in Canada ($4.4 \, \text{mm} \, \text{d}^{-1}$) (Roulet and Woo, 1986), which is most likely explained by higher values of net radiation at these more southerly study sites.

In summer, *wet tundra* and water bodies on Samoylov Island show higher ET rates than *dry tundra*. The differences in summer ET rates seem to be primarily controlled by the combination of high net radiation and low precipitation which has also been pointed out by other studies on Samoylov Island (Boike et al., 2008; Langer et al., 2011b) and at other locations on the Arctic coastal plain (Liljedahl et al., 2011). The tundra at the study site is dominated by mosses, which can strongly control the water vapor flux at the surface (Rouse, 2000; McFadden et al., 2003; Grant et al., 2003). Mosses lack stomatal control of water loss (Oechel and Sveinbjörnsson, 1978). They therefore evaporate freely provided they are moist (Rouse, 2000; Thompson et al., 2004). Rates of water loss from a saturated moss canopy can be comparable or even higher than those from a free water surface (Firbas, 1931; Barkman, 1958), which explains the magnitude of evaporation from water surfaces being similar to that from *wet tundra* in summer and fall. *Wet tundra* in the low-lying ice-wedge polygonal centers stays saturated throughout summer and fall due to the near-surface water level, while *dry tundra* on the elevated polygonal rims relies mostly on precipitation for moisture input. This likely explains the difference in ET rates during the summer, when the combination of high net radiation and little precipitation limits ET from *dry tundra*.

In fall, the difference between ET from *dry tundra* and *wet tundra* as well as water bodies is reversed with ET from *dry tundra* being about $40 \, \%$ higher than from both *wet tundra* and water bodies. This result suggests other limitations than net radiation and near-surface soil moisture on local ET rates during fall. The large differences in the latent heat fluxes between *dry tundra* on the elevated polygon rims and *wet tundra* in the low-lying ice-wedge polygon centers indicate instead considerable differences in the surface energy balance during fall. The rims feature a higher albedo than the lowered centers (Langer et al., 2011b) and almost a similar average surface temperature (Langer et al., 2010). Therefore, it can be excluded that the increased latent heat flux originates from a larger radiation budget at the rims. Furthermore, the

potential differences in ground heat flux between the polygon rims and centers are negligible in fall (about $6\,\mathrm{Wm^{-2}}$) (Langer et al., 2010, 2011b) and can therefore not account solely for the difference in ET rates as suggested by Liljedahl et al. (2011). We conclude that there must be differences in the partitioning of sensible and latent heat fluxes between the polygonal rims and centers. The energy partitioning of sensible and latent heat fluxes is potentially triggered by differences in the surface-air temperature gradients, in the saturation vapor pressure deficit between the surface and the air, or in the resistance to evapotranspiration. However, frequent and high precipitation during the fall period renders the moss canopy of *dry tundra* on the rims equally wet as *wet tundra* in the water-saturated polygonal centers. The rims feature a considerably higher surface roughness than the water-saturated polygonal centers due to the dendritic growth form of the dominant moss species (*Hylocomium splendens*). This difference in growth form of the mosses can strongly modify water loss from the moss canopy (Tallis, 1959; Hosokawa et al., 1964) and potentially lower the resistance to evapotranspiration on the rims. Additionally, the elevated polygonal rims are more exposed to wind, all of which could lead to generally increased turbulent heat fluxes at the polygonal rims with a shift towards higher latent heat fluxes.

2.6.2 *Downscaling land cover*

The distribution of *k*-means classes are similar in both CHRIS Proba and Landsat imagery. This suggests that the underlying land cover fractions did not vary significantly between the different acquisition dates. The mean proportions of land cover types within each *k*-means spectral class show a similar trend for different dates, sensors and resolutions. However, the proportions of the different land cover types within *k*-means Class 2 and Class 3 show a large degree of variability for both CHRIS Proba and Landsat data. In these classes the same spectral signature can result from various combinations of the underlying subpixel-scale land cover composition. This subject requires further investigation in other representative parts of the Delta, on the basis of very high-resolution satellite and radar imagery (resolution less than $4\,\mathrm{m}$).

The high degree of variability in the relative proportions of different the land cover types in CHRIS Proba Class 9 suggests that the high NIR reflectance from short but dry surfaces and also high NIR reflectance from tall but wet vegetation cannot be distinguished using CHRIS Proba data. With the additional surface information available from two SWIR bands, Landsat data is more effective in distinguishing between those dry and wet tundra surfaces. Further investigations regarding the spectral mixing of Arctic land surfaces within coarse-scale resolution satellite data are required to fully understand the physical aspects of the downscaling scheme presented in this study and its applicability to other satellite sensors.

The distribution of *k*-means classes within the delta and their associated subpixel-scale composition is in overall agreement with observations from other studies. Polygonal tundra is primarily found on the first terrace in the central and eastern part of the Delta, whereas the north-western part of the delta is dry (Ulrich et al., 2009; Schneider

et al., 2009) and appears more homogeneous with little or no subpixel-scale heterogeneity. In an area in the southwest Lena River Delta along the Olenek channel, Grosse et al. (2008) mapped 239 ha small open water bodies, while this study estimated an area of 305 ha water surfaces, of which 88 ha was *open water*. The differences are probably not due to inter-annual differences in the surface hydrology as the accumulated precipitation up to the image acquisition dates in 2001 and 2006 only differs by 9 mm, which is unlikely to have caused significant differences in the extent of water surfaces. Differences in the classification of water surfaces might be due to the different spectral ranges of the imagery used for classification (panchromatic versus VNIR) or differences in surface properties of land cover at the site investigated by Grosse et al. (2008) and on Samoylov Island. Differences in surface properties, *e. g.*, the ratio of shrub cover, are likely to affect the spectral characteristics of composite Landsat pixels and associated subpixel-scale estimates of land/water cover, which underlines the importance of detailed field studies to further improve the presented scaling approach.

Misclassifications of the heterogeneous ice-wedge polygonal tundra can occur due to a limited spectral range of the aerial or satellite imagery used for high-resolution land cover mapping. Furthermore, special care must be taken when selecting the study area to ensure that it produces a representative dataset of the subpixel-scale heterogeneity of the landscape in question. In this study, we have been able to show the range of variability in the underlying land cover classes by decomposing each single Landsat pixel, rather than merely looking at the study area as a whole. We could then assign the average proportion of the different land cover types to each spectral class in the satellite data. This empirical downscaling of land cover can be used where standard spectral mixing analyses (SMA) are not successful. SMA procedures rely on the selection of endmembers, *i. e.*, pixels with completely homogeneous land cover. However, the high level of heterogeneity in the ice-wedge polygonal landscape makes it difficult and in the case of *overgrown water* even impossible to select suitable endmembers. In this study, we have therefore used the mean proportions of each land cover type within each *k*-means class to decompose the composite pixels. Further developments include the use of probability distribution functions (PDFs) that ensure the mean, standard deviation and skew of the subpixel-scale variability when disaggregating coarse resolution data (Hill et al., 2011). The success of this approach, however, depends on the quality of the subpixel-scale PDF used: "The PDF must capture the natural heterogeneity at a sufficiently fine resolution to preserve critical ecosystem states and processes" (Hill et al., 2011). Extrapolation of the PDF to larger regions requires the PDF to be spatially representative. In regions with similar land cover types and spectral properties to the ice-wedge polygonal tundra, we would expect to find similar PDFs to those presented in this study. Extending our approach to coarser resolution imagery (*e. g.*, MERIS with 1 km resolution) would mean including flood plains and barren ground that exhibit different spectral signatures from those exhibited by ice-wedge polygonal tundra.

2.6.3   *Implications of subpixel-scale heterogeneity*

Spectral information from Landsat imagery can effectively determine subpixel-scale percentages of *dry tundra* and *open water* surfaces. Some 13 % of the delta's land surface (not including rivers and coastal areas) has been estimated from Landsat data to be occupied by water bodies. However, by including the subpixel-scale land/water fraction, the water surface area increases to 20 %. Classifications based on traditional Landsat analyses may therefore underestimate the water surface area by a factor of 1.5. Databases on even larger scales, such as the Global Lakes and Wetland Database (GLWD) by Lehner and Döll (2004), could underestimate the water surface area of the Lena Delta by a factor of 4. Similar discrepancies have been found by Grosse et al. (2008) who estimated the water surface area detected by high-resolution remote sensing data over three sites in eastern Siberia to be 2 to 7 times larger than those indicated by the GLWD. Assuming the polygonal tundra of Samoylov Island to be representative of the *wet sedge- and moss-dominated tundra* in the Lena Delta as a whole (as classified by Schneider et al. (2009)), we estimate the existence of approximately 6,200,000 small water bodies (smaller than 0.1 ha) to exist in the *wet sedge- and moss-dominated tundra* within an area of 8277 km².

The land cover class *overgrown water* shows the largest variation within our high-resolution aerial land cover classification. This is probably due to the different dates of image acquisition and field mapping, with misclassified sites representing transient water accumulations. *Wet tundra*, *overgrown water* and *open water* bodies represent stages in a landscape sequence that are dependent on the current water level. Their transient nature makes them prone to changes in the inter-annual and seasonal surface moisture regime (Smol and Douglas, 2007; Boike et al., 2008), which presents a key challenge when incorporating temporal changes of fine-scale land cover into the modeling of water, heat and carbon fluxes.

The proportions of ET from *wet tundra*, *dry tundra* and water bodies varied considerably for summer and fall. The results on evapotranspiration of this study can be generalized to the surface energy balance, which is a key element in larger-scale atmospheric models. For polygonal tundra on Samoylov Island, a distinctly different surface energy balance depending on the land cover class has been demonstrated both during summer and winter (Langer et al., 2011b,a), so that it should be calculated independently in modeling approaches. In the case of carbon fluxes, differences between land cover types of ice-wedge polygonal tundra are much higher than for ET (Kutzbach et al., 2004; Sachs et al., 2010) which makes correct fine-scale land cover classifications even more important. *Wet tundra* and *overgrown water* show methane fluxes that are up to 40 and 20 times higher than *dry tundra* and *open water* (Sachs et al., 2010). In this case, misclassifications of land cover at the meter scale can result in large errors at the landscape scale. Schneider et al. (2009), for example, find a much higher water body ratio (30 %) and a much lower ratio of *wet tundra* (8 %) for ice-wedge polygonal tundra on Samoylov Island as compared to this study (16 % and 19 %). Their land cover classification would lead to an underestimation of the areally weighted methane flux by about 40 %.

The classification techniques presented in this study can be used to compile improved fractional distributions for land cover classes within a larger-scale grid, which will facilitate upscaling of the surface energy balance as well as carbon fluxes computed for individual land cover types. A further improvement in the method would include the statistical representation of temporal changes in land cover. It should be emphasized that this approach would account for subpixel-scale heterogeneity in the land cover on a meter scale, simply by reproducing the correct land/water cover statistics within a grid cell.

The preceding discussion highlights the importance of integrating detailed field studies, multi-scale remote sensing data and model schemes in Arctic areas. Such integrated studies would be able to account for highly heterogeneous land cover patterns in large-scale models (Rietkerk et al., 2011), to monitor fine-scale changes of land surface properties (Stow et al., 2004) and to validate existing land cover classifications, especially with regard to the extent of water bodies and wetlands (Frey and Smith, 2007).

2.7 CONCLUSIONS

Resolutions of 4 m or less are necessary, in order to map the fine-scale landscape elements of ice-wedge polygonal tundra. Land cover elements of ice-wedge polygonal tundra are therefore not resolved by CHRIS Proba and Landsat imagery, and any coarser-scale land cover databases. About 90 % of the satellite pixels are composed of patches or fragments of *dry tundra* and *wet tundra* as well as water surfaces. Spectral classification of composite CHRIS Proba and Landsat pixels in areas of ice-wedge polygonal tundra is determined by the relative proportions of *dry tundra* and water within each pixel. Decomposition of composite pixels is therefore possible using sub-meter resolution imagery in the visible and near-infrared to derive subpixel-scale probabilities of land/water cover. The actual land/water proportions within each composite pixel is most effectively captured by Landsat data, which provides more surface information in the SWIR range. The inclusion of subpixel-scale water bodies increases the water surface area of the total land area in the Lena Delta from 13 to 20 %. In order to ensure the validity of these subpixel-scale probabilities, fine-scale land cover mapping must capture the typical heterogeneity of all the relevant land cover classes. This approach, however, is sensitive to the specific surface spectral characteristics of the subpixel-scale land/water covers. Further high-resolution analyses of other typical tundra and wetland areas in permafrost landscapes are therefore necessary.

The land cover types of ice-wedge polygonal tundra exhibit distinctly different seasonal differences in water, carbon and energy fluxes. Under a warming Arctic climate, small water bodies and transient *wet tundra* patches are prone to change and their disappearance or formation may indicate critical thresholds in ecosystem processes. The classification and scaling techniques presented in this study take into account the subpixel-scale heterogeneity of ice-wedge polygonal tundra from mid-summer to late fall on the meter scale. They simply reproduce the actual land cover statistics within a pixel, which can be considered as a prerequisite for reliable large-scale modeling of water, energy and carbon exchange from permafrost areas.

2.8   ACKNOWLEDGMENTS

3

WATER BODY DISTRIBUTIONS ACROSS SCALES: A REMOTE SENSING BASED COMPARISON OF THREE ARCTIC TUNDRA WETLANDS

3.1 ABSTRACT

Water bodies are ubiquitous features in Arctic wetlands. Ponds, *i.e.*, waters with a surface area smaller than 10^4 m², have been recognized as hotspots of biological activity and greenhouse gas emissions but are not well inventoried. This study aimed to identify common characteristics of three Arctic wetlands including water body size and abundance for different spatial resolutions, and the potential of Landsat-5 TM satellite data to show the subpixel fraction of water cover (SWC) via the surface albedo. Water bodies were mapped using optical and radar satellite data with resolutions of 4 m or better, Landsat-5 TM at 30 m and the MODIS water mask (MOD44W) at 250 m resolution. Study sites showed similar properties regarding water body distributions and scaling issues. Abundance-size distributions showed a curved pattern on a log-log scale with a flattened lower tail and an upper tail that appeared Paretian. Ponds represented 95 % of the total water body number. Total number of water bodies decreased with coarser spatial resolutions. However, clusters of small water bodies were merged into single larger water bodies leading to local overestimation of water surface area. To assess the uncertainty of coarse-scale products, both surface water fraction and the water body size distribution should therefore be considered. Using Landsat surface albedo to estimate SWC across different terrain types including polygonal terrain and drained thermokarst basins proved to be a robust approach. However, the albedo–SWC relationship is site specific and needs to be tested in other Arctic regions. These findings present a baseline to better represent small water bodies of Arctic wet tundra environments in regional as well as global ecosystem and climate models.

3.2 INTRODUCTION

Wetlands cover about 8 % ($396,000$ km²) of the non-glaciated Arctic tundra surface (Walker et al., 2005). Low relief and the underlying permafrost impede drainage in these areas, so that the water table is slightly above or below the ground surface. Wetlands are therefore characterized by poorly drained, highly saturated soils as well as abundant ponds and lakes, which support unusually productive habitats in an otherwise dry and barren environment. Organic wetland soils store large amounts of carbon (Tarnocai et al., 2009) and both tundra surfaces and water bodies are a main source of carbon dioxide and methane to the atmosphere (McGuire et al., 2009). A changing Arctic climate may alter the spatial extent of wetlands as well as the number and occurrence of water bodies affecting high-latitude carbon, water and energy fluxes (Chapin III et al., 2000; Avis et al., 2011). Thawing of permafrost may either increase the number of ponds and lakes when

thermokarst depressions fill with water (Jorgenson et al., 2001; Walter et al., 2006), or decrease their number when permafrost thaw results in drainage of water bodies (Yoshikawa and Hinzman, 2003; Smith et al., 2005; Smol and Douglas, 2007). Ponds, *i.e.*, water bodies with a surface area smaller than 10^4 m², are by far the dominant water bodies in Arctic wetlands (Emmerton et al., 2007; Grosse et al., 2008; Muster et al., 2012). They have been recognized as hotspots of biological activity (Smol and Douglas, 2007), carbon dioxide (Laurion et al., 2010; Abnizova et al., 2012) and methane emissions (Laurion et al., 2010; Walter et al., 2006). Abnizova et al. (2012) found that omission of Siberian tundra ponds would mean an underestimation of landscape carbon dioxide emissions of 35 % to 62 %. However, the ponds' impact on regional and global carbon emissions, both current and future, remains difficult to quantify since little information is available regarding their number and occurrence in the Arctic. High-resolution assessments of water bodies including ponds have been conducted only in northeast Siberia (Grosse et al., 2008; Muster et al., 2012), and in the western Canadian Arctic (Emmerton et al., 2007). Global land cover data sets are limited in spatial detail due to their low resolution. The global lakes and wetlands database (GLWD), for example, only includes lakes larger than 10^5 m² (Lehner and Döll, 2004). Moreover, both global and regional land cover data sets can be highly inconsistent (Frey and Smith, 2007; Ozesmi and Bauer, 2002; Brown and Young, 2009), especially in the northern taiga–tundra zone where land cover heterogeneity is high (Pflugmacher et al., 2011). Muster et al. (2012) showed that Landsat data with a resolution of 30 m cannot resolve ponds and results in an underestimation of water surface area in polygonal tundra by a factor of 1.5. Scaling procedures are needed to link high-resolution assessments of pond distribution with spatial resolutions of 4 m or better to the medium- (tens of meter spatial resolution) and low-resolution (hundreds to kilometers spatial resolution) forcing or boundary land cover data sets used in ecosystem and climate models in order to determine the role of Arctic ponds for the regional and global water, energy and carbon balances. Studies have validated circumpolar (Weiss and Crabtree, 2011; Watts et al., 2012) and regional (Hope, 1999; Olthof and Fraser, 2007; Olthof et al., 2008) subpixel information of Arctic surface waters up to resolutions of 30 m. Locally calibrated studies, on the other hand, provide great detail but are limited to small areas (Goswami et al., 2011). Medium-scale Landsat data with a resolution of 30 m provides a link between such high- and low-resolution remote sensing data. Surface albedo has been shown to be proportional to the subpixel surface water fraction. Studies have used this relationship for example to estimate the subpixel fraction of wet bare soil (Idso et al., 1975; Jackson et al., 1976) and melt ponds on sea ice (Fetterer and Untersteiner, 1998; Eicken et al., 2004). We use Landsat surface albedo to estimate the subpixel fraction of open water cover since albedo is a critical physical parameter affecting the Earth's climate and is a standardized parameter implemented in climate models.

This study inventories ponds and lakes in three Arctic tundra wetlands in the Canadian High Arctic, on the Alaska Coastal Plain, and in the Lena Delta in Siberia. High-resolution remote sensing data with resolutions of 4 m or better are used to assess (i) the size distribution of water bodies; (ii) the loss of information on water body number

and water body surface area with decreasing spatial resolution; and (iii) the potential of medium-scale Landsat surface albedo to show the subpixel fraction of open water cover (SWC).

3.3 STUDY AREAS

Study areas are Polar Bear Pass on Bathurst Island in the Canadian High Arctic, Samoylov Island in the Lena Delta in Siberia, Russia, and the Barrow Peninsula on the Alaska coastal plain (Figure 14).

The study area on Samoylov Island (SAM) is located in the Lena River Delta, 120 km south of the Arctic Ocean (72° 22′ N, 126° 30′ E) (Figure 14(b)). SAM is the smallest of the three study areas with 1.76 km² (Table 6). It is characterized by thermokarst lakes surrounded by low-centered ice-wedge polygonal tundra. Polygonal tundra is composed of elevated dry polygonal rims interspersed with wet depressed polygonal centers and numerous small polygonal ponds (Fig. 14(a)). Few high-centered polygons are typically found along lake margins and on elevated plateaus. Polygonal tundra represents about 30% of the Lena River Delta's land surface (Muster et al., 2012).

The wetland area of Polar Bear Pass (PBP) is the second largest wetland in the Canadian High Arctic (75° 40′N, 98° 30′W). It is a shallow valley running east-west across south-central Bathurst Island with a surface area of about 94 km² (Young et al., 2013) (Figure 14(c)). The wetland is bordered by hills reaching about 240 m above sea level. Runoff from the adjoining hillslopes moves both water and matter into the wetland zone (Woo and Young, 2006), creating an unusually productive habitat within a polar desert environment.

The Barrow study area (BAR) is located about 10 km south of Barrow on the Arctic Coastal Plain of northern Alaska (71° 15′ N, 156° 33′ W) (Figure 14). It is the largest of the three sites with an area of about 354 km² encompassing polygonal terrain, shallow, oriented thaw lakes, and drained thaw lake basins (Brown et al., 1980; Hinkel et al., 2003).

All three sites are peat-forming lowland wetlands underlain by continuous permafrost. Regional climates are characterized by long, dry, cold winters and short, moist, cool summers, with PBP exhibiting the coldest and driest climate of the study areas (Table 6). The snow-free period for BAR and SAM lasts from mid-June to mid-September, but is much shorter at PBP from mid-July to end of August. Vegetation at all three sites can be characterized as predominantly wet tundra with abundant sedges, grasses, mosses and dwarf-shrubs less than 40 cm in height. According to the Circumpolar Arctic Vegetation Map (CAVM) SAM and BAR are situated within wetland complexes identified as sedge, moss dwarf-shrub wetland and sedge/grass moss wetland, respectively (Walker et al., 2005). The PBP wetland area does not appear on the CAVM as it is smaller than the minimum CAVM mapping unit of 196 km². However, sedge/grass, moss wetlands can be found on Bathurst Island and throughout the Canadian High Arctic. Moreover, the Northern Land Cover Classification (NLCC) classifies about 70 % of the PBP wetland area as wetland, wet sedge or water (Olthof et al., 2008).
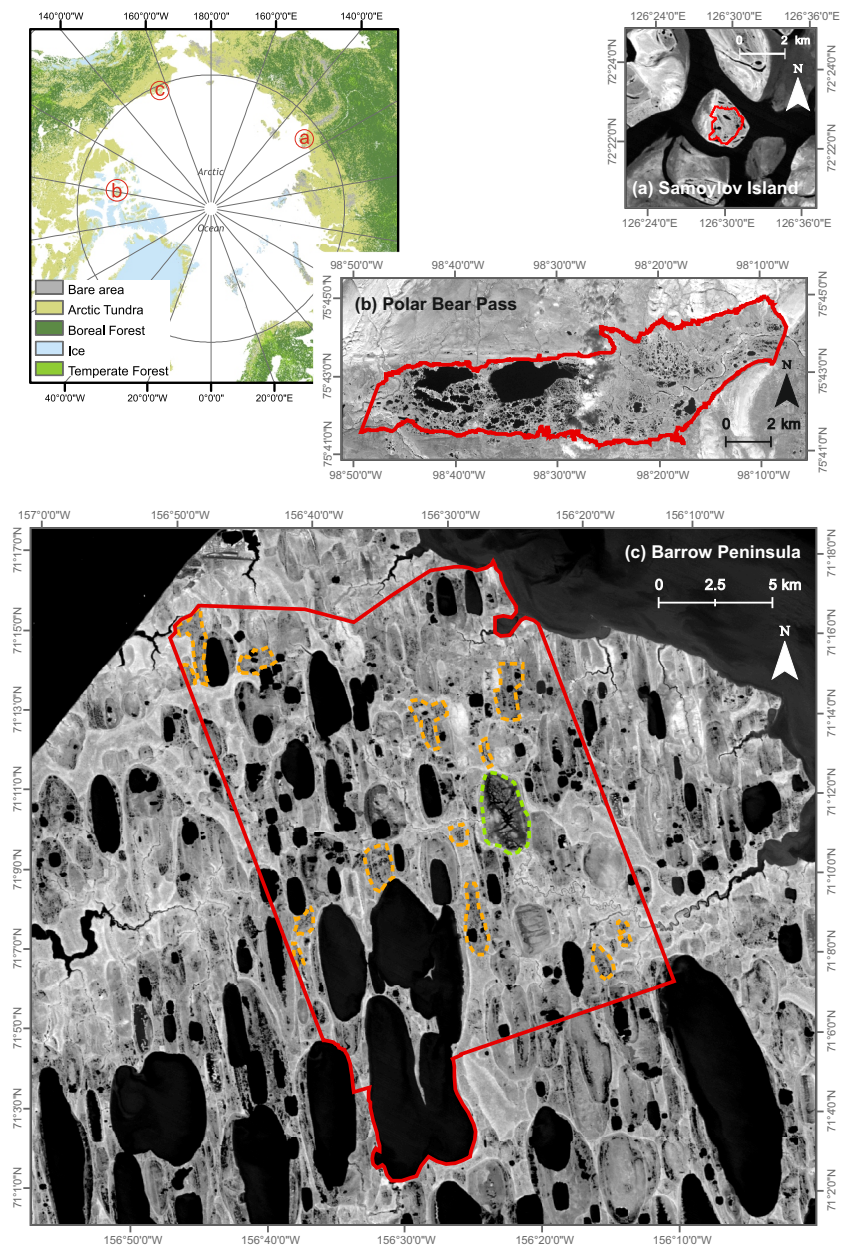
Figure 14: Location of study areas in the Arctic. (**a**) Samoylov Island, Lena Delta, Siberia, Russia; (**b**) Polar Bear Pass, Bathurst Island, Canada; and (**c**) Barrow Peninsula, Alaska, USA. Red lines mark the study areas. In the Barrow study area, orange lines mark selected polygonal terrain, green line marks a drained, vegetated thermokarst basin.

Table 6: Site characteristics of the study areas Polar Bear Pass (PBP), Samoylov Island (SAM), and Barrow Peninsula (BAR).

	PBP	SAM	BAR
Location	75°40′N, 98°30′W	72°22′N, 126°30′E	71°18′N, 156°33′W
Study area [km²]	68.6	1.76	353.6
Permafrost depth [m]	100 to 500 m [a]	500 to 600 m [e]	⩾ 300 m [g]
Active layer depth [m]	0.3 to 1 m [b]	0.4 to 0.9 m [f]	0.3 to 0.9 m [h]
Climate characteristics			
Climate regime	polar desert [c]	arctic-continental	cold maritime
Station	Resolute Bay	Samoylov Island	Barrow
Years	1971–2000	1961–1999	1977–2009
Mean annual air temperature	−16.4 °C	−13.6 °C [f]	−12 °C [i]
Mean July air temperature	4.3 °C [b]	10.1 °C [f]	3.3 °C [i]
Mean summer precipitation	94 mm [d]	125 mm [f]	72 mm [i]
References	[a] Smith and Burgess (2002)	[e] Grigoriev (1960)	[g] Brown and Johnson (1965)
	[b] Abnizova et al. (2012)	[f] Boike et al. (2013)	[h] Hinkel and Nelson (2003)
	[c] Young and Labine (2010)		[i] Liljedahl et al. (2011)

[d] Field measurements 2008&2009

3.4 MATERIAL AND METHODS

3.4.1 *Processing of remote sensing data*

For each study area, high-resolution imagery with spatial resolutions of 0.3 to 4 m was used to map open water cover. Available high-resolution data included TerraSAR-X imagery for PBP at 2 m resolution, visible and near-infrared (VNIR) aerial photographs for SAM at 0.3 m resolution, and multispectral KOMPSAT-2 imagery for BAR at 4 m resolution (Table 7). Pixel-based classifications of water surfaces were converted from raster to vector files in order to identify contiguous water bodies as discrete objects. GIS analysis of vector data yielded the information about number and size of water bodies. High-resolution water body maps were compared with water body maps based on Landsat-5 TM at 30 m resolution and the MODIS water mask (MOD44W) at 250 m resolution (Carroll et al., 2009). The analysis of water body size distributions included only frost cracks, ponds, and lakes with a minimum surface area of 1 m² for SAM and 5 m² for PBP

Table 7: Sensor type, resolution, water detection thresholds, and acquisition dates of remote sensing data for the study areas Polar Bear Pass (PBP), Samoylov Island (SAM) and Barrow Peninsula (BAR). Water detection thresholds are in sensor specific units, i.e. reflectance [ρ], digital number [DN], and backscattering coefficient [ff°_{db}].

SITE	SATELLITE SENSOR	RESO- LUTION [M]	WATER DETECTION		DATE
			BAND	THRESHOLD	
PBP	TerraSAR-X	2	HH	$< -21.55\,ff^{\circ}_{db}$	13 August 2009
	Landsat-5 TM	30	NIR	0 to 0.03 ρ	28 August 2009
SAM	VNIR aerial photography	0.3	NIR	0 to 5438 DN	1, 9 and 15 August 2008
	Landsat-5 TM	30	NIR	0 to 0.03 ρ	25 July 2007
BAR	KOMPSAT-2	4	NIR	46 to 139 DN	2 August 2009
	Landsat-5 TM	30	NIR	0.01 to 0.07 ρ	15 July 2009

and BAR. All remote sensing data were processed using the image processing software ENVI 4.8 (ITTVIS) and ArcGIS 10 (ESRI).

3.4.1.1 *VNIR aerial imagery of SAM*

Aerial images of Samoylov Island were obtained by mounting two Nikon D200 cameras on a helium-filled blimp. Images were acquired in the visible (VIS) from about 400 to 690 nm and near-infrared (NIR) ranges above about 830 nm (together referred to as the VNIR range). The Nikon D200 has a radiometric resolution of 24 bit per pixel. The flights took place at noon on sunny, cloudless days (1, 9 and 15 August 2008). An average flying altitude of 750 m resulted in a pixel size of about 0.14 m. Sixteen images were used to map the ice-wedge polygonal tundra on Samoylov Island, with an image overlap of about 25 %. Land cover classification was carried out individually for each VNIR image. Open water surfaces were extracted using a density slice classification applied to the NIR band. A relative classification accuracy was calculated by comparing the classifications for overlapping areas of adjacent images. In areas where aerial photographs overlapped the land cover classification varied by about 3 % on average (Muster et al., 2012).

3.4.1.2 *TerraSAR-X and SPOT-5 imagery of PBP*

The TerraSAR-X (TSX) image was acquired on 13 August 2009 in Stripmap mode with HH polarization and an incidence angle of 33.29°. The image was obtained as Single Look Slant Range Complex (SSC) and transformed to Single Look Complex (SLC) with the Gamma software (Werner et al., 2000). Multilook processing was applied to reduce speckle noise with 3 looks in range and 2 looks in azimuth. Radio-

metric calibration of the multilook image was done according to Fritz et al. (2007) using the following equation:

$$\sigma^\circ = \left(Ks * DN^2 - NEBN \right) \tag{9}$$

where the digital number, DN, *i. e.*, the amplitude of the backscattered signal of each pixel, was transformed into a backscattering coefficient, σ°, corrected for sensor noise, NEBN (Noise Equivalent Beta Naught), on a linear scale. This calibration takes into account the calibration constant, Ks, which is provided in the image data. Correction for variation in local incidence angle with terrain was neglected due to the low gradient of topography in the study area.

The backscattering coefficients were then calculated in decibels by the following formula:

$$\sigma^\circ_{db} = 10 * \log_{10} \left(\sigma^\circ \right) \tag{10}$$

The resulting multi-looked image was geocoded to UTM WGS84 using a look-up table based on a DEM (Wegmuller, 1999) which was generated from Canadian Digital Elevation Data 1:50,000 (Geomatics Canada, 2006). The remaining signal-dependent noise SAR speckling was reduced by the application of a 11 by 11 pixel Gamma filter (Shi and Fung, 1994).

For the PBP study area, a pixel threshold for water body delineation was fitted according to reference data from high-resolution aerial photography and field mapping for a small area of about 500 m². Consequently, pixels with brightness values $< -21.55\,\sigma^\circ_{db}$ were classified as open water. A majority filter with a kernel size of 7×7 pixels was applied to reduce spurious pixels in the classification. The PBP wetland zone was defined as all area below elevations of 30 m, and only water bodies that did completely fall within this zone were considered for analyses.

A SPOT-5 image from 25 August 2009 was available for the study area. The image had a resolution of 10 m in multispectral mode with four bands ranging from 500 to $1,750$ nm. The image was used as ancillary information to confirm the TSX-based water classification with the help of the NIR band.

3.4.1.3 *KOMPSAT-2 imagery of BAR*

Two acquisitions of KOMPSAT-2 were available on August 2, 2009. KOMPSAT-2 provides imagery with a single panchromatic band between 500 and 900 nm at 1 m resolution and four spectral bands between 450 and 900 nm at 4 m resolution. Radiometric resolution of the sensor is 10 bit per pixel. Open water surfaces were extracted using a density slicing applied to the NIR band at 4 m resolution. Cloud shadows were removed manually from the water body classification.

3.4.1.4 *Landsat-5 Thematic Mapper (TM)*

The Landsat-5 TM images were corrected towards surface reflectance values using Chavez-COST based corrections (Chavez, 1996; Chander

et al., 2009) including the Dark Object Subtraction (DOS) and the CO-Sine Transmittance (COST) effects. The image-based DOS compensates for the atmospheric scattering (Chavez, 1988). We subtracted the signal of the atmosphere so that surface reflectances of tundra were in the range of 0.06 to 0.10 in the red and 0.10 to 0.27 in the near-infrared range.

The Landsat calibration tool in ENVI 4.8 (ITTVIS) normalizes the Landsat at-sensor radiance data against the solar irradiance (Thuillier et al., 2003) and for yearly variations in the Sun-Earth distance. According to the Chavez-COST method (Chavez, 1996), the COSine effect accounts for different solar zenith angles. We did not correct for the cosine-dependant atmospheric transmittance as the COST method handles this variable optionally and does not recommend it for low sun elevation angles.

The reflectance, ρ, is defined as

$$\rho = \frac{\pi \left(L_{sat} - L_{path} \right) d^2}{ESUN_\lambda \cos\theta_s} \tag{11}$$

where L_{sat} = spectral radiance at sensor [$Wm^{-2}sr^{-1}$—m] , L_{path} = atmospheric path (relative scattering component (Chavez, 1988)), d = Earth-Sun distance [astronomical units], ESUN = mean exoatmospheric solar irradiance [Wm^{-2}—m]], $\cos\theta_s$ = COSine effect, and θ_s = Solar zenith angle [°].

Classification of water bodies from Landsat data was done using a density slicing of the NIR band. The pixel threshold value that resulted in the closest agreement between Landsat water body area and high-resolution water body area was chosen.

3.4.1.5   *MODIS water mask*

For the area from 60°N to 80°N the MODIS water mask (MOD44W) was derived from Terra MODIS data MOD44C 250 m 16-day composites. Data from May to September of three years (2000–2002) was used (Carroll et al., 2009). Data were classified using regression tree classification, which yields a subpixel estimate of the water component of a pixel. Features were determined to be water bodies if the averaged classification result showed a water content of 50 % or greater. Water pixels were included in the final product when a pixel was identified as water at least 50 % of the time during the observation period between 2000 and 2002 (Mark Carroll, personal communication, February 4, 2013).

3.4.2   *Accuracy assessment of water body classification*

Robust threshold methods were selected to extract open water surfaces from the high-resolution imagery as well as the Landsat-5 TM data in this study. Water absorbs most of the incoming irradiation in the near-infrared (NIR) and the X-band of the electromagnetic spectrum so that water bodies appear very dark in these spectral bands. Open water can therefore be mapped applying a threshold in a NIR or X-band that divides land and water pixels. The cut-off value is extracted individually for images due to different illumination and acquisition geometry and different sensor spectroradiometry. The NIR threshold method has

been shown to produce similar or even better results compared with multispectral classifications (Braud and Feng, 1998; Frazier et al., 2000; Roach et al., 2012). Moreover, threshold-slicing in the NIR wavelength region allows to extract water pixels that appear atypical in the visible spectral wavelength range due to sky glint, turbidity, and lake bottom reflectance, which are common at high latitudes due to low sun zenith and abundance of shallow water bodies.

In the case of medium-scale data like Landsat with a resolution of 30 m, high-resolution aerial photography as well as high-resolution satellite imagery is used as "ground truth" to evaluate the accuracy of lake classification (Roach et al., 2012; Frazier et al., 2000; Ramsey III and Laine, 1997). In this study, neither image nor field data were available at a sufficient resolution to evaluate the high-resolution water body classifications. However, in the near-infrared as well as in the X-band grey values in the images show a sharp contrast between the water body and the surrounding tundra and classification accuracy is expected to be high (Figure 15). Nevertheless, two types of errors may affect the accuracy of water body classification, *i.e.*, omission errors and commission errors.
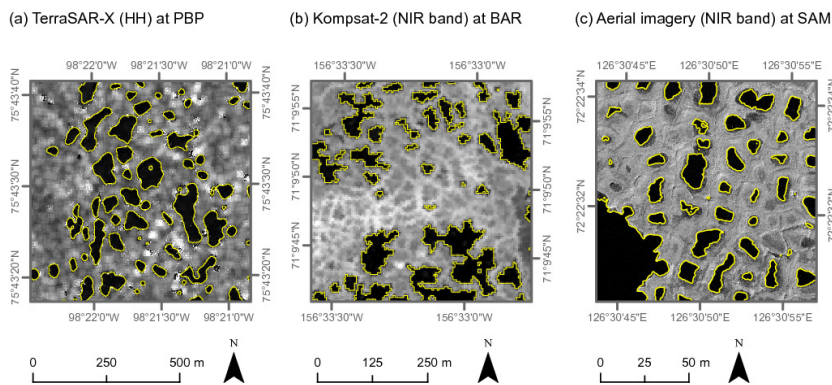
Figure 15: Subsets of study areas show detailed views of water body classifications from (a) TerraSAR-X imagery for Polar Bear Pass (PBP) with a resolution of 2 m, (b) Kompsat-2 NIR imagery for Barrow Peninsula (BAR) with a resolution of 4 m, and (c) NIR aerial imagery of Samoylov Island (SAM) with a resolution of 0.14 m.

Omission errors are due to low spatial resolution so that smaller water bodies are not mapped. Omission errors can be ruled out for SAM and PBP with image resolutions of 0.18 and 2 m, respectively. Omission errors may occur for BAR with a resolution of 4 m.

Commission errors depend on the spectral resolution of the remote sensing data so that a spectral signal is misinterpreted as water where in reality it may be wet soil. In the near-infrared, commission errors may occur for single pixels where small patches of wet soil or shadows due to microtopography or clouds are misinterpreted as water. Cloud shadows can be ruled out with the help of all four bands (R, G, B, NIR) available for the Kompsat-2 imagery and the aerial imagery.

In the X-band, rough water surfaces due to high wind speeds may be confounded as tundra surfaces as the X-band is very sensitive to surface roughness. However, wind speeds were low during acquisition time of the TSX image and water surfaces were calm. Furthermore, wet

snow or wet soil as well as shadows may show the same threshold as open water in the X-band. Based on field observations of PBP, no snow persisted in the study area in mid-August. Wet soil and shadows due to microtopography appear in patch sizes much smaller than the minimum size pond threshold of 5m² and were excluded from the classification. A SPOT-5 image (from 25 August 2009) with a resolution of 10m was used to visually check the water body classification from the TSX image and remove any pixels falsely identified as water. All water bodies identified in the SPOT image were also identified in the TerraSAR-X image.

3.4.3   *Subpixel analysis of Landsat surface albedo*

We investigated the relationship between surface albedo, α, calculated from the Landsat surface reflectance, ρ, and the subpixel water cover (SWC) within each Landsat pixel. This study and others (*e. g.*„ (Brest and Goward, 1987; Duguay and Ledrew, 1992; Liang, 2000)) use the broad-band reflectance as the surrogate for the integrated hemispherical albedo. Albedo is defined as the fraction of incident radiation that is reflected by a surface. While reflectance is defined as this same fraction for a single incidence angle, albedo, in its strict sense, is the directional integration of reflectance over all sun-view geometries. For sensors with wide-viewing angles like MODIS, AVHRR, SeaWIFS and MERIS, bi-directional distribution function (BRDF) corrections are needed. The Landsat sensor, however, has a viewing angle of only 15°. First BRDF measurements of tundra North of 70° using a field goniometer show that the anisotropy effect would account for maximal 1% albedo for the backward looking ($-7.5°$) viewing geometry and for smaller than 0.5% albedo for the forward looking geometry ($+7.5°$) viewing geometry at the outermost pixels of a Landsat acquisition depending on the sun azimuth (Marcel Buchhorn, personal communication, February 2, 2013). Within this study, the regions of investigations comprised only subsets of the Landsat acquisitions with minor anisotropic effects.

Ninety-eight percent of the solar radiation received at the Earth is in the range of about 0.3 to 2.5 µm, which is covered by Landsat. Broad-band Landsat surface albedo was calculated from Landsat band reflectances from band 2 (520–600 nm), 4 (760–900 nm) and 7 ($2,080$–$2,350$ nm) according to the formula by Brest and Goward (1987) and Duguay and Ledrew (1992) for vegetated surfaces:

$$\alpha = 0.526\rho_{band2} + 0.362\rho_{band4} + 0.112\rho_{band7} \tag{12}$$

Duguay and Ledrew (1992) used this formula for albedo estimation of alpine tundra environments. The formula has since been validated by Liang (2000). Liang (2000) conducted radiative transfer simulations under varying atmospheric and surface conditions to show that it is possible to calculate coefficients for narrow- to broadband albedo conversion for a range of different sensors. Liang (2000) showed that the linear formula by Duguay and Ledrew (1992) fit their data of all cover types well, including soil, vegetation canopy, water, wetland, snow, rock, and other cover types.

The main target of this study were mixed pixels, *i.e.*, pixels with SWC between less than 95% and more than 5%. Spectra of Landsat

mixed pixels are most often characterized by the reflectance of the vegetative component within the pixel. Therefore, the albedo formula for vegetated surfaces was selected and then applied to all Landsat pixels.

Surface water extent in permafrost terrain is strongly affected by seasonal processes, including inundation after snowmelt, progressing thaw depth, evaporation, and precipitation. Whenever possible, high-resolution images and Landsat data were chosen to be from the same year and season, *i.e.*, late summer (Table 7). For SAM, Landsat data was not available for the same year as the aerial imagery, *i.e.*, 1, 9 and 15 August 2008. Instead, Landsat imagery from 25 July 2007 was used. Water balance on Samoylov Island is usually equilibrated, so that water levels and the corresponding water surface area of ponds and lakes do not change significantly for the years of interest (Boike et al., 2013).

For subpixel analysis, the VNIR aerial imagery and KOMPSAT-2 imagery were registered onto the Landsat imagery in ERDAS IMAG-INE 9.2 with a root mean square error of less than 0.5 and 1.6 pixel, respectively. All water surface types, *i.e.*, ponds, lakes, frost cracks, rivers, and streams were used for the calculation of subpixel open water cover (SWC). Maps of open water surfaces derived from high-resolution imagery were then used to calculate the SWC within each Landsat pixel. Consequent analysis of the relationship between SWC and albedo was done for albedo values with a minimum of five repetitions.

3.5 RESULTS

3.5.1 *Abundance and size distribution of water bodies*

Water bodies at all three sites were dominated in number by ponds, *i.e.*, water bodies with a surface area smaller than 10^4 m², but dominated in area by a few large lakes (Figures 16 and 17(a)). The total number of water bodies (area-normalized per 10^7 m²) was about a magnitude higher at SAM than at PBP and BAR (Table 8). The study area at SAM featured only polygonal tundra. Thermokarst lakes contributed less than 1% to the total water body number and showed maximum surface areas of 4.1×10^4 m². The larger study areas of PBP and BAR, however, featured a greater variety of pond and lake sizes. Maximum lake surface area was 5.6×10^6 m² for PBP, and 4.7×10^7 m² for BAR.

The proportion of ponds to the total water surface area diminished with an increasing number of large lakes in the study areas (Figure 16). BAR showed a total pond surface area of only 4 %, followed by PBP with 22 %, and SAM with 49 %. However, ponds contributed more than 95 % to the total number of water bodies in each study area. Even ponds with a surface area of 10^3 m² or less remained a dominant group contributing 60 % to the total number of water bodies at PBP, 87 % at BAR and 99 % at SAM (Figure 16). At BAR, the minimum water body size was 16m² and increased in a stepwise pattern of 4×4 m, which reflected the pixel size of the KOMPSAT imagery used for water body delineation.

Visually, the upper tail of the high-resolution size distributions fit well a Pareto distribution. The Pareto distribution is a power law probability distribution in the form of $N = xA^y$, which appears linear
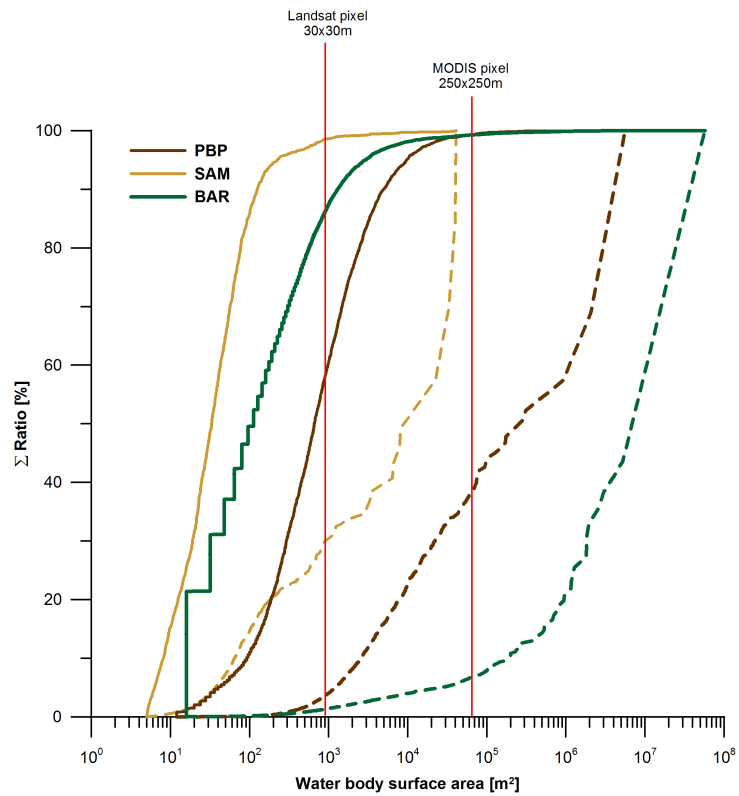
Figure 16: Cumulative ratio of water body surface area to the total
water surface area (dotted lines) and cumulative ratio of
number of water bodies per surface area to the total abun-
dance (thick lines) for Polar Bear Pass (PBP), Samoylov Is-
land (SAM) and Barrow Peninsula (BAR). Vertical lines in-
dicate the pixel size of Landsat with 30×30 m and MODIS
with 250×250 m.
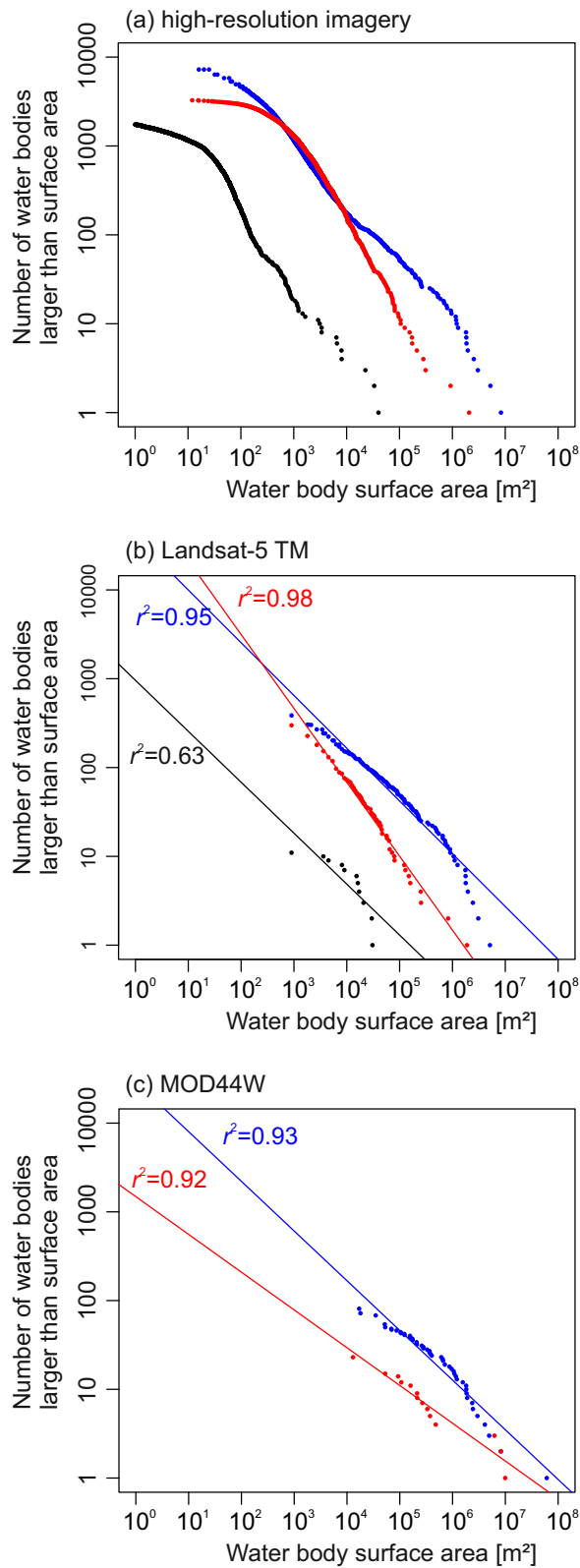
Figure 17: Size distributions of water bodies for Polar Bear Pass (PBP) in red, Samoylov Island (SAM) in black and Barrow Peninsula in blue on a double logarithmic scale (base 10). Size distributions are derived from (**a**) high-resolution imagery with resolutions of 4 m or better; (**b**) Landsat-5 TM imagery with a resolution of 30 m; and (**c**) from the MODIS water mask (MOD44W) with a resolution of 250 m. No water bodies were mapped for SAM from MOD44W.

on a log-log plot. Using the Pareto distribution, however, to extrapolate missing data in the lower tail of the distribution would lead to an overestimation of small water bodies. Size distributions of ponds and lakes at all sites appeared linear on a log-log plot in the upper tail of the distribution, *i. e.*, for water bodies larger than about $400\,m^2$ for PBP, $30\,m^2$ for SAM and $100\,m^2$ for BAR (Figure 17). Water bodies smaller than these thresholds, *i. e.*, in the lower tail of the size distribution, showed no substantial increase in lake abundance. Since the smallest and largest lakes differed in size for the study areas, distribution curves were located at different points along the abscissa.

Landsat- and MODIS-based size distributions at PBP and BAR (Figure 17(b,c)) do not show the flattened lower tail. Linear regressions on the log-abundance log-size plots show high r^2 values of 0.98 for PBP and 0.95 for BAR (Figure 17(b)) and could therefore be mistaken for power-law distributed data. Landsat-based size distribution of SAM, however, significantly deviates from linearity with a r^2 value of only 0.63.

Table 8: Descriptive statistics of water bodies $\geqslant 5\,m^2$ in the study areas of Polar Bear Pass (PBP), Samoylov Island (SAM) and Barrow Peninsula (BAR).

	SAM	PBP	BAR
Number of water bodies	1342	3293	9225
Number of ponds ($< 0.01\,km^2$)	1338	3133	9049
Number of lakes ($\geqslant 0.01\,km^2$)	4	160	176
Total water body area [m^2]	$2.7 * 10^5$	$1.8 * 10^7$	$1.0 * 10^8$
Maximum size [m^2]	$4.1 * 10^4$	$5.6 * 10^6$	$4.7 * 10^7$
Minimum size [m^2]	5.0	12.0	16.0
Mean size [m^2]	200	$5.5 * 10^3$	$1.1 * 10^4$
Median size [m^2]	30	700	100
Standard deviation [m^2]	$1.9 * 10^3$	$1.1 * 10^5$	$5.1 * 10^5$
Normalized per $10^7\,m^2$			
Total number of water bodies	76216	4804	2609
Number of ponds	75989	4571	2559
Number of lakes	227	233	50

3.5.2   *Effect of scale on water body mapping*

Water body surface area and water body number derived from the high-resolution imagery were set to 100% for comparative purposes with water body mapping based on Landsat-5 TM and the MODIS water mask (MOD44W) (Figure 18). Water surface area mapped with Landsat amounted to 64 % of the total water surface area at PBP, 44 % at SAM, and 95 % at BAR (Figure 18). For PBP and BAR, MOD44W showed a close agreement with the actual water surface area (Figure 18). The spatial distribution, however, of ponds and lakes changed for both Landsat and MOD44W, which can be seen in Figure 19. At PBP, clusters of ponds and small lakes converged into larger continuous water bodies. This effect was most pronounced for MOD44W but is also present for Landsat based mapping. The convergence of small

water bodies in close proximity can be expected in coarse resolution datasets from Landsat and/or MODIS as compared with field data or very fine resolution remote sensing because the pixel size does not permit distinguishing sub-pixel lakes as individual entities.
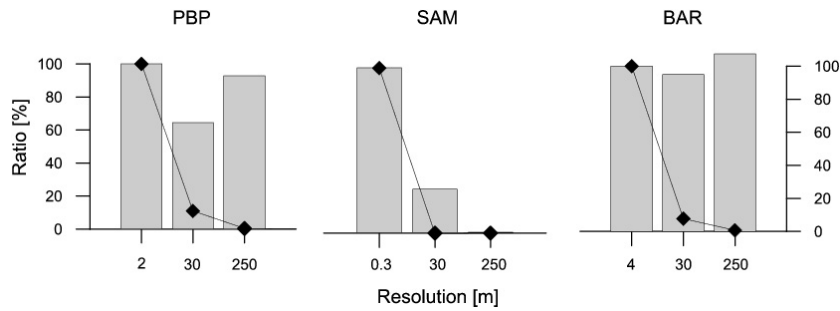
Figure 18: Water body surface area and water body number mapped at different resolutions for Polar Bear Pass (PBP), Samoylov Island (SAM) and Barrow Peninsula (BAR). Bars show the ratio of water surface area to the total water body surface area mapped at the highest resolution. Lines show the ratio of water body number to the total number mapped at the highest resolution. Water bodies were mapped at PBP from TSX imagery with 2 m, at SAM from VNIR aerial imagery with 0.3 m, and at BAR from KOMPSAT-2 imagery with 4 m resolution. 30 m resolution water body maps were derived for all sites from Landsat-5 TM imagery. Water bodies at 250 m were extracted from the MODIS water mask (MOD44W) (Carroll et al., 2009).

Underestimation of the number of water bodies was even stronger than underestimation of the water surface area. At SAM, only 0.8 % of the total water body number could be detected with Landsat, 8 % at BAR, and 13 % at PBP. Water body number further decreased in MOD44W with a resolution of 250 m (Carroll et al., 2009) to less than 1 % at PBP and BAR, and no water bodies were detected at SAM.
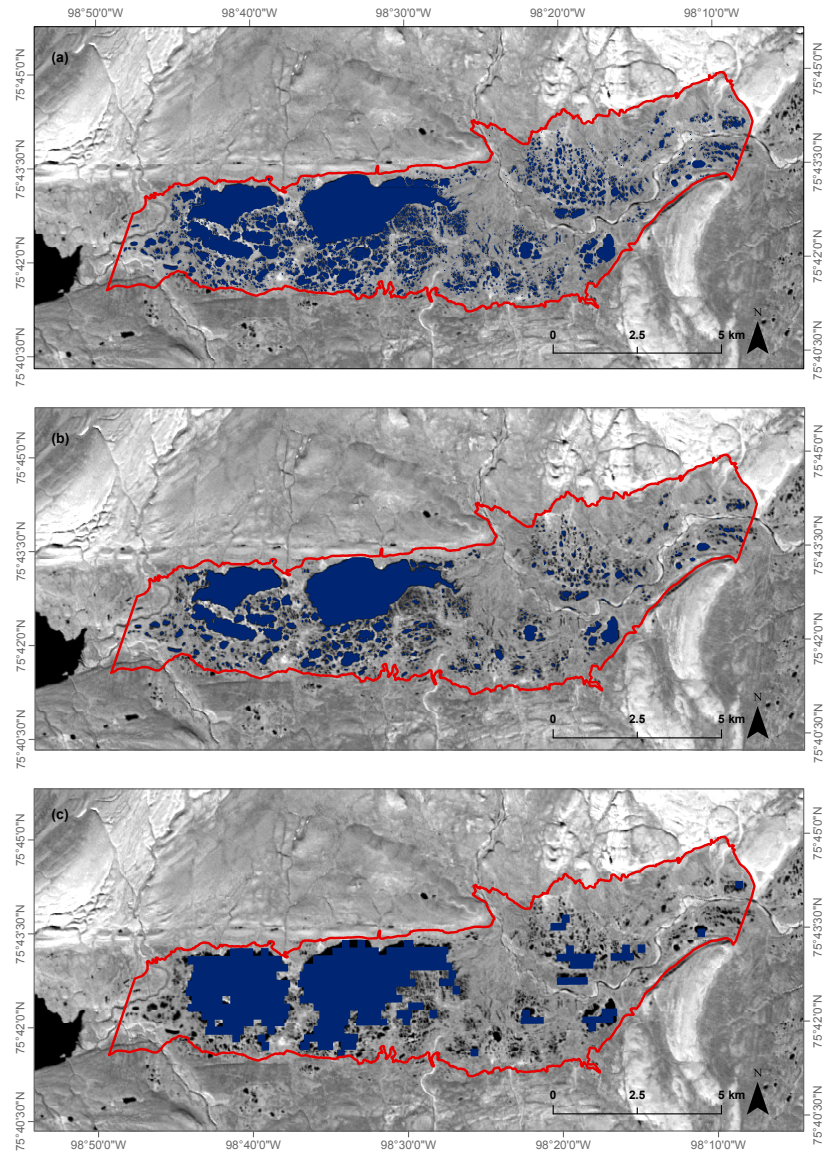
Figure 19: Water bodies (blue areas) in Polar Bear Pass (PBP) mapped at different resolutions from (**a**) TerraSAR-X imagery (HH polarization) with 2 m resolution; (**b**) Landsat-5 TM imagery with 30 m resolution; and (**c**) MODIS water mask (MOD44W) with 250 m resolution (Carroll et al., 2009). Red line marks the study area.

3.5.3 *Subpixel analysis of Landsat albedo*

To characterize Landsat surface albedo in the study areas, pixels were grouped into three categories: water pixels (SWC of 95 % and higher), land pixels (SWC of 5 % and lower) and mixed pixels (SWC between 95 % and 5 %).

Mean water albedo and mean land albedo were similar across study sites (Figure 20). However, land albedo showed a much wider range at PBP and BAR than at SAM. The mean albedo values of water pixels ranged from 0.05 at SAM and BAR to 0.06 at PBP (Figure 20(a)). Outliers of water albedo were predominantly associated with water pixels along pond and lake margins or with water bodies that were close to the Landsat resolution of 30 m in width and/or length. The mean albedo values of land pixels ranged from 0.12 at SAM to 0.13 at PBP and BAR (Figure 20(b)) which were associated with wet tundra. Land albedo reached maxima of 0.25 for PBP, 0.15 for SAM, and 0.17 for BAR. At PBP, albedo values larger than 0.17 were associated with alluvial gravel deposits of the flood plain and sandy-gravel ridges with little to no vegetation within the wetland. At SAM, albedo values larger than 0.13 represented Landsat pixels dominated by dry tundra. BAR land pixels showed lowest albedo values of less than 0.08, which were associated with drained thermokarst basins.

For all sites, SWC decreased with increasing albedo (Figure 21(a)). The albedo–SWC relationship appeared strongly linear for mixed pixels at PBP and SAM, but less so for BAR. Between albedo 0.06 and 0.08 at SAM, SWC was about 10 % higher than the linear relation predicts. BAR exhibited lowest albedo for mixed pixels, and albedo showed about 20 % to 50 % less SWC than at PBP and SAM. The albedo–SWC relationship of PBP and SAM differed between 10 % and 20 % SWC. For all sites, the mean standard deviation (SD) of SWC was equal to or less than 1% for water and land pixels. SWC of mixed pixels showed an SD of 27 % for BAR, followed by PBP with 26 %, and SAM with 21 %. At all sites, SD decreases towards the upper and lower end of the function.
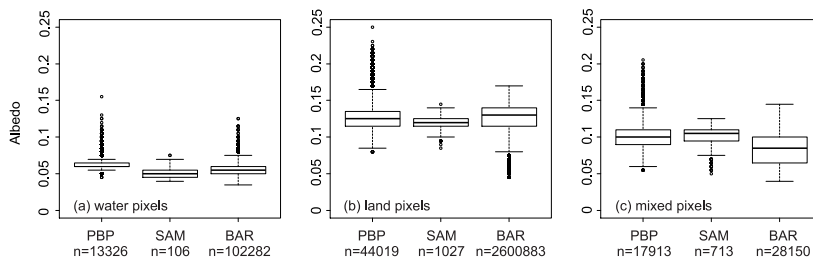
Figure 20: Range of Landsat albedo values for Polar Bear Pass (PBP), Samoylov Island (SAM) and Barrow Peninsula (BAR) for (**a**) water pixels; (**b**) land pixels; and (**c**) mixed pixels. Boxplots show minimum, lower quartile, median, upper quartile, maximum, and outliers.

The BAR albedo–SWC function shown in Figure 21(a) includes the whole study area. BAR, however, was composed of many different terrain types like polygonal terrain and depressed thermokarst basins for which separate albedo–SWC functions were calculated (Figure 21(b)).
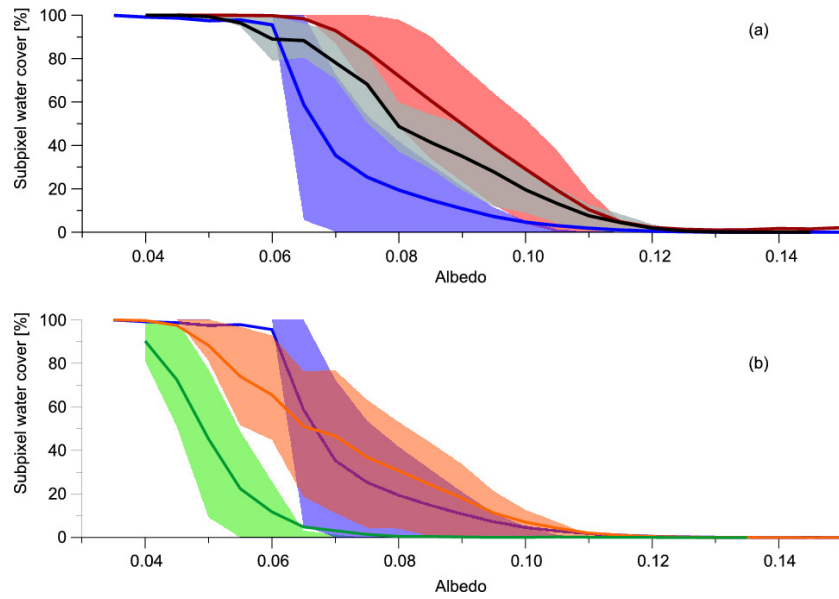
Figure 21: Mean subpixel proportion of open water cover per Landsat surface albedo. Corresponding shaded areas show the 20th and the 80th percentile of the data. Panel (**a**) shows the total study areas of Polar Bear Pass (PBP) (red line), Samoylov Island (SAM) (black line), and Barrow Peninsula (BAR) (blue line); Panel (**b**) shows the mean subpixel proportion of water cover per Landsat albedo for the total BAR study area (blue line), for polygonal terrain (orange line) and a vegetated, drained thermokarst basin (green line), only.

Although SD did not improve significantly with 24 % for polygonal terrain and 27 % for the thermokarst basin, the relationship between SWC and albedo appeared strongly linear for each landscape subtypes compared with the albedo–SWC relationship for the whole study area. The range of albedo in the thermokarst basin was significantly lower than for the other areas. Albedo of polygonal terrain of BAR was within the albedo range of PBP and SAM but SWC was lower.

3.6   DISCUSSION

3.6.1   *Size distribution of ponds and lakes across scales*

Circumpolar and global water body mapping is limited by the low spatial resolution of large-scale imagery. Previous studies therefore attempted to estimate small water bodies that could not be mapped. The linear behaviour of the size distributions for larger water bodies has been used to estimate smaller water bodies using the Pareto distribution (Hamilton et al., 1992; Lehner and Döll, 2004; Downing et al., 2006; Grosse et al., 2008). In the present study, however, application of the Pareto distribution would lead to an overestimation of the number of small water bodies. In all three wetlands, resolutions of 0.3 to 4 m make water body mapping nearly complete. The flattened lower tail is therefore very likely an inherent property of the size distributions. Similar flattened tails have been observed by Seekell and Pace (2011)

and McDonald et al. (2012) for study areas in the United States. In a recent study, Seekell et al. (2013) compare lake data from a mountainous and a flat region and attribute difference in lake size distributions due to the differences in topography. Seekell et al. (2013) suggest that the power-law relationship, *e.g.*, in form of a Pareto distribution, is confined to flat regions. This does not conform to results from this study where size distributions do not appear Paretian although all study sites are located in flat regions. However, their lake sizes from the flat region are derived from Landsat with a minimum lake size threshold of 10^4 m and omit smaller water bodies that are found in the study area (Verpoorter et al., 2012). This study indicates that Landsat- and MODIS-based water body size distributions can be mistaken to follow a power law function whereas higher resolution water body classifications reveal that this is not the case. Based on our results we argue that the existence of a flattened lower tail depends on the image resolution and that conclusions about the effect of geomorphic constraints may need further investigation.

The flattened lower tail is well pronounced for SAM and PBP where water bodies were mapped at 0.14 m and 2 m. At BAR where water bodies were mapped at a resolution of 4 m, the flattened lower tail is not as well pronounced, indicating missing water bodies. In polygonal tundra at SAM, ponds have a mean area of about 10 m². Although ice-wedge polygonal tundra is a common feature on the Alaska coastal plain (Brown, 1967), polygonal ponds as small as at SAM could not be mapped at BAR due to the pixel size of the KOMPSAT imagery with 16m². Thus, the total number of water bodies is likely to be even larger for BAR. An increase in water body area by 10% would mean that over 600,000 water bodies smaller than 16 m² were not mapped. But this number would by far exceed the size distribution of small water bodies at BAR even if we would assume a Pareto-based distribution. Other distributions, like the log-normal distribution, also appear linear in the upper part in a log-log plot. But they estimate water body abundances to be orders of magnitude smaller than abundances predicted from the Pareto distribution (Seekell and Pace, 2011). Finding the right model to calculate the size distribution of water bodies, therefore, relies on the completeness of the water body count. Our findings support the conclusions of Seekell and Pace (2011) that there exists a need for a more complex approach to model water body size distributions that goes beyond the extrapolation via a Pareto distribution. Size distributions could be approximated using a two part scheme, finding separate functions for the upper and lower tail of the distribution. Seekell et al. (2013) propose an extended equation of the power-law relationship within a fractal geometry framework to account for the deviation from linearity in the upper tail of the distribution.

Our study shows the loss of small water bodies when mapping water with Landsat data and in the case of SAM also with the MODIS water mask (MOD44W). It is not surprising that water bodies with surface areas below the image resolution should be omitted in a classification process that does not use a subpixel mapping approach. The overestimation of water surface in MOD44W at PBP and BAR, on the other hand, may therefore seem counterintuitive. This effect is the result of the spatial distribution of water bodies in the landscape. Clus-

ters of small water bodies may dominate the pixel spectrum, which is in turn interpreted as pure water. Many small water bodies are consequently lumped into a single larger water body. This effect has also been pointed out by Lehner and Döll (2004) and is amplified by the classification method. In the case of MOD44W, water pixels were identified if the averaged classification result showed a water content of 50 % or greater (Carroll et al., 2009). The total water surface area may then be similar for both high- and low-resolution mapping, but the water body size distributions differ significantly.

MOD44W is a static product that shows average surface water conditions for the time period from May to September of three years 2000 to 2002. Pixels were classified as water when a pixel was identified as water at least 50 % of the time. This approach smoothens out short-term transitions in water bodies due to flooding or drought. The MOD44W therefore represents average conditions in our study areas. All high-resolution data sets as well as Landsat imagery date from mid-July or later so that water body classifications represent mid-summer conditions and are not affected by tundra flooding due to snow melt. Our water body classifications, however, do represent the water surface state at a specific date and not an average condition of the water surface area. Surface area of wetland ponds at PBP was directly measured in relatively wet summers of 2008 and 2009 and varied $\pm 10\%$ during mid-summer and in between years due to differences in precipitation and evaporation (Abnizova et al., 2012). Similar mid-summer fluctuations were found by Bowling et al. (2003) on the Alaska Arctic coastal plain. An increased water body surface area would decrease the ratio of MOD44W water surface area relative to our high-resolution classification and vice versa. MOD44W does not show any water bodies for SAM. In this case, inter-annual variability of the water surface area is not a likely cause. The diameters of the largest lakes on SAM do not exceed 125 m. MODIS pixels of 250×250 m therefore do not show a subpixel water content larger than 50 %and were not classified as water in MOD44W.

3.6.2   *Albedo as an estimator of subpixel water cover*

The correlation between albedo and SWC is linear only for rather homogeneous landscape types, *i. e.*, polygonal terrain of SAM and BAR, drained vegetated thermokarst basins at BAR, and wet tundra at PBP. Open water is the darkest endmember within a Landsat mixed pixel and therefore strongly determines the albedo. However, other dark land surface endmembers like water with immersed vegetation or wet soil also contribute to a low albedo even if the extent of open water within the mixed pixel is small. Conversely, if land surface endmembers have a rather high albedo, a larger proportion of open water is needed within the pixel to result in a low albedo. This argumentation explains both the variation of the SWC-albedo relationship between sites as well as within a site. Different endmember combinations can render the same albedo depending on which endmembers are present, their exact appearance and extent within a mixed pixel. A higher number of endmembers increases the possible number of endmember combinations for the same albedo, which attenuates the albedo–SWC correlation. The number of land surface endmembers present in a study

area may thus be one reason for the wider range of the SWC-albedo relationship at PBP and BAR than at SAM. SAM only comprises polygonal tundra with a limited range of surface types, whereas the larger study areas at PBP and BAR show a greater variety of surface types.

Furthermore, the same endmember varies within sites, which is most apparent for open water. Local variation of open water albedo can be due to several factors, including water turbidity, reflection from lake and pond bottom (Katsaros et al., 1985), and roughness of the water surface (Scott Pegau and Paulson, 2001). The solar elevation angle (SEA), *i.e.*, the incidence of the direct radiation, however, exerts the strongest influence (Payne, 1972; Nunez et al., 1972). Low SEAs lead to larger albedos (Cogley, 1979; Katsaros et al., 1985; Liang, 2000), which possibly explains the larger open water albedo for PBP. SEA is lowest at PBP with 23.5°, whereas SEA is 37.5° for SAM and 40.3° for BAR. Albedo values larger than 0.07 for open water at PBP and BAR represent Landsat pixels that are situated along the margins of water bodies or rivers and streams. Such border pixels are prone to misclassification due to the overlay error between the high-resolution water masks and the Landsat imagery. Border pixels may consequently have been falsely identified as pure water pixels whereas in fact they represent pure land or mixed pixels. For land pixels, the range of albedo is much greater. Compared with open water, land pixels contain several surface types, which are characterized by different vegetation types, surface wetness, and microtopography. Estimated Landsat albedo of Samoylov land surface ranges from 0.09 to 0.14 whereas pyranometer measurements show 0.14 for wet and 0.2 for dry tundra (Langer et al., 2011b). Differences between albedo estimates from satellite sensors and field measurements are mainly due to two factors. First, the directional reflectance function especially at low SEA influences the directional measurements of satellite sensors much more than the hemispherical measurements of pyranometers (Lucht et al., 2000). Second, satellite sensors provide clear-sky measurements only, whereas continuous pyranometer measurements include cloudy and diffuse illumination conditions.

The albedo–SWC function is also affected by the quality of the underlying water body map. At SAM, the resolution of 0.3 m renders the most accurate SWC per Landsat albedo of all three sites, which is another explanation for the lower variation in the albedo-SWC relationship than at PBP and BAR. Resolutions of 2 m at PBP and 4 m at BAR already represent averages of very fine-scale land cover pattern and cannot account for very small patches of water, *e.g.*, water with immersed vegetation, frost cracks, or water patches within wet tundra. Albedo of land pixels at PBP and BAR, therefore, is probably affected by dark soil and water patches that we could not account for with the available remote sensing imagery.

Seasonal variations in water surfaces are another factor to consider regarding the variation of the SWC-albedo relationship. The SAM high-resolution water body map dates from summer 2008 whereas the Landsat image is from summer 2007. Although field observations confirm the overall consistency of water bodies for these years, shallow waters can be subject to high fluctuations in water levels. We therefore speculate that open water surfaces along banks mapped in 2008 actually appeared as water with emergent vegetation in 2007, which would ex-

plain the elevated SWC between albedo values of 0.06 to 0.08 at SAM that are associated with border pixels along the banks of ponds and lakes. At both PBP and BAR, the high-resolution water body maps are from the same year as the Landsat data but date two weeks earlier. At PBP in August 2009, however, water levels were relatively stable even in ponds with dynamic water levels (Abnizova et al., 2012) so that seasonal differences in water cover can be ruled out. Similarly, no extreme rain event or drying of the surface was observed at BAR in summer 2009 from available precipitation records (NCDC web archive at http://www.ncdc.noaa.gov/crn/, StationID 1007).

3.6.3 *Implementation of an albedo–SWC function*

This paper proposes the use of Landsat surface albedo to estimate SWC. The albedo–SWC function of mixed pixels appeared linear for all sites, which is why similar results can be expected in other Arctic tundra environments. However, our separate analyses of polygonal terrain and a vegetated, drained thaw lake basin at BAR show that albedo–SWC functions are site-specific and should be derived separately for different regions and surface types.

Our approach distinguishes two endmembers only, *i. e.*, land and open water, and is thus a robust method. Accounting for patches of open water that are below the detection threshold of even 1 m resolution imagery and investigating the effect of wet tundra soil on albedo could further improve the model. Given the spread of the SWC-albedo relationship, it could best be used to estimate specific ranges of SWC, *i. e.*, grouping Landsat pixels with SWC of $100\% - 80\%$, $60\% - 40\%$, and so on. The estimated SWC could further be linked to our knowledge of the size distribution of water bodies to estimate the number of water bodies smaller than 10^4 m² in a certain area.

Products like the MOD44W are invaluable for their use in regional climate and ecosystem models due to their extensive coverage. Sub-pixel information allows to assess the uncertainty of such coarse-resolution products and should include not only the surface water fraction but also the water body size distribution. Direct coupling of high-resolution water body maps with 1 km or more resolution data, however, would increase the border pixel problem that we already observed at the Landsat scale (Weiss and Crabtree, 2011). Large-scale active and passive microwave as well as optical and infrared measurements have been successfully used to estimate subpixel water cover compared with Landsat-scale maps of open water (Prigent et al., 2001; Weiss and Crabtree, 2011; Watts et al., 2012). A nested downscaling approach could involve stacking regression functions in a two-step scaling approach from high-resolution to Landsat-based mapping and from Landsat-based mapping to coarser products.

3.7   CONCLUSIONS

This study assessed (i) water body distributions across scales and (ii) the potential of Landsat surface albedo to show the subpixel fraction of open water cover (SWC) in three Arctic tundra wetlands in the Canadian High Arctic, Northern Russia and Alaska. Water bodies were mapped using optical and radar satellite data with spatial resolutions

of 4 m or better, Landsat-5 TM imagery at 30 m and the MODIS water mask (MOD44W) at 250 m spatial resolution.

Water bodies at all three sites were dominated in number by ponds, *i.e.*, water bodies with a surface area smaller than 10^4 m², but dominated in area by a few large lakes. At all sites ponds represented over 95 % of the total water body number. Abundance of ponds, however, did not display linearly on a log-log plot as assumed in previous studies but showed a flattened lower tail instead. Landsat- and MODIS-based water body mapping lead to the truncation of the lower tail. Size distributions could then be mistaken for power-law distributed data, which would largely overestimate the number of small water bodies.

Landsat mixed pixels with a SWC between 95 % and 5 % showed albedo values of 0.07 to 0.12 for polygonal and wet tundra, and 0.04 to 0.07 for a drained, vegetated thermokarst basin. Landsat mixed pixels showed a strong linear relationship between albedo and SWC for these distinct terrain types. The best performance with a standard deviation of 21 % SWC was obtained at the polygonal tundra site in Northern Russia where sub-meter resolution mapping of open water surfaces provided the most accurate SWC and the spectral contrast between open water and tundra was highest. Between-site variation ranged between 10 % and 50 % SWC. Estimation of SWC with Landsat surface albedo proved to be a robust approach in the investigated Arctic tundra wetlands, but its applicability in other Arctic regions requires further investigation.

The quality of both water body distributions as well as SWC estimates relied on the detail of the high-resolution water body map. In this study, best results were obtained with spatial resolutions of 2 m or better. Decreasing resolution not only led to the omission of small water bodies but also resulted in local overestimation of water surface area when clusters of small water bodies were merged into single larger water bodies.

This study presents an example of a remote sensing based multi-scale inventory of water bodies in Arctic tundra wetlands. Its results can be used as a baseline to better represent small water bodies of Arctic wet tundra environments in regional as well as global ecosystem and climate models.

European Space Agency to the ACCOnet Project (International Polar Year AO Project 4133). The Landsat-5 TM data and the MODIS water mask (MOD44W) were obtained through the online Data Pool at the NASA Land Processes Distributed Active Archive Center (LP DAAC), USGS/Earth Resources Observation and Science (EROS) Center, Sioux Falls, South Dakota (https://lpdaac.usgs.gov).

4

ASSESSING THE SPATIAL VARIABILITY OF LAND COVER AND LAND SURFACE TEMPERATURE IN HIGH ARCTIC TUNDRA, BATHURST ISLAND, CANADA

4.1 ABSTRACT

The Arctic land surface is changing due to a rapidly warming Arctic climate. Assessing spatial controls of land surface temperature (LST) are important in order to understand the consequences of a changing Arctic land surface on the surface energy balance and its consequences for the regional and global climate. This study investigated spatial and temporal variations of MODIS land surface temperature in a Canadian High Arctic tundra landscape for land cover types ranging from fully vegetated, moist to wet tundra to sparsely vegetated bare soil and barren areas as well as open water surfaces. Land cover composition of MODIS pixels with a resolution of about 1.3 km was quantified based on the Northern Land Cover Classification (NLCC) with a resolution of 30 m. MODIS LST was compared to *in-situ* radiometer measurements over wet tundra for three summer seasons in 2008, 2009, and 2010. MODIS LST in the study area were in good agreement with *in-situ* radiometer measurements showing a mean difference of 1.8 °C. Subpixel land cover heterogeneities within the MODIS pixels were negligible for LST estimation when the subpixel spatial LST differences were less than 5 °C, and the proportion of one land cover class was larger than 60 %. Mean deviations increased for temperatures below freezing which suggests the existence of a cold bias. LST variability within land cover classes was 1.7 °C. The highest LST spatial differences were found for warm and dry synoptic periods characterized by high net radiation with up to 10 °C between for *bare soil* and *open water* surfaces. LST spatial differences indicated differences in the surface energy balance and could be explained by differences in surface albedo, surface moisture, and resistance to evaporation. Net radiation only partially controlled LST spatial differences. High net radiation values were tightly coupled to the first synoptic period where ground thaw and snow melt divert energy from surface warming. Overall, MODIS LST realistically represented different surface conditions which supports its applicability in satellite-based Arctic land cover and energy flux monitoring schemes.

4.2 INTRODUCTION

The Arctic is warming at a rate twice as fast compared to the global temperature increase (Hinzman et al., 2005; ACIA, 2005; Parry, 2007; AMAP, 2011). Spaceborne radiative measurements have recorded Arctic land surface warming of about 1 °C (Comiso, 2003, 2006). Spaceborne radiative measurements are a powerful tool to access land surface warming over large spatial scales. This is especially invaluable in the vast and remote Arctic environments where ground-based obser-

vations of land surface temperature (LST) are sparse and limited to small areas. Spaceborne LST is defined as the radiometric or skin temperature of the Earth's surface which is the canopy temperature for densely vegetated areas and the soil surface temperature in the absence of vegetation (Qin and Karnieli, 1999). In the case of sparsely vegetated ground, LST is the average temperature of the vegetation canopy, vegetation body, and the soil surface under the vegetation. LST is measured by satellite thermal sensors such as Landsat, ASTER, AVHRR or MODIS. Landsat and ASTER provide medium resolutions of 90 m but are limited both in their areal coverage as well as their temporal resolution. The Moderate Resolution Imaging Spectroradiometer (MODIS) with a nominal resolution of 1 km provides global coverage of the polar regions several times per day. MODIS LST have been used to map permafrost extent (Hachem et al., 2009) and to drive soil thermal models for monitoring and projecting the thermal state of permafrost (Langer et al., 2013). Other applications in the Arctic include disturbance mapping (Coops et al., 2009) and the estimation of CO_2 fluxes (Schubert et al., 2010). Performance assessments of MODIS LST have been conducted over selected homogeneous terrain such as lakes, rice crops, silt playas and densely vegetated areas (Hachem et al., 2012). Evaluation of MODIS LST with ground-based radiometer measurements in Arctic regions are limited to two Arctic sites, one on Svalbard in Norway (Westermann et al., 2011) and the other in the Lena Delta in Northern Siberia (Langer et al., 2010). In lack of *in-situ* radiometer measurements, Hachem et al. (2009), Hall et al. (2008) and Hall et al. (2004) used near-surface air temperature to validate MODIS LST but agree that ground-based LST provide a more accurate estimation of MODIS LST uncertainty.

LST forms as a result of the surface energy balance, *i.e.*, the partitioning of the available net radiation into the sensible and latent heat flux and the ground heat flux (Dickinson, 1983). The exchange of turbulent fluxes between the land surface and the atmosphere as well as the heat flux into the ground is controlled by land surface properties such as albedo, emissivity, or surface roughness. Spatial variations in LST can therefore be attributed to differences in land cover. MODIS LST represent spatially aggregated LST over heterogeneous land surfaces. Interpretation of LST spatial variability therefore needs to consider the MODIS subpixel-scale land cover composition. Sustained spatial differences in LST have been found between open water and tundra surfaces in a polygonal tundra landscape in Siberia (Langer et al., 2010) and between wet and dry areas in a sparsely vegetated tundra environment on Svalbard (Westermann et al., 2011). In both studies, LST measurements were obtained from a thermal imaging system mounted on a 10 m mast. Thermal cameras provide high resolutions but are limited in extent to about 100 m² and comparison with MODIS LST were therefore limited to one MODIS pixel only. Few studies have assessed regional LST spatial variation over a wider range of land cover types. LST spatial variations have been investigated in relation to vegetation indices (Goïta et al., 1997; Traore et al., 1997). Vegetation indices, however, were derived at the same resolution as LST so that subpixel heterogeneity could not be accounted for. LST may change with a changing land surface. Changes of the Arctic land surface changes due to a warming climate are, for example, the lengthening of the snow-free

season or the shrub expansion. Other land cover changes include wetting (Jorgenson et al., 2001; Smith et al., 2005; Jorgenson et al., 2006; Watts et al., 2012) and drying of the surface (Yoshikawa and Hinzman, 2003; Smith et al., 2005; Riordan et al., 2006; Carroll et al., 2011) due to the degradation of permafrost. Assessing spatial controls of LST is important in order to understand the consequences of a changing Arctic land surface on the surface energy balance and its consequences for the regional and global climate. The quality of LST monitoring and satellite-based flux monitoring relies on the reliability of spaceborne LST over a wide range of Arctic land surface types.

This study investigates the relationships between land cover and LST for a tundra landscape in the Eastern Canadian High Arctic. Land cover in the study area ranges from barren and sparsely vegetated surfaces to fully vegetated moss/grass tundra. Objectives of the study were to (i) compare MODIS LST to *in-situ* radiometer measurements, and (ii) examine MODIS LST spatial and temporal variations.

4.3 STUDY AREA

Bathurst Island ($98°\,30'$W, $75°\,40'$N) is located in the central zone of the Canadian Arctic Archipelago in Nunavut, Canada (Fig. 22a). Bathurst Island shows a typical polar desert climate with long, cold winters and short, cool, moist summers (Young and Labine, 2010). The climate does not significantly differ from the climate at Resolute Bay on Cornwallis Island which lies about 90 km to the southeast where long-term climate records are available since 1948. Mean January air temperature is $-32.2\,\circ$C and mean July air temperature is $4.3\,°$C (Environment Canada, 2013). Mean annual precipitation is about 155 mm. Neither Resolute Bay nor Bathurst Island show a significant trend in air temperatures or precipitation (Young and Labine, 2010), although Zhang et al. (2000) and Prowse et al. (2009) report a warming trend of $1.3\,°$C and an increase in precipitation of 25 % from 1948 to 2005 for the Eastern Canadian Arctic. Climate projections for the 2050s predict a double increase in both air temperature and precipitation over the entire region of Northern Canada (Prowse et al., 2009).

Plant growth is limited to the short snow-free season which typically lasts about 10 weeks from mid-June to the end of August. Local topography determines drainage characteristics and thus local water supply. Soil conditions and plant communities reflect the topographic moisture gradient. Uplands and plateaus are comparatively dry and plant communities consist of scattered herbaceous perennials with varying amounts of lichens with a low total plant cover (Sheard and Geale, 1983). In low-lying areas, the underlying permafrost impedes drainages which results in poorly drained, highly saturated soils (Edlund and Alt, 1989). Low-lying wetland areas support unusually productive habitats in an otherwise dry and barren environment with a plant cover of 65 % or larger characterized by different types of moss, grass meadows. The Polar Bear Pass (PBP) wetland area on central Bathurst Island is a designated wildlife area and is classified as a Ramsar wetland site of international importance. It forms the largest contiguous wetland area on the island with a surface area of about $94 * 10^6$ km² (Fig. 22c). The PBP wetland area is bordered by hills reaching about 240 m above sea level (a.s.l.) and runoff from these hillslopes

is effective in moving both water and matter into the adjoining wetland zone (Woo and Young, 2006). Within the wetland zone, moss, grass, sedge meadows alternate with sparsely vegetated dry ridges and many small ponds and lakes creating a patchy land cover pattern.
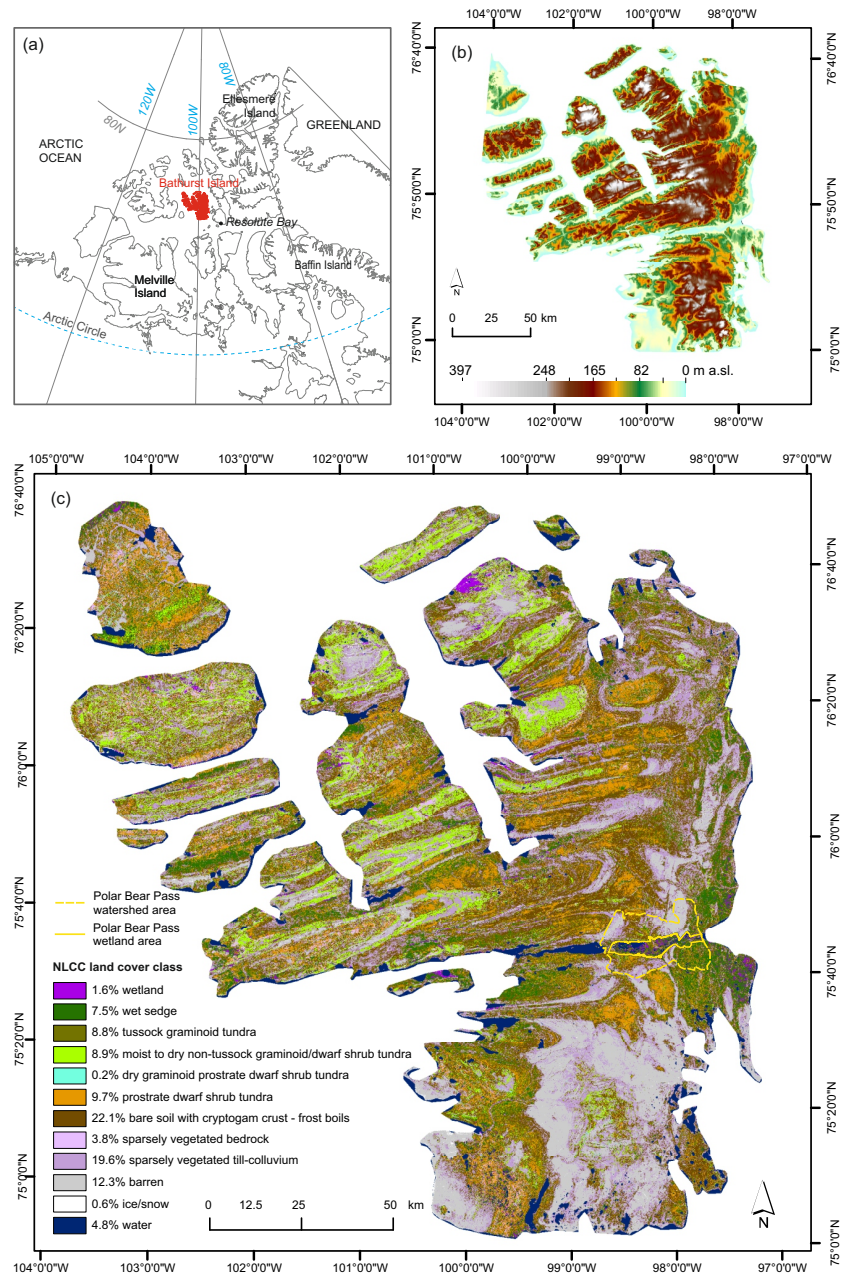
Figure 22: (a) Location of Bathurst Island in the Canadian Arctic Archipelago, (b) topography (Geomatics Canada, 2006), and (c) land cover map of Bathurst Island according to the Northern Land Cover Classification (NLCC).

This study is divided into three parts. First, *in-situ* radiometer measurements are compared to MODIS LST. Secondly, consistency of land cover-LST relationships are evaluated by comparing LST variations within land cover types. Finally, LST spatial and temporal variations are assessed for different land cover types within the PBP watershed.

4.4.1 *Measuring in-situ land surface temperature*

In-situ LST was measured with a Precision Infrared Temperature Sensor (IRTS-P, Campbell Scientific, Inc.) over a patch of wet sedge tundra dominated by moss and grass (Fig. 23). The sensor was mounted 0.83 m above the canopy measuring an area of about 0.28 m in diameter. IRTS-P has an accuracy of $\pm 0.3\,°C$ in the range of 10 to 55 °C. LST was measured from July 2008 to July 2010.

An automatic weather station was set up a few meters next to the radiometer station. Net radiation and incoming short-wave radiation were measured with an NR lite (Kipp & Zonen) with an accuracy of $0.01\,\mathrm{MJm^{-2}}$. Air temperature was measured with a temperature probe CS215 (Campbell Scientific, Inc.) with an accuracy of $\pm 0.2\,°C$. The daily sum of precipitation was recorded with a tipping bucket rain-gauge (Campbell Scientific, Inc.) with an accuracy of $\pm 0.25\,mm$. Sky condition was classified visually in the morning and in the evening as clear, scattered, broken, overcast, partially obscured or obscured.

4.4.2 *Processing MODIS land surface temperature*

Satellite-based LST were acquired from MODIS Collection-5 Land-Surface Temperature/Emissivity level 3 daily product from both the Terra (MOD11A1) and Aqua (MYD11A1) satellites. LST is derived from measurements in the thermal infrared channel 31 (10.78 to 11.28 µm) and channel 32 (11.77 to 12.27 µm) using the day-night split-window algorithm (Wan and Dozier, 1996). Maximum error ranges between 2 and 3 °C with a standard deviation of 0.009 due to emissivity erros (Wan and Li, 1997). The level 3 MODIS LST products contain day and night LST observations which were averaged to obtain daily temperatures. MODIS level 3 LST data are gridded in the sinusoidal projection. The product has a nominal resolution of about 1 km at nadir. Due to the conformal distortion of the sinusoidal projection in the high latitudes, however, grid cells are approximately 0.930 km in width and 1.8 km in length over the study area.
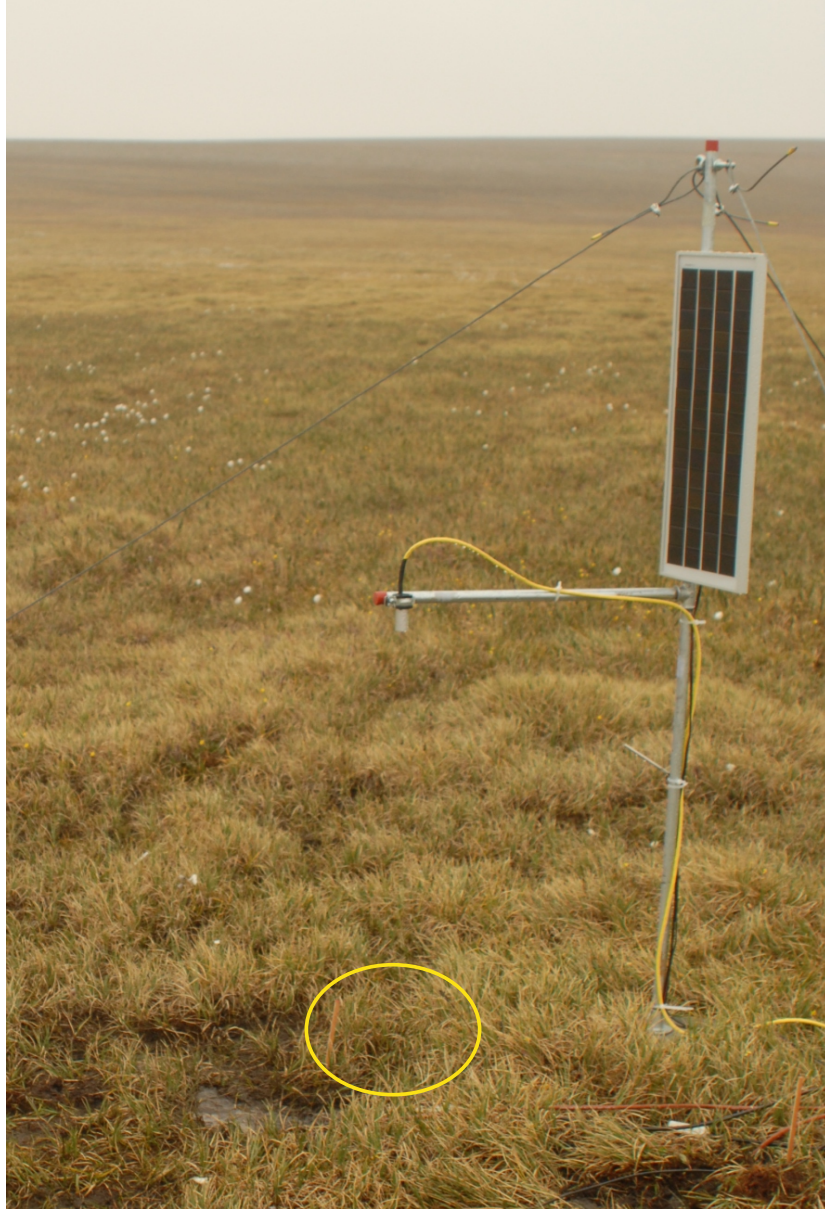
Figure 23: Station with Precision Infrared Temperature Sensor in a zone of wet sedge tundra in the Polar Bear Pass wetland area. The yellow circle indicates the field of view of the radiometer with about 0.28 m in diameter.

4.4.3   *Comparing in-situ LST to MODIS LST*

Evaluation of MODIS LST is typically done by comparing MODIS LST to *in-situ* radiometer or air-borne measurements over homogeneous terrain. In this study, MODIS LST was compared to the *in-situ* radiometer measurements over wet sedge tundra. A MODIS comparison pixel was chosen according to the Northern Land Cover Classification (NLCC) so that MODIS subpixel land cover composition was dominated by the NLCC *wet sedge* class (Fig. 25). Differences between *in-situ* radiometer measurements and MODIS LST were assessed by calculating the mean difference (MD) and the root-mean-square-error (RMSE). MD is an uncertainty measure that takes into account the direction of the difference, whether positive or negative, while RMSE is a measure that is sensitive to outliers and considers the magnitude of the difference without considering the sign (Soliman et al., 2012). MD is simply the average of the differences between MODIS LST and *in-situ* measurements for each time step in the observation period. RMSE is derived by averaging the squared differences between MODIS LST and *in-situ* measurements at each time step and taking the square root of that result.

There exists a large scaling gap between the *in-situ* LST and MODIS LST. Wan (2008) recommends measurements over large homogeneous sites with sizes of at least 5 by 5 km using high-accuracy TIR radiometer measurements at multiple points. These requirements are difficult to fulfill at Arctic sites where logistical constraints limit the selection and number of field stations. The usefulness of the *in-situ* LST measurements for MODIS evaluation in this study can be assessed by looking at the maximum LST spatial variability and the subpixel-scale heterogeneity of MODIS pixels. MODIS LST represents a surface temperature derived from the aggregated radiance over the pixel area. Comparing *in-situ* measurements with MODIS LST implicitly assumes that temperature distribution and emissivity within the measurements areas are similar. Two problems arise with this assumption. First, even within the small measurement area of the *in-situ* radiometer, the surface is not truly uniform. McCabe et al. (2008) illustrates that even homogeneous surfaces show fine-scale differences in surface materials, surface geometry, shadows and microshadows, which cause emissivity and temperature variations. In our case, the field of view (FOV) of the *in-situ* radiometer consists of moss and grass, and microtopography exists due to hummocks. Field mapping and aerial photos show that this micropattern repeats itself over larger areas (Chapter 1, Fig. 1d). We therefore assume that the surface's spectral reponse is homogeneous within the NLCC class *wet sedge*. The second problem it is difficult to find suitable comparison pixels in the PBP wetland area due to the large pixel size of MODIS. MODIS pixels featured a subpixel ratio of 71 % *wet sedge* at most. Other land cover types present in the the chosen MODIS comparison pixel were *tussock graminoid tundra* (8 %), *prostrate dwarf shrub* (7 %), *wetland* (6 %), as well as *bare soil* and *water* surfaces (3 % each). This subpixel heterogeneity introduces uncertainty in the comparison between the MODIS LST and the *in-situ* measurements through differences in the emissivity and temperature of the diverse subpixel land cover fractions.

This uncertainty is assessed by studying the case of a binary mixed pixel composed of *wet sedge* and dry *bare soil*. Remotely sensed LST is retrieved from the outgoing long-wave radiation emitted by the ground surface within the measurement area of the thermal sensor. According to the Stefan-Boltzman Law, emittance from a black body is $\epsilon\sigma T^4$. Natural surfaces, however, do not behave as a black body. The ratio between the radiation emitted by an object and that by a black body at the same temperature is defined as the object's emissivity ϵ. Reported emissivities range from 0.963 to 0.975 for tundra surfaces dominated by moss and grass (Rees, 1993; Langer et al., 2010) and from 0.962 to 0.977 for bare soil (Rees, 1993; Snyder et al., 1998). To address the maximum possible uncertainty, we assumed emissivity values of 0.963 for *wet sedge* and 0.977 for *bare soil*. Radiances were calculated separately for each land cover type within the MODIS pixel according to Kirchhoff's law

$$L_{out,i} = \epsilon\sigma_{sb}T_{surf}^4 + (1 - \epsilon_i)L_{in} \, , \tag{13}$$

where $L_{out,i}$ is the outgoing long-wave radiation of land cover type i (Wm^{-2}), σ is the Stefan-Boltzman constant $(5.67 * 10^{-8}\,Wm^{-2}K^{-4})$, T is the absolute temperature (K), and ϵ_i is the surface emissivity of land cover type i. $L_{out,i}$ were weighted with their respective land cover fraction and subsequently summed to an aggregated radiance for the total area of the MODIS pixel. Inverting equation 13 with the aggregated radiance and a weighted average emissivity yielded the aggregated MODIS surface temperature which was compared to the *in-situ* LST.

4.4.4   *Assessing subpixel land cover composition*

NLCC covers the Canadian North above the treeline with a resolution of 30 m (Olthof et al., 2008). The classification was derived from a Landsat-7 ETM+ mosaic. Most of the imagery including the area over Bathurst Island was acquired during the peak of the growing season period in the months of July and August from July 14, 1999 to August 28, 2002 (Olthof et al., 2005). Landsat data were radiometrically balanced using year-2000 SPOT Vegetation data following the procedure in Olthof et al. (2005). A fuzzy K-means algorithm and a pseudo-colour table representing cluster means in the near-infrared, shortwave-infrared and red spectrum displayed as Red, Green and Blue (RGB) were applied to the mosaic to produce 200 spectral clusters (Olthof et al., 2008). Lookup tables were generated from existing land cover products as well as limited field data and reference data found in the literature to merge spectral clusters to 15 classes. In the eastern Canadian High Arctic, validation was performed in an area surrounding Iqaluit, Nunavut, showing an overall accuracy of about 85 % for 46 points (Olthof et al., 2008). Ponds, *i. e.*, water bodies with a surface area smaller than $10^4\,m^2$, are not resolved by the NLCC but are characteristic for wetland areas. NLCC was enhanced with a high-resolution water body classification for the PBP wetland area where ponds make up 60 % of the total water body number and 22 % of the total water surface area (Muster et al., 2013). Land cover changes since 2000 are expected to be small with the exception of the *wetland* class. The *wetland* class is defined as wet tundra that is flooded part or all

of the year with vegetation emerging from the water surface (Fig. 24a). This condition highly depends on the seasonal water balance including snow melt, runoff and precipitation events.

(a) wetland

(b) wet sedge

(c) moist to dry non-tussock tundra

(d) prostrate dwarf shrub tundra

(e) barren rock

(f) bare soil with cryptogam crust - frost boils

Figure 24: Photos of different land cover types according to the Northern Land Cover Classification in the Polar Bear Pass watershed.

MODIS LST was compared for five representative NLCC land cover types: *barren*, *bare soil*, *open water* (lake), *wet sedge*, and a mixed type comprised of equal parts of the classes *wet sedge*, *wetland* and open *water* (ponds) (Fig. 24). Land cover types were selected to represent the full range of land surface properties from wet to dry and fully vegetated to sparsely vegetated or barren areas. NLCC was intersected with the sinusoidal grid of MODIS in ArcGIS 10.1 (Esri) which rendered the subpixel land cover composition for each MODIS pixel in the study area. Geolocation error is 50 m or better for the NLCC (Olthof et al., 2008) and 50 m at nadir for the MODIS data (Wolfe et al., 2002).

MODIS LST spatial variation was assessed both between land cover classes as well as within land cover classes. Four to five pixels were selected for each land cover type to assess LST variability within a land cover class. The search area for suitable pixels was restricted within an
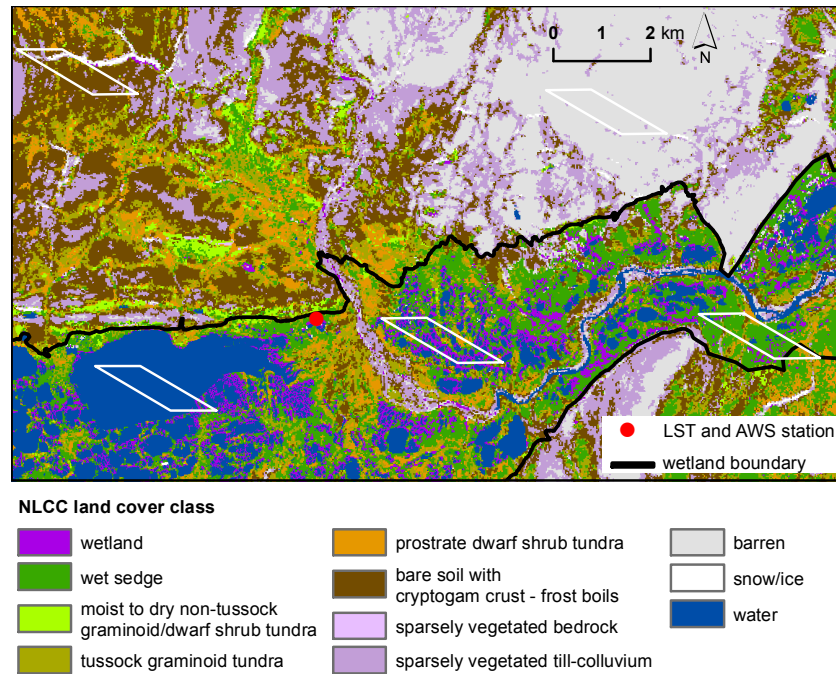
Figure 25: Northern Land Cover Classification of the central Polar Bear Pass wetland area with surrounding uplands. White boxes mark typical MODIS pixels for each of the five selected land cover types.

area $\pm 0.5°$ north and south of Polar Bear Pass to rule out potential LST differences due to a climatic north-south gradient. MODIS pixels composed only of barren ground could be easily identified due to the existence of large contiguous barren areas. No completely homogeneous MODIS pixels could be found for the classes *bare soil*, *wet segde*, and *open water*. Instead, chosen MODIS pixels featured a minimum sub-pixel ratio of 90 % for *bare soil*, of 70 % for *wet sedge*, and 80 % for *open water* (Fig. 25). Evident MODIS LST outliers, *i.e.*, with offsets of 15 °C or more to other MODIS LST measurements, were removed. The variability of LST within each land cover type was assessed by calculating the average standard deviation over the total observation period in 2010 since MODIS LST quality appeared best during this time. LST spatial variation between land cover types and LST temporal patterns were assessed in 2010 for MODIS pixels within the PBP watershed.

Table 9: Selected land cover types of the Northern Land Cover Classification (NLCC), definition and percent plant cover. Albedo mean and standard deviation were calculated for the selected MODIS pixel within the Polar Bear Pass watershed for the snow and lake ice free period from July 12 to August 29, 2010.

NLCC CLASS	NLCC DEFINITION	PLANT COVER [%]	ALBEDO
barren	sparse vegetation on nonacidic and calcareous parent material	< 2	0.23 ± 0.02
bare soil	bare soil with cryptogam crust - frost boils; unconsolidated barren surfaces having experienced significant cryoturbation with $2 - 10\%$ vegetation cover consisting of graminoids and cryptogam plants	$2 - 10$	0.16 ± 0.01
wet sedge	graminoids and bryoids; wet sedge including cottongrass that is saturated for a significant part of the growing season, also includes moss and may include $< 10\%$ dwarf shrubs $< 40\,cm$ tall	> 90	0.17 ± 0.02
wetland	vegetated areas where the water table intersects the land surface all or part of the year	NA	0.13 ± 0.01
open water (lake)	areas covered by liquid standing water	0	0.04 ± 0.00

4.5.1 *Spatial variability of land cover*

Three main topographic units can be distinguished on the Island: low-land, uplands and plateaus (Fig. 22b). The NLCC identifies 12 land cover classes on Bathurst Island (Fig. 22). Upland areas are characterized by *barren* surfaces, *bare soil* surfaces and *prostrate dwarf shrub tundra* (Fig. 24d, e, f) which together account for 44 % of the island's surface area. Nine percent of the island are classified as *graminoid tundra* which characterizes the transition zones between plateaus and low-lands. Lowlands are dominated by wet land surfaces, *i.e.*, *wet sedge* and *wetland*. Wetland areas account for 9 % of the Island's surface area. Most of the water bodies are also located within those areas with a surface cover of 5 %. Subpixel land cover proportions larger than 50 % were found for less than one percent of all MODIS pixels over Bathurst Island. Barren and sparsely vegetated areas represent the largest contiguous land surface types on the island (Fig. 22c).

4.5.2 *Comparing in-situ LST to MODIS LST*

The effect of subpixel land cover composition on the MODIS LST was evaluated for a binary mixed pixel composed of varying proportions of *wet sedge* tundra and dry *bare soil* with varying LST differences. The worst case scenario includes a subpixel composition of 50 % *wet sedge* and 50 % *bare soil* with an LST difference of 10 °C. This worst case scenario results in an offset of 5.1 °C between the aggregated MODIS temperature and the *in-situ* radiometer measurements over *wet sedge* (Fig. 26). The offset decreases with an increasing subpixel ratio of *wet sedge* and a decreasing LST difference. The maximum offset for the chosen comparison MODIS pixel with a subpixel ratio of 70 % *wet sedge* could be 3.1 °C. In the following, deviations between *in-situ* and MODIS measurements larger than 5 °C were consequently not attributed to subpixel heterogeneity but interpreted as MODIS outliers instead.

In total, MODIS LST were compared to *in-situ* LST on 195 days from June 1 to September 30 for the years 2008, 2009, and 2010. Total MD between surface and MODIS LST was 1.8 °C and total RMSE was 4.0 °C (Table 10). A total of 27 outliers were counted for all observation periods. Outliers were generally colder than *in-situ* measurements. The highest number of outliers (14) were counted during the observation period in 2008, which represented 25 % of the available observation pairs. Outliers in 2008 also showed the largest deviation between *in-situ* LST and MODIS LST with a MD of 3.7 °C and a RMSE of 5.1 °C (Table 10). Outliers made up 16 % of the observations pairs in 2009, and 10 % in 2010. Closest agreement between *in-situ* measurements and MODIS LST was found for 2010, when MD was 0.3 °C and RMSE was 2.17 °C. An increase in MODIS LST deviation could be observed towards the end of the validation periods in 2008 and 2009, when LST fell below 0 °C. In 2008, MD is −3.2 °C for the period from July 30 to September 2 and −4.2 °C from September 2 to September 30. The difference in deviation is even larger in 2010 with a MD of −0.6 °C from June 1 to September 4 and a MD of −3.9 °C from September 5 until September 30.
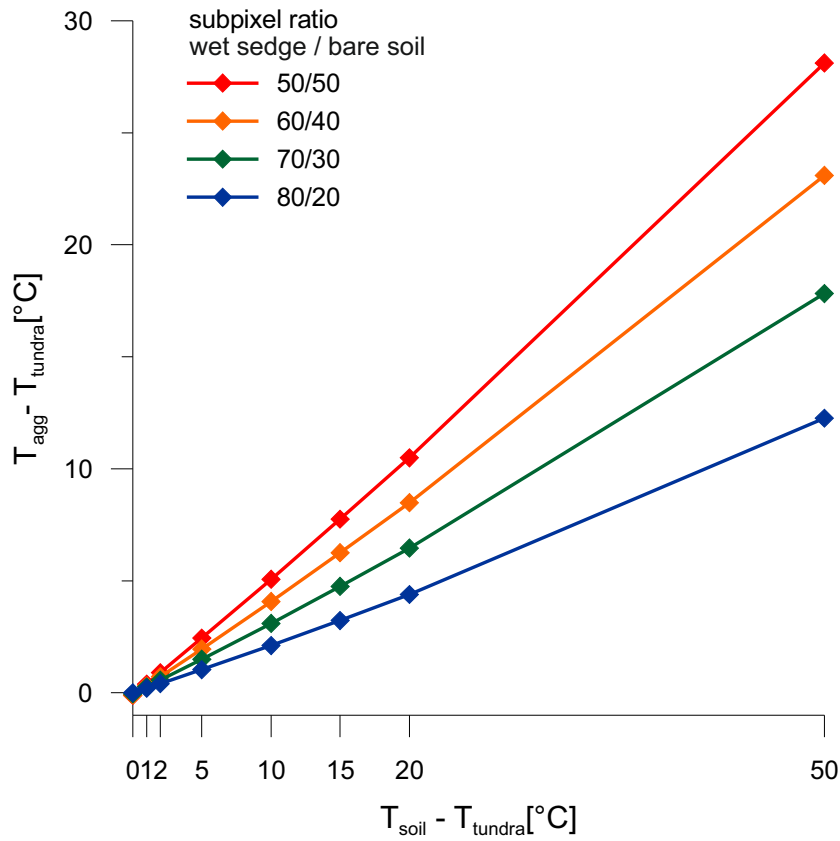
Figure 26: Offset in land surface temperature between the aggregated LST, T_{agg}, and the *in-situ* LST over *wet sedge* tundra, T_{tundra}, for varying subpixel compositions of *wet sedge* and *bare soil*. A constant T_{tundra} of $15\,°C$ was set and T_{soil} was calculated according to the chosen temperature difference $(T_{soil} - T_{tundra})$. Differences in emissivity, ϵ, were set constant with $\epsilon_{tundra} = 0.963$ and $\epsilon_{soil} = 0.977$.

In 2010, *open water* surface started to freeze on September 3, 2010. The *open water* surface exhibited a zero curtain, *i. e.*, surface temperature remained at about 0 °C for four days until September 9, 2010, which is another indicator for the good quality of MODIS LST in 2010. Onset of freezing in 2008 was hard to characterize due to the negative bias of MODIS LST during that period (Fig. 27). In 2008, *in-situ* LST fell below 0 °C on August 17 whereas MODIS LST indicated freezing three to six days earlier. *In-situ* LST also recorded a slight warming up to 3 °C between August 29 and September 2, 2008, which is not shown in MODIS LST.
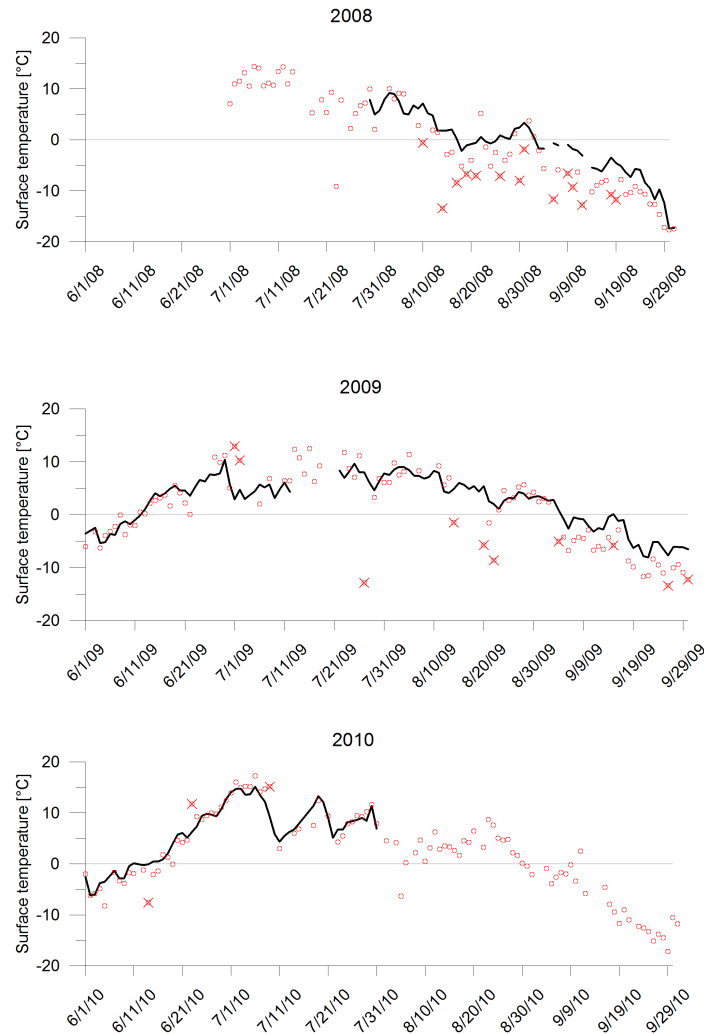
Figure 27: *In-situ* land surface temperature (LST) and MODIS LST measurements for 2008, 2009, and 2010. Black lines denote *in-situ* LST. Open circles represent MODIS LST and crosses indicate MODIS LST outliers with an offset of ±5 °C or more to *in-situ* LST.

Table 10: Statistics of MODIS and *in-situ* land surface temperature comparison.

	2008	2009	2010	TOTAL
observation period	July 30 to September 30	June 01 to September 30	June 01 to July 31	
Number of observation pairs	56	88	51	**195**
Number of outliers	14	10	3	**27**
Mean difference	3.65	1.49	0.28	**1.80**
Root-mean-square error	5.13	4.06	2.17	**4.03**

4.5.3 *Synoptic conditions in 2008, 2009, and 2010*

Weather observations were available from June 1 to August 31 in 2008 and 2009 and from June 1 to August 1 in 2010 (Fig. 28). Two distinct synoptic periods could be identified for all three years. The first period was dominated by little cloud cover, high net radiation, warming air temperatures, and little to no precipitation events. This warming period was well expressed in both 2008 and 2010 lasting from the beginning of June until July 14 in 2008 and July 10 in 2010. In 2008 and 2010, a sharp drop in both net radiation and air temperature marked the beginning of the second period. The second period was characterized by prevailing overcast conditions with frequent precipitation events and low net radiation. In 2009, the first warming period was about two weeks shorter than in 2008 and 2010 lasting until July 1. Air temperatures remained low with a maximum of 9.5 °C compared to 13.5 °C in 2008 and 14.9 °C in 2010. In 2008 (2009), snow melt started on June 5 (6) and lasted until June 12 (11) (Assini and Young, 2012). In 2010, snow melt started about a week later and lasted until June 17 (Young et al., 2013).
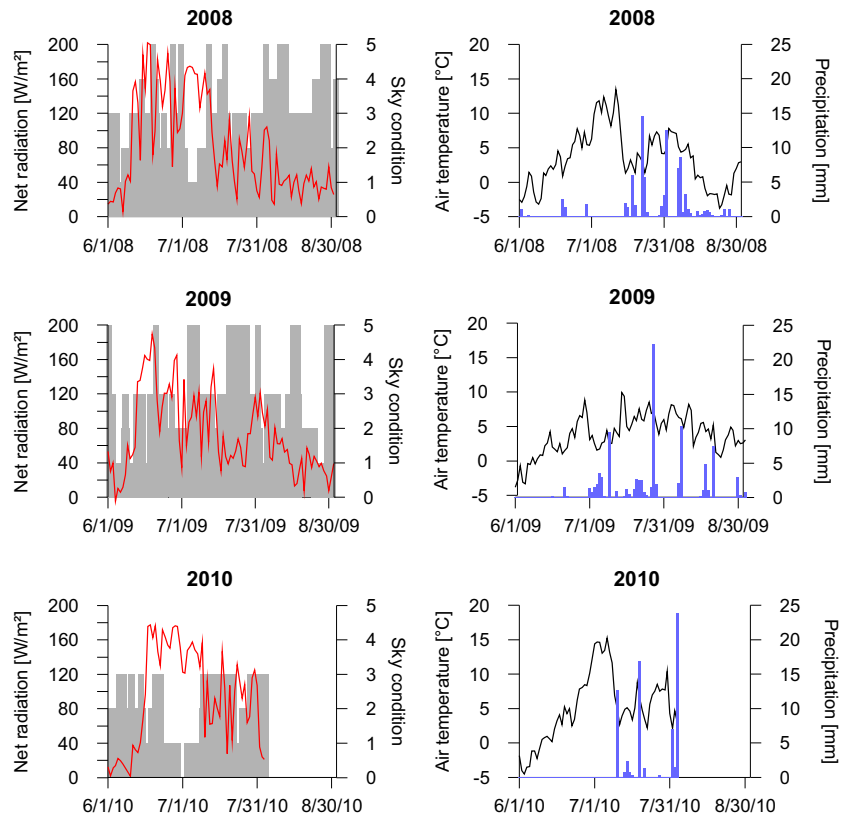
Figure 28: Synoptic conditions in 2008, 2009, and 2010. Plots on the left side show net radiation and sky condition. Plots on the right side show air temperature and precipitation. Bar charts on the left-hand side indicate sky condition from clear sky (0), scattered (1), broken (2), overcast (3), partially obscured (4), and obscured (5). No data was available from August 3 to August 31, 2010.

Table 11: Variability of MODIS land surface temperature (LST) per land cover class.

LAND COVER CLASS	NUMBER OF PIXELS	LST STANDARD DEVIATION [°C]
barren	5	1.6
bare soil	5	1.7
wet sedge	5	1.5
mixed wetland	4	1.3
lake	4	1.7

4.5.4 *Spatial and temporal variability of land surface temperatures*

Overall, MODIS pixels with the same subpixel land cover composition showed a similar range of LST over the course of the 2010 observation period. Average standard deviation was highest for *bare soil* and *open water* surface with 1.7 °C and lowest for the *mixed wetland* type with 1.3 °C (Table 11).

The following assessment of LST temporal and spatial variations between land cover types applies to the MODIS pixels located within the PBP watershed (Fig. 25). Highest LST were found in 2010 during the first synoptic period for *bare soil* surfaces with up to 22 °C (Fig. 30 and 29). *Open water* surfaces reached temperatures of up to 14 °C. LST were coolest in 2009 reaching only a maximum of 14.4 °C for *bare soil* and 10 °C for *open water* surfaces. Significant differences between LST of different land cover types could be observed for all years during the first warm synoptic period (Fig. 30). Variation in LST started to appear after the end of snow melt in mid-June and remained until the end of the period. Mean LST differences were largest between *bare soil* and *open water* surfaces with about 7 °C in 2008 and 9 °C in 2009 and 2010.
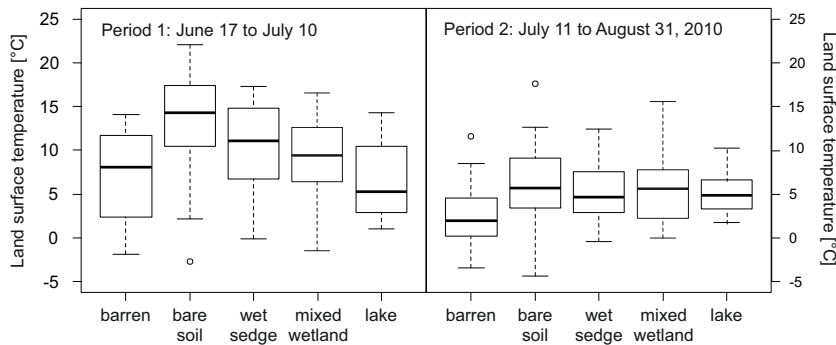
Figure 29: MODIS LST for different land cover types and synoptic periods in 2010. Boxplots show median, upper and lower quartile, minimum and maximum.
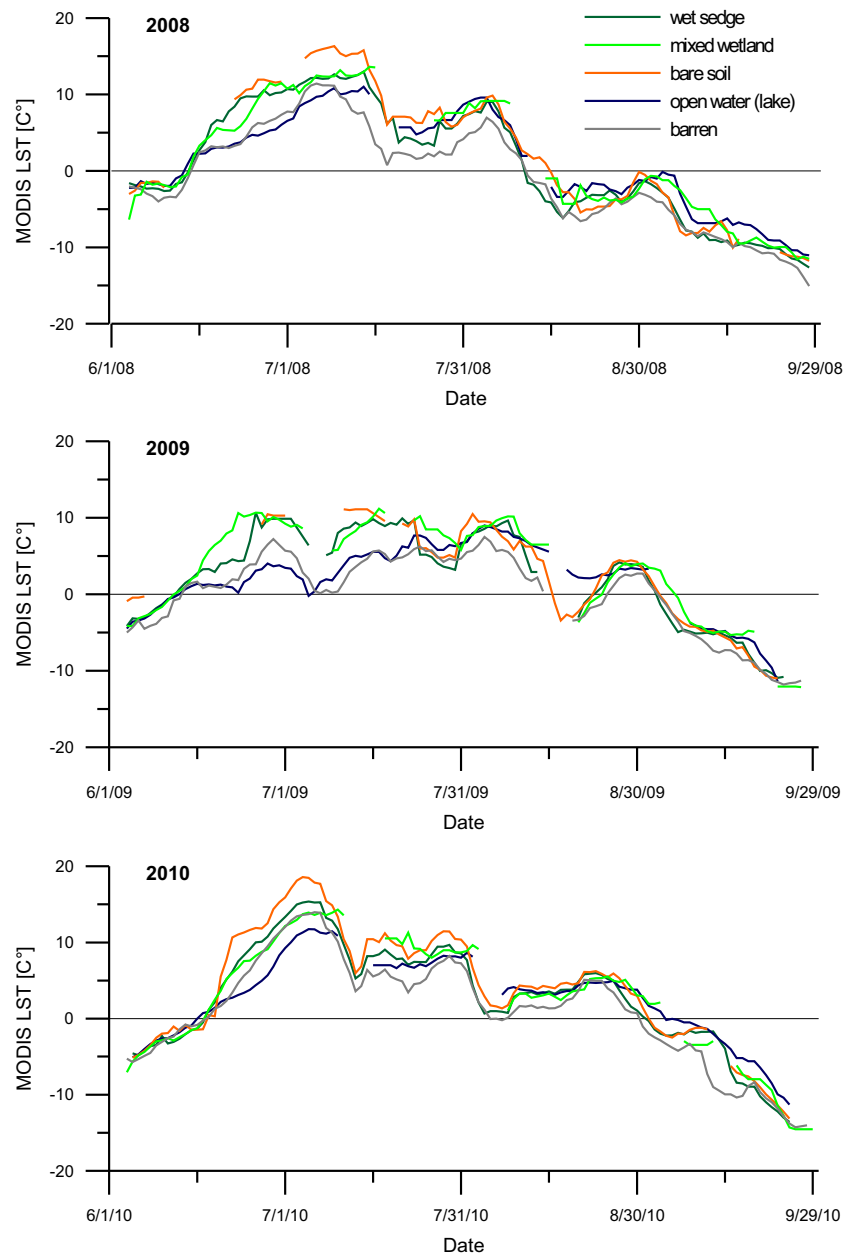
Figure 30: MODIS LST for different land cover types in 2008, 2009, and 2010. A 7-day moving average (MA) was applied to MODIS LST time series. Averages were calculated when a minimum of three observations were present in the time window.

The LST spatial and temporal patterns were similar for all three years. In 2010, for example, *bare soil* surface showed the highest LST with a mean temperature of 13.4 °C followed by *wet sedge* (10.2 °C), *mixed wetland* (9.3 °C), and *barren* surfaces (8.1 °C) (Fig. 29). *Open water* surfaces were coolest with a mean of 5.3 °C. During the cool period in 2010 mean differences between *bare soil*, *wet sedge*, *mixed wetland* and *open water* surfaces diminished. Mean temperature of *bare soil* surfaces were only about 1 °C warmer than the other surface types with the exception of the *barren* surfaces, which were 3.5 °C cooler than *bare soil* surfaces.

The dependence of temperature differences on the net radiation was evaluated for *bare soil*, *wet sedge*, *open water* and *barren* surfaces (Fig. 31). For high positive values of net radiation, *bare soil* surfaces were about 2 °C warmer than the air temperature, T_{air}, whereas *barren* and *open water* surfaces were 1 to 2 °C colder. LST separation between land cover classes was strongest for *bare soil* and *open water* surfaces for the net radiation class centered at 140 Wm^{-2}. For low net radiation values between 0 and 40 Wm^{-2}, spatial differences vanished and all surfaces were about 1 to 2 °C cooler than T_{air}. Both *open water* and *wet sedge* surfaces showed a drop in deviation from T_{air} for high net radiation. Lake surfaces were still frozen until mid-July which explains the significantly cooler lake surface temperature.
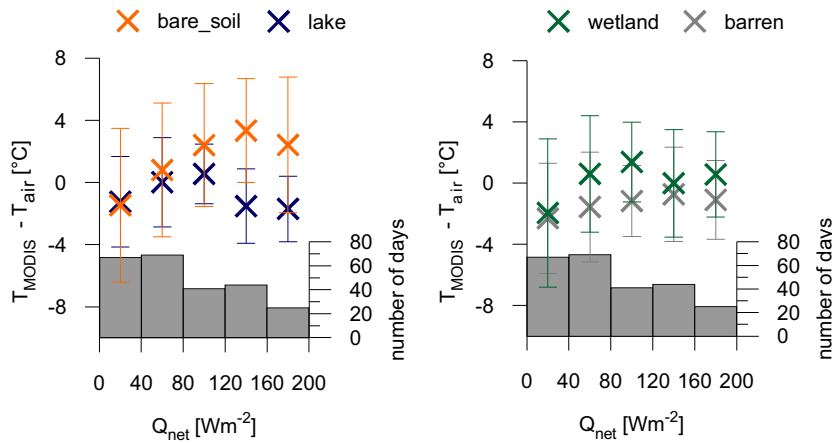
Figure 31: Mean difference between daily averages of air temperature, T_{air} and surface temperature, T_{MODIS}, $(T_{air} - T_{MODIS})$ for *bare soil* (orange), *open water* (blue), *wet sedge* (green), and *barren* (grey) surfaces vs. net radiation in classes of 40 Wm^{-2}. Classes were built over all observations from 2008, 2009, and 2010. Net radiation was recorded at the automatic weather station in *wet sedge* terrain. The error bars show the standard deviation and thus the spread of the data points within a class of net radiation. The histograms show the distribution of the net radiation in number of days.

4.6   DISCUSSION

4.6.1   *Comparison of in-situ LST to MODIS LST*

In-situ LST over a *wet sedge* surface agreed well with a MODIS pixel dominated by *wet sedge* surfaces. This supports the assumption that the measurement area of the *in-situ* radiometer is representative for the NLCC *wet sedge* class which dominates the MODIS comparison pixel. The total mean difference between *in-situ* LST and MODIS LST of 1.8 °C found in this study agrees with other Arctic studies which show deviations of less than 2 °C for MODIS LST weekly averages (Langer et al., 2010; Westermann et al., 2011). However, Wan (2008) reported an accuracy of about 1 °C over homogeneous surfaces. In the present case, deviations larger than 1 °C are probably introduced due to the subpixel land cover heterogeneity within the MODIS comparison pixel. Maximum spatial variability of LST occurs during snow melt when snow free surfaces start to warm whereas remaining patches of snow show LST around 0 °C (Westermann et al., 2011). Small topographic variations in the otherwise flat wet tundra terrain lead to varying snow depths and thus a patchy snow melt pattern (Assini and Young, 2012). This possibly explains the slightly colder MODIS LST during the snow melt period in the first half of June, 2010. MODIS LST that are warmer than *in-situ* LST can be found at end of June, 2009, and the beginning of July, 2010 when LST are highest and LST spatial differences are largest. *Bare soil* and small ponds probably heat stronger within the MODIS comparison pixel than *wet sedge* surfaces and consequently lead to a positive offset.

Uncertainty in the comparison may also be due to inter-annual variations in surface properties, especially surface wetness. Observation periods were characterized by different meteorological conditions including 2009 with a rather wet and cold summer and 2010 with warm and dry conditions. Inter-annual differences in snow water equivalent (SWE) at the end of winter, the thawing of the active layer as well as to the balance between precipitation and evapotranspiration during summer cause annual differences in surface wetness (Woo, 2012). The NLCC, however, is a static product that dates from the years 1999 to 2002, and does not account for different surface wetness conditions in the MODIS comparison pixel.

Overall, MODIS LST deviations were generally colder than *in-situ* measurements and largest during periods dominated by overcast or obscured sky conditions. This pattern suggests a contamination of MODIS LST by clouds or fog, when the MODIS cloud-mask fails to detect all affected pixels especially near cloud edges and with sub-pixel clouds (Langer et al., 2010; Westermann et al., 2011, 2012). In 2009, MODIS LST showed a continuously negative bias after the onset of freezing. This indicates the beginning of a systematic negative bias similar to what has been observed by Westermann et al. (2012) on Svalbard. Warm surface temperatures in winter are typically associated with overcast conditions whereas clear-sky conditions are typically associated with cold surface temperatures. Due to the inherent association with clear-sky conditions, MODIS LST overrepresents cold surface temperatures leading to a cold bias in temporal averages du-

ring winter. An extended validation in the winter months is needed to confirm this bias over the study area.

4.6.2 *Spatial and temporal variation in land surface temperature*

LST variability within the same land cover class showed a standard deviation of less than 2 °C during 2010. Chosen MODIS pixels did not feature a 100 % homogeneous land cover. *E. g.*, bare soil pixels featured a minimum subpixel ratio of 90 % of *bare soil*. The remaining 10 % were composed of varying land cover which probably caused LST variations within the same class. At large, however, the agreement of MODIS LST of the same land cover type is good. This supports the consistency of the NLCC across the study area, *i. e.*, the fine-scale land cover composition within a 30 m² NLCC pixel is consistent within the same class.

During warm and dry periods, *bare soil* surfaces in the study area heat up the most with the average daily LST being about 3 to 8 °C warmer than *wet sedge* surfaces. This difference could be expected due to large difference in available surface moisture. After snow melt, the bare soil surface dries out, and no moisture input is provided through precipitation. The surface resistance increases limiting the latent heat flux so that more energy is available for the sensible heat flux and thus for warming the surface (Seneviratne et al., 2010). Over both *open water* and *mixed wetland* surfaces, however, moisture supply at the surface is unlimited and the increased latent heat flux has a cooling effect on the surface. Over *wet sedge* surfaces, the soil underneath the surface cover of mosses and grasse remains saturated throughout the thawed season. *Wet sedge* surfaces, however, do not show the same degree of cooling as mixed wetland surfaces. This is probably due to a limited latent heat flux from these sites. Evapotranspiration measurements over moss-dominated wetland sites in an Arctic coastal wetland near Barrow, Alaska, showed that an increased bulk surface resistance suppressed the evapotranspiration during large atmospheric demands even if soils were wet (Liljedahl et al., 2011). Transpiration from vascular plants is limited due to the relatively low cover of grasses. Vegetation cover in *wet sedge* surfaces is dominated by mosses. Although the underlying soil remains saturated, the moss-dominated vegetation cover dries out during warm and dry periods which reduces latent heat fluxes (Oechel and Van Cleve, 1986; Muster et al., 2012). Although *barren* surfaces equally dry out during the warm period, they do not heat up as much as *bare soil* but remain about 5 °C cooler. This is likely due to the difference in albedo. *Barren* surfaces exhibit an albedo that is about 7 % higher than the albedo of *bare soil* surfaces, so that more of the incoming shortwave radiation is reflected back into the atmosphere and less net radiation is available for the sensible and latent heat fluxes.

Langer et al. (2010) and Westermann et al. (2011) observed the net radiation to be a controlling factor for LST differences between wet and dry areas of the same land cover type, *i. e.*, tundra and sparsely vegetated barren areas, respectively. In this study net radiation only partly explains the magnitude of LST spatial differences. Surface temperature deviations from the air temperature were much larger than in the studies of Langer et al. (2010) and Westermann et al. (2011) indicating other controlling factors than net radiation. Highest positive

deviations from air temperature are not associated with the highest net radiation values for *bare soil*, *lake*, and *wet sedge* surface. Net radiation higher than 120 Wm⁻² occurs exclusively during the warm synoptic period from the beginning of June until about mid-July. This period comprises the beginning of thaw so that much of the net radiation is used for snow melt and and ground thaw and less for surface warming. Over the course of the period, the thaw front of the active layer is still close to the surface and provides additional cooling (Westermann et al., 2011). *Bare soil* surfaces in the uplands melt out a couple of days earlier than *wet sedge* surfaces in the lowlands so that *bare soil* surfaces start to warm earlier.

Medium-resolution LST measurements inferred from Landsat or ASTER in combination with detailed field-based land cover mapping would improve the understanding of LST variability within areas of MODIS LST. Several Landsat scenes are available throughout the observation period. To retrieve Landsat LST, however, an atmospheric correction of the Landsat thermal band is necessary. Up to date, readily available software do not include standardized models of the Arctic atmosphere. Atmospheric correction would therefore require the calibration of existing algorithms with measured atmospheric profiles in the Arctic which was beyond the scope of this study.

4.7 CONCLUSIONS

MODIS land surface temperature (LST) showed similar spatial and temporal variations in Canadian High Arctic tundra over a range of land cover types for the three different years 2008, 2009, and 2010 with varying meteorological conditions. All three years show distinct dual weather pattern with a warm and dry period from the beginning of June to about mid-July and a wet, cool period later on. LST spatial differences indicate differences in the surface energy balance and could be explained by differences in surface albedo, surface moisture, and resistance to evaporation. Net radiation only partially controled LST spatial differences. High net radiation values were tightly coupled to the first synoptic period where ground thaw and snow melt divert energy from surface warming.

MODIS LST in the study area were in good agreement with *in-situ* radiometer measurements showing a mean difference of 1.8 °C. MODIS LST are inherently affected by subpixel heterogeneities in land cover due to the large pixel size of 1.7 km² and the high land cover heterogeneity in the study area. Subpixel land cover heterogeneities within the MODIS pixels were negligible when the subpixel spatial LST differences were less than 5 °C, and the proportion of one land cover class was larger than 60 %.

LST variability within land cover classes of 1.7 °C was similar to the overall MODIS uncertainty. This indicates that the land surface representation via the Northern Land Cover Classification (NLCC) of LST is consistent throughout the study area and has undergone little change since the NLCC production in 1999 to 2002. The assessment of subpixel land cover heterogeneities within the NLCC might further explain MODIS LST variations.

All in all, MODIS LST realistically represented different surface conditions ranging from fully vegetated, moist to wet tundra to sparsely

vegetated bare soil and barren areas as well as open water surfaces which supports its applicability in satellite-based Arctic land cover and energy flux monitoring schemes. However, the possible uncertainty in MODIS LST due to subpixel land cover effects should be considered.

BIBLIOGRAPHY

Abnizova, A., J. Siemens, M. Langer, and J. Boike (2012). Small ponds with major impact: The relevance of ponds and lakes in permafrost landscapes to carbon dioxide emissions. *Global Biogeochemical Cycles 26*(GB2041), 1–9.

Abnizova, A., K. Young, and M. Lafreniere (2012). Pond hydrology and dissolved carbon dynamics at Polar Bear Pass wetland, Bathurst Island, Nunavut. *Ecohydrology*, doi: 10.1002/eco.1323.

ACIA (2005). *Arctic climate impact assessment–scientific report*. Cambridge, UK: Cambridge University Press.

AMAP (2011). Snow, water, ice and permafrost in the Arctic (SWIPA). *Oslo: Arctic Monitoring and Assessment Programme (AMAP)*.

Assini, J. and K. L. Young (2012). Snow cover and snowmelt of an extensive High Arctic wetland: spatial and temporal seasonal patterns. *Hydrological Sciences Journal 57*(4), 738–755.

Avis, C. A., A. J. Weaver, and K. J. Meissner (2011). Reduction in areal extent of high-latitude wetlands in response to permafrost thaw. *Nature Geosciences Letter 4*(7), 444–448.

Banks, S. N., T. Ullmann, J. Duffe, A. Roth, D. J. King, A. M. Demers, A. Hogg, A. Schmitt, R. Baumhauer, and S. Dech (2012). Multifrequency analysis of high resolution quad-pol Radarsat-2 and dual-pol TerraSAR-X data for land cover classification in Arctic Coastal Ecosystems, Mackenzie Delta, beaufort sea. In *Geoscience and Remote Sensing Symposium (IGARSS), 2012 IEEE International*, pp. 3548–3551. IEEE.

Barkman, J. J. (1958). *Phytosociology and ecology of cryptogamic epiphytes, including a taxonomic survey and description of their vegetation units in Europe.* Assen, Netherland: Van Gorcum & Comp. NV.

Bartholomé, E. and A. Belward (2005). GLC2000: a new approach to global land cover mapping from Earth observation data. *International Journal of Remote Sensing 26*(9), 1959–1977.

Blok, D., M. Heijmans, G. Schaepman-Strub, J. Van Ruijven, F. Parmentier, T. Maximov, and F. Berendse (2011). The cooling capacity of mosses: controls on water and energy fluxes in a Siberian tundra site. *Ecosystems 14*(7), 1055–1065.

Boike, J., B. Kattenstroth, K. Abramova, N. Bornemann, A. Chetverova, I. Fedorova, K. Fröb, M. Grigoriev, M. Grüber, L. Kutzbach, et al. (2013). Baseline characteristics of climate, permafrost and land cover from a new permafrost observatory in the Lena River Delta, Siberia (1998-2011). *Biogeosciences 10*(3), 2105–2128.

Boike, J., M. Langer, H. Lantuit, S. Muster, K. Roth, T. Sachs, P. Overduin, S. Westermann, and A. D. McGuire (2012). Permafrost–Physical Aspects, Carbon Cycling, Databases and Uncertainties. In *Recarbonization of the Biosphere*, pp. 159–185. Springer.

Boike, J., C. Wille, and A. Abnizova (2008). Climatology and summer energy and water balance of polygonal tundra in the Lena River Delta, Siberia. *Journal of Geophysical Research 113*(G03025).

Bonan, G., F. Chapin, and S. Thompson (1995). Boreal forest and tundra ecosystems as components of the climate system. *Climatic Change 29*(2), 145–167.

Bowling, L., D. Kane, R. Gieck, L. Hinzman, and D. Lettenmaier (2003). The role of surface storage in a low-gradient Arctic watershed. *Water Resources Research 39*(4), 1087.

Braud, D. and W. Feng (1998). Semi-automated construction of the Louisiana coastline digital land/water boundary using Landsat Thematic Mapper satellite imagery. *Technical Report 97-002 97*(2).

Braun-Blanquet, J. (1932). *Plant Sociology. The study of plant communities*, Volume First edition. New York and London: McGraw-Hill Book Co., Inc.

Brest, C. L. and S. Goward (1987). Deriving surface albedo measurements from narrow band satellite data. *International Journal of Remote Sensing 8*(3), 351–367.

Brown, J. (1967). Tundra soils formed over ice wedges, northern Alaska. *Soil Science Society of America Journal 31*(5), 686–691.

Brown, J., O. J. Ferrians, J. Heginbottom, and E. Melnikov (1997). *Circum-Arctic map of permafrost and ground-ice conditions*. Reston, USA: US Geological Survey Reston.

Brown, J. and P. Johnson (1965). Pedo-ecological investigations, Barrow, Alaska. Technical report, Cold Regions Research and Engeneering Lab, Hanover, USA.

Brown, J., P. Miller, L. Tieszen, and F. Bunnell (1980). *An arctic ecosystem: the coastal tundra at Barrow, Alaska*. Dowden, Hutchinson & Ross, Inc.

Brown, L. and K. Young (2009). Assessment of three mapping techniques to delineate lakes and ponds in a Canadian High Arctic wetland complex. *Arctic 59*(3), 283–293.

Carroll, M., J. Townshend, C. DiMiceli, T. Loboda, and R. Sohlberg (2011). Shrinking lakes of the Arctic: Spatial relationships and trajectory of change. *Geophysical Research Letters 38*(20).

Carroll, M., J. Townshend, C. DiMiceli, P. Noojipady, and R. Sohlberg (2009). A new global raster water mask at 250 m resolution. *International Journal of Digital Earth 2*(4), 291–308.

Chander, G., B. Markham, and D. Helder (2009). Summary of current radiometric calibration coefficients for Landsat MSS, TM, ETM+, and EO-1 ALI sensors. *Remote Sensing of Environment 113*(5), 893–903.

Chapin, F., M. Sturm, and M. e. a. Serreze (2005). Role of land-surface changes in Arctic summer warming. *Science 310*(5748), 657.

Chapin III, F. S., P. A. Matson, and P. M. Vitousek (2012). Landscape Heterogeneity and Ecosystem Dynamics. In *Principles of Terrestrial Ecosystem Ecology*, Volume second edition, pp. 369–397. New York, USA: Springer.

Chapin III, F. S., A. D. McGuire, J. Randerson, R. Pielke, D. Baldocchi, S. E. Hobbie, N. Roulet, W. Eugster, E. Kasischke, and E. B. Rastetter (2000). Arctic and boreal ecosystems of western North America as components of the climate system. *Global Change Biology 6*(S1), 211–223.

Chavez, P. (1988). An improved dark-object subtraction technique for atmospheric scattering correction of multispectral data. *Remote Sensing of Environment 24*(3), 459–479.

Chavez, P. (1996). Image-based atmospheric corrections-revisited and improved. *Photogrammetric Engineering and Remote Sensing 62*(9), 1025–1035.

Cogley, J. (1979). The albedo of water as a function of latitude. *Monthly Weather Review 107*(6), 775–781.

Comiso, J. C. (2003). Warming trends in the Arctic from clear sky satellite observations. *Journal of Climate 16*(21), 3498–3510.

Comiso, J. C. (2006). Arctic warming signals from satellite observations. *Weather 61*(3), 70–76.

Coops, N. C., M. A. Wulder, and D. Iwanicka (2009). Large area monitoring with a MODIS-based Disturbance Index (DI) sensitive to annual and seasonal variations. *Remote Sensing of Environment 113*(6), 1250–1261.

Dickinson, R. (1983). Land surface processes and climate–Surface albedos and energy balance. *Advances in Geophysics 25*, 305–353.

Downing, J., Y. Prairie, J. Cole, C. Duarte, L. Tranvik, R. Striegl, W. McDowell, P. Kortelainen, N. Caraco, J. Melack, et al. (2006). The global abundance and size distribution of lakes, ponds, and impoundments. *Limnology and Oceanography 51*(5), 2388–2397.

Duguay, C. and E. Ledrew (1992). Estimating surface reflectance and albedo from Landsat-5 Thematic Mapper over rugged terrain. *Photogrammetric Engineering and Remote Sensing 58*, 551–558.

Edlund, S. and B. Alt (1989). Regional congruence of vegetation and summer climate patterns in the Queen Elizabeth Islands, Northwest Territories, Canada. *Arctic 42*(1), 3–23.

Eicken, H., T. Grenfell, D. Perovich, J. Richter-Menge, and K. Frey (2004). Hydraulic controls of summer Arctic pack ice albedo. *Journal of Geophysical Research 109*(C08007).

Emmerton, C., L. Lesack, and P. Marsh (2007). Lake abundance, potential water storage, and habitat distribution in the Mackenzie River Delta, western Canadian Arctic. *Water Resources Research 43*(5), W05419.

Environment Canada (2013). Climate data online, Resolute Bay, Nunavut. *http://www.climate.weatheroffice.gc.ca 2013-5-22*.

Eugster, W., W. Rouse, R. Pielke Sr, J. Mcfadden, D. Baldocchi, T. Kittel, F. Chapin III, G. Liston, P. Vidale, E. Vaganov, et al. (2000). Land-atmosphere energy exchange in Arctic tundra and boreal forest: Available data and feedbacks to climate. *Global Change Biology 6*(S1), 84–115.

Euskirchen, E. S. and M. S. Bret-Harte (2009). The Arctic Observatory Network. *FluxLetter 2*(2), 1–3.

Fetterer, F. and N. Untersteiner (1998). Observations of melt ponds on Arctic sea ice. *Journal of Geophysical Research 103*(C11), 24821–24835.

Firbas, F. (1931). *Untersuchungen über den Wasserhaushalt der Hochmoorpflanzen* (German ed.). Leipzig, Germany: Borntraeger.

Foody, G. M. (2002). Status of land cover classification accuracy assessment. *Remote Sensing of Environment 80*(1), 185–201.

Frazier, P., K. Page, et al. (2000). Water body detection and delineation with Landsat TM data. *PE & RS- Photogrammetric Engineering & Remote Sensing 66*(12), 1461–1467.

French, H. (2007). *The periglacial environment* (3rd ed.). West Sussex, England: Wiley.

Frey, K. and L. Smith (2007). How well do we know Northern land cover? Comparison of four global vegetation and wetland products with a new ground-truth database for West Siberia. *Global Biogeochemical Cycles 21*(1), GB1016.

Fritz, T., M. Eineder, M. Lachaise, A. Roth, H. Breit, B. Schättler, and M. Huber (2007). TerraSAR-X Level 1b Product Format Specification. Technical report, TX-GS-DD-3307, Oberpfaffenhofen, Germany.

Garratt, J. (1994). *The atmospheric boundary layer*. Cambridge, UK: Cambridge University Press.

Geomatics Canada (2006). *Canadian Digital Elevation Data, Level 1 (CDED1), version 1.0*. Chatham, Canada: Geomatics, Natural Resources Canada.

Goïta, K., A. Royer, and N. Bussières (1997). Characterization of land surface thermal structure from NOAA-AVHRR data over a northern ecosystem. *Remote sensing of environment 60*(3), 282–298.

Gómez-Chova, L., L. Alonso, L. Guanter, G. Camps-Valls, J. Calpe, and J. Moreno (2008). Correction of systematic spatial noise in pushbroom hyperspectral sensors: Application to CHRIS/PROBA images. *Applied Optics 47*(28), F46–F60.

Goswami, S., J. Gamon, and C. Tweedie (2011). Surface hydrology of an arctic ecosystem: Multiscale analysis of a flooding and draining experiment using spectral reflectance. *Journal of Geophysical Research: Biogeosciences 116*(G4), G00I07.

Grant, R., W. Oechel, and C. Ping (2003). Modelling carbon balances of coastal Arctic tundra under changing climate. *Global Change Biology 9*(1), 16–36.

Grigoriev, M. (1993). *Cryomorphogenesis in the Lena Delta* (Russian ed.). Yakutsk, Russia: Permafrost Institute Press.

Grigoriev, N. (1960). The temperature of permafrost in the Lena delta basin: deposit conditions and properties of the permafrost in Yakutia. *229*, 97–101.

Grosse, G., V. Romanovsky, K. Walter, A. Morgenstern, H. Lantuit, and S. Zimov (2008). Distribution of thermokarst lakes and ponds at three yedoma sites in Siberia. In *Ninth International Conference on Permafrost, Kane, DL & Hinkel, KM (eds), Institute of Northern Engineering, University of Alaska Fairbanks*, pp. 551–556.

Guanter, L., R. Richter, and J. Moreno (2006). Spectral calibration of hyperspectral imagery using atmospheric absorption features. *Applied optics 45*(10), 2360–2370.

Gutowski, W. J., H. Wei, C. J. Voeroesmarty, and B. M. Fekete (2007). Influence of Arctic wetlands on Arctic atmospheric circulation. *Journal of Climate 20*(16), 4243–4254.

Hachem, S., M. Allard, and C. Duguay (2009). Using the MODIS land surface temperature product for mapping permafrost: an application to northern Québec and Labrador, Canada. *Permafrost and Periglacial Processes 20*(4), 407–416.

Hachem, S., C. Duguay, and M. Allard (2012). Comparison of MODIS-derived land surface temperatures with ground surface and air temperature measurements in continuous permafrost terrain. *The Cryosphere 6*, 51–69.

Hall, D. K., J. E. Box, K. A. Casey, S. J. Hook, C. A. Shuman, and K. Steffen (2008). Comparison of satellite-derived and in-situ observations of ice and snow surface temperatures over Greenland. *Remote Sensing of Environment 112*(10), 3739–3749.

Hall, D. K., J. R. Key, K. A. Casey, G. A. Riggs, and D. J. Cavalieri (2004). Sea ice surface temperature product from MODIS. *Geoscience and Remote Sensing, IEEE Transactions on 42*(5), 1076–1087.

Hamilton, S., J. Melack, M. Goodchild, and W. Lewis (1992). *Estimation of the fractal dimension of terrain from lake size distributions*, pp. 145–163. New York, USA: Wiley.

Hansen, M., R. DeFries, J. R. Townshend, and R. Sohlberg (2000). Global land cover classification at 1 km spatial resolution using a classification tree approach. *International Journal of Remote Sensing 21*(6-7), 1331–1364.

Hill, T., T. Quaife, and M. Williams (2011). A data assimilation method for using low-resolution Earth observation data in heterogeneous ecosystems. *Journal of Geophysical Research 116*(D8), D08117.

Hinkel, K., W. Eisner, J. Bockheim, F. Nelson, K. Peterson, and X. Dai (2003). Spatial extent, age, and carbon stocks in drained thaw lake basins on the Barrow Peninsula, Alaska. *Arctic, Antarctic, and Alpine Research 35*(3), 291–300.

Hinkel, K. and F. Nelson (2003). Spatial and temporal patterns of active layer thickness at Circumpolar Active Layer Monitoring (CALM) sites in northern Alaska, 1995–2000. *Journal of Geophysical Research 108*(D2), 8168.

Hinzman, L. D., N. D. Bettez, and W. R. e. a. Bolton (2005). Evidence and implications of recent climate change in Northern Alaska and other Arctic regions. *Climatic Change 72*, 251–298.

Hope, A. (1999). Estimating lake area in an Arctic landscape using linear mixture modelling with AVHRR data. *International Journal of Remote Sensing 20*(4), 829–835.

Hosokawa, T., N. Odani, and H. Tagawa (1964). Causality of the distribution of corticolous species in forests with special reference to the physio-ecological approach. *The Bryologist 67*(4), 396–411.

Idso, S., R. Jackson, R. Reginato, B. Kimball, and F. Nakayama (1975). The dependence of bare soil albedo on soil water content. *Journal of Applied Meteorology 14*(1), 109–113.

Jackson, R., S. Idso, and R. Reginato (1976). Calculation of evaporation rates during the transition from energy-limiting to soil-limiting phases using albedo data. *Water Resources Research 12*(1), 23–26.

Jia, G. J., H. E. Epstein, and D. A. Walker (2003). Greening of arctic Alaska, 1981–2001. *Geophysical Research Letters 30*(20).

Jorgenson, M., C. Racine, J. Walters, and T. Osterkamp (2001). Permafrost degradation and ecological changes associated with a warming climate in central Alaska. *Climatic Change 48*(4), 551–579.

Jorgenson, M. T., Y. L. Shur, and E. R. Pullman (2006). Abrupt increase in permafrost degradation in Arctic Alaska. *Geophysical Research Letters 33*(2).

Kane, D. L. and R. F. Carlson (1973). Hydrology of the central arctic river basins of Alaska. Technical report.

Katsaros, K., L. Mcmurdie, R. Lind, and J. DeVault (1985). Albedo of a water surface, spectral variation, effects of atmospheric transmittance, sun angle and wind speed. *Journal of Geophysical Research 90*(C4), 7313–7321.

Kattsov, V., J. Walsh, W. Chapman, V. Govorkova, T. Pavlova, and X. Zhang (2007). Simulation and projection of Arctic freshwater budget components by the IPCC AR4 global climate models. *Journal of Hydrometeorology 8*(3), 571–589.

Kolasa, J. and C. D. Rollo (1991). Introduction: the heterogeneity of heterogeneity: a glossary. In *Ecological Heterogeneity*, pp. 1–23. Springer.

Kutzbach, L., D. Wagner, and E.-M. Pfeiffer (2004). Effect of microrelief and vegetation on methane emission from wet polygonal tundra, Lena Delta, Northern Siberia. *Biogeochemistry 69*, 341–362.

Langer, M., S. Westermann, and J. Boike (2010). Spatial and temporal variations of summer surface temperatures of wet polygonal tundra in Siberia - implications for MODIS LST based permafrost monitoring. *Remote Sensing of Environment 114*(9), 2059–2069.

Langer, M., S. Westermann, M. Heikenfeld, W. Dorn, and J. Boike (2013). Satellite-based modeling of permafrost temperatures in a tundra lowland landscape. *Remote Sensing of Environment 135*, 12–24.

Langer, M., S. Westermann, S. Muster, K. Piel, and J. Boike (2011a). Permafrost and surface energy balance of a polygonal tundra site in Northern Siberia–Part 2: Winter. *The Cryosphere 5*, 509–524.

Langer, M., S. Westermann, S. Muster, K. Piel, and J. Boike (2011b). The surface energy balance of a polygonal tundra site in Northern Siberia–Part 1: Spring to fall. *The Cryosphere 5*, 151–171.

Laurion, I., W. Vincent, S. MacIntyre, L. Retamal, C. Dupont, P. Francus, and R. Pienitz (2010). Variability in greenhouse gas emissions from permafrost thaw ponds. *Limnology and Oceanography 55*(1), 115–133.

Lehner, B. and P. Döll (2004). Development and validation of a global database of lakes, reservoirs and wetlands. *Journal of Hydrology 296*(1-4), 1–22.

Liang, S. (2000). Narrowband to broadband conversions of land surface albedo I: Algorithms. *Remote Sensing of Environment 76*(2), 213–238.

Liljedahl, A., L. Hinzman, Y. Harazono, D. Zona, C. Tweedie, R. Hollister, R. Engstrom, and W. Oechel (2011). Nonlinear controls on evapotranspiration in Arctic coastal wetlands. *Biogeosciences 8*, 3375–3389.

Lillesand, T., R. Kiefer, and J. Chipman (2004). *Remote sensing and image interpretation* (5 ed.). New York, USA: John Wiley & Sons Ltd.

Lucht, W., A. Hyman, A. Strahler, M. Barnsley, P. Hobson, and J. Muller (2000). A comparison of satellite-derived spectral albedos to ground-based broadband albedo measurements modeled to satellite spatial scale for a semidesert landscape. *Remote Sensing of Environment 74*(1), 85–98.

MacKay, D. (2003). *Information theory, inference, and learning algorithms*. Cambridge, UK: Cambridge University Press.

Masson, V., J.-L. Champeaux, F. Chauvin, C. Meriguet, and R. Lacaze (2003). A global database of land surface parameters at 1-km resolution in meteorological and climate models. *Journal of Climate 16*(9), 1261–1282.

Mauder, M. and T. Foken (2004). *Documentation and instruction manual of the eddy covariance software package TK2*. Bayreuth, Germany: University of Bayreuth.

Mauder, M., T. Foken, R. Clement, J. Elbers, W. Eugster, T. Grünwald, B. Heusinkveld, and O. Kolle (2008). Quality control of CarboEurope flux data? Part 2: Inter-comparison of eddy-covariance software. *Biogeosciences 5*(2), 451–462.

Mauder, M., C. Liebethal, M. Göckede, J. Leps, F. Beyrich, and T. Foken (2006). Processing and quality control of flux data during LITFASS-2003. *Boundary-Layer Meteorology 121*(1), 67–88.

McCabe, M., L. Balick, J. Theiler, A. Gillespie, and A. Mushkin (2008). Linear mixing in thermal infrared temperature retrieval. *International Journal of Remote Sensing 29*(17-18), 5047–5061.

McDonald, C. P., J. A. Rover, E. G. Stets, and R. G. Striegl (2012). The regional abundance and size distribution of lakes and reservoirs in the United States and implications for estimates of global lake extent. *Limnology and Oceanography 57*(2), 597–606.

McFadden, J. P., W. Eugster, and F. S. Chapin Iii (2003). A regional study of the controls on water vapor and CO_2 exchange in Arctic tundra. *Ecology 84*(10), 2762–2776.

McGuire, A., L. Anderson, T. Christensen, S. Dallimore, L. Guo, D. Hayes, M. Heimann, T. Lorenson, R. Macdonald, and N. Roulet (2009). Sensitivity of the carbon cycle in the Arctic to climate change. *Ecological Monographs 79*(4), 523–555.

McGuire, A., F. Chapin, C. Wirth, M. Apps, J. Bhatti, T. Callaghan, T. Christensen, J. Clein, M. Fukuda, T. Maximov, et al. (2007). Responses of high latitude ecosystems to global change: Potential consequences for the climate system. *Terrestrial Ecosystems in a Changing World*, 297–310.

Mendez, J., L. Hinzman, and D. Kane (1998). Evapotranspiration from a wetland complex on the Arctic coastal plain of Alaska. *Nordic hydrology 29*(4), 303–330.

Morgenstern, A., G. Grosse, and L. Schirrmeister (2008). Genetic, morphological, and statistical characterization of lakes in the permafrost-dominated Lena Delta. In *Proceedings of the Ninth International Conference on Permafrost (NICOP), June 29–July 3, 2008, Fairbanks, Alaska, USA*.

Muster, S., B. Heim, A. Abnizova, and J. Boike (2013). Water body distributions across scales: A remote sensing based comparison of three Arctic tundra wetlands. *Remote Sensing 5*(4), 1498–1523.

Muster, S., M. Langer, B. Heim, S. Westermann, and J. Boike (2012). Subpixel heterogeneity of ice-wedge polygonal tundra: a multi-scale analysis of land cover and evapotranspiration in the Lena River Delta, Siberia. *Tellus B 64*.

Naumov, Y. (2004). *Soils and soil cover of Northeastern Eurasia*, pp. 161–183. Springer Verlag.

Nunez, M., J. Davies, and P. Robinson (1972). Surface albedo at a tower site in Lake Ontario. *Boundary-Layer Meteorology 3*(1), 77–86.

Oechel, W. and K. Van Cleve (1986). The role of bryophytes in nutrient cycling in the taiga. In *Forest ecosystems in the Alaskan taiga*, pp. 121–137. Springer.

Oechel, W. C. and B. Sveinbjörnsson (1978). *Primary production processes in Arctic bryophytes at Barrow, Alaska*, pp. 269–298. New York, USA: Springer.

Olthof, I., C. Butson, R. Fernandes, R. Fraser, R. Latifovic, and J. Orazietti (2005). Landsat ETM+ mosaic of northern Canada. *Canadian Journal of Remote Sensing 31*(5), 412–419.

Olthof, I. and R. Fraser (2007). Mapping northern land cover fractions using Landsat ETM+. *Remote Sensing of Environment 107*(3), 496–509.

Olthof, I., R. Latifovic, and D. Pouliot (2008). *Circa-2000 Northern Land Cover of Canada*. Ottawa, Canada: Natural Resources Canada.

Olthof, I., D. Pouliot, R. Fernandes, and R. Latifovic (2005). Landsat-7 ETM+ radiometric normalization comparison for northern mapping applications. *Remote Sensing of Environment 95*(3), 388–398.

Ozesmi, S. and M. Bauer (2002). Satellite remote sensing of wetlands. *Wetlands Ecology and Management 10*, 381–402.

Parry, M. L. (2007). *Climate Change 2007: Impacts, Adaptation and Vulnerability: Working Group I Contribution to the Fourth Assessment Report of the IPCC*, Volume 4. Cambridge, UK: Cambridge University Press.

Payne, R. (1972). Albedo of the sea surface. *Journal of Atmospheric Sciences 29*, 959–970.

Pflugmacher, D., O. Krankina, W. Cohen, M. Friedl, D. Sulla-Menashe, R. Kennedy, P. Nelson, T. Loboda, T. Kuemmerle, E. Dyukarev, et al. (2011). Comparison and assessment of coarse resolution land cover maps for Northern Eurasia. *Remote Sensing of Environment 115*(12), 3539–3553.

Ping, C.-L., M. H. Clark, and D. K. Swanson (2004). Cryosols in Alaska. In *Cryosols*, pp. 71–94. Springer.

Pitman, A. (2003). The evolution of, and revolution in, land surface schemes designed for climate models. *International Journal of Climatology 23*(5), 479–510.

Prigent, C., E. Matthews, F. Aires, and W. Rossow (2001). Remote sensing of global wetland dynamics with multiple satellite data sets. *Geophysical Research Letters 28*(24), 4631–4634.

Prowse, T. D., C. Furgal, B. R. Bonsal, T. W. Edwards, et al. (2009). Climatic conditions in northern Canada: past and future. *Ambio 38*(5), 257.

Qin, Z. and A. Karnieli (1999). Progress in the remote sensing of land surface temperature and ground emissivity using NOAA-AVHRR data. *International Journal of Remote Sensing 20*(12), 2367–2393.

Ramsey III, E. and S. Laine (1997). Comparison of Landsat Thematic Mapper and high resolution photography to identify change in complex coastal wetlands. *Journal of Coastal Research 13*(2), 281–292.

Rees, W. (1993). Infrared emissivities of Arctic land cover types. *International Journal of Remote Sensing 14*(5), 1013–1017.

Regmi, P., G. Grosse, M. C. Jones, B. M. Jones, and K. W. Anthony (2012). Characterizing post-drainage succession in thermokarst lake basins on the Seward Peninsula, Alaska with TerraSAR-X backscatter and Landsat-based NDVI data. *Remote Sensing 4*(12), 3741–3765.

Rietkerk, M., V. Brovkin, P. van Bodegom, M. Claussen, S. Dekker, H. Dijkstra, S. Goryachkin, P. Kabat, E. van Nes, et al. (2011). Local ecosystem feedbacks and critical transitions in the climate. *Ecological Complexity 8*(3), 223–228.

Riordan, B., D. Verbyla, and A. D. McGuire (2006). Shrinking ponds in subarctic Alaska based on 19502002 remotely sensed images. *Journal of Geophysical Research 111*(G04002).

Roach, J. K., B. Griffith, and D. Verbyla (2012). Comparison of three methods for long-term monitoring of boreal lake area using Landsat TM and ETM+ imagery. *Canadian Journal of Remote Sensing 38*, 427–440.

Roth, K. L., P. E. Dennison, and D. A. Roberts (2012). Comparing endmember selection techniques for accurate mapping of plant species and land cover using imaging spectrometer data. *Remote Sensing of Environment 127*, 139–152.

Roulet, N. T. and M. Woo (1986). Wetland and lake evaporation in the low Arctic. *Arctic and Alpine Research 18*(2), 195–200.

Rouse, W. R. (2000). The energy and water balance of high-latitude wetlands: Controls and extrapolation. *Global Change Biology 6*(S1), 59–68.

Rouse, W. R., E. M. Blyth, R. W. Crawford, J. R. Gyakum, J. R. Janowicz, B. Kochtubajda, H. G. Leighton, P. Marsh, L. Martz, and A. Pietroniro (2003). Energy and water cycles in a high-latitude, North-flowing river system. *Bulletin of the American Meteorological Society 84*, 73–87.

Rovansek, R. J., L. D. Hinzman, and D. L. Kane (1996). Hydrology of a tundra wetland complex on the Alaskan Arctic Coastal Plain, USA. *Arctic and Alpine Research 28*(3), 311–317.

Sachs, T., M. Giebels, J. Boike, and L. Kutzbach (2010). Environmental controls on CH_4 emission from polygonal tundra on the microsite scale in the Lena river delta, Siberia. *Global Change Biology 16*(11), 3096–3110.

Salmun, H., A. Molod, J. Albrecht, and F. Santos (2009). Scales of variability of surface vegetation: Calculation and implications for climate models. *Journal of Geophysical Research 114*(G2), G02007.

Schmid, H. (1994). Source areas for scalars and scalar fluxes. *Boundary-Layer Meteorology 67*(3), 293–318.

Schneider, J., G. Grosse, and D. Wagner (2009). Land cover classification of tundra environments in the Arctic Lena Delta based on Landsat 7 ETM+ data and its application for upscaling of methane emissions. *Remote Sensing of Environment 113*, 380–391.

Schubert, P., L. Eklundh, M. Lund, and M. Nilsson (2010). Estimating northern peatland CO_2 exchange from MODIS time series data. *Remote Sensing of Environment 114*(6), 1178–1189.

Schwamborn, G., V. Rachold, and M. Grigoriev (2002). Late quaternary sedimentation history of the Lena Delta. *Quaternary International 89*(1), 119–134.

Scott Pegau, W. and C. Paulson (2001). The albedo of Arctic leads in summer. *Annals of Glaciology 33*(1), 221–224.

Seekell, D. and M. Pace (2011). Does the Pareto distribution adequately describe the size-distribution of lakes? *Limnology and Oceanography 56*(1), 350–356.

Seekell, D. A., M. L. Pace, L. J. Tranvik, and C. Verpoorter (2013). A fractal-based approach to lake size distributions. *Geophysical Research Letters 40*(3), 517–521.

Serreze, M. C., D. H. Bromwich, M. P. Clark, A. J. Etringer, T. Zhang, and R. Lammers (2003). Large-scale hydro-climatology of the terrestrial Arctic drainage system. *Journal of Geophysical Research 108*(D2), 8160.

Serreze, M. C., J. E. Walsh, F. S. Chapin Iii, T. Osterkamp, M. Dyurgerov, V. Romanovsky, W. C. Oechel, J. Morison, T. Zhang, and R. G. Barry (2000). Observational of recent change in the Northern high-latitude environment. *Climatic Change 46*, 159–207.

Sheard, J. and D. Geale (1983). Vegetation studies at Polar Bear Pass, Bathurst Island, N.W.T. I. Classification of plant communities. *Canadian Journal of Botany 61*(6), 1618–1636.

Shi, Z. and K. Fung (1994). A comparison of digital speckle filters. In *Geoscience and Remote Sensing Symposium, 1994. IGARSS'94. Surface and Atmospheric Remote Sensing: Technologies, Data Analysis and Interpretation., International*, Volume 4, pp. 2129–2133. IEEE.

Smith, L., Y. Sheng, G. MacDonald, and L. Hinzman (2005). Disappearing Arctic lakes. *Science 308*(5727), 1429.

Smith, S. and M. Burgess (2002). *A digital database of permafrost thickness in Canada*. Ottawa, Canada: Geological Survey of Canada.

Smol, J. P. and M. S. V. Douglas (2007). Crossing the final ecological threshold in high Arctic ponds. *Proceedings of the National Academy of Sciences of the USA 104*, 12395–12397.

Snyder, W. C., Z. Wan, Y. Zhang, and Y.-Z. Feng (1998). Classification-based emissivity for land surface temperature measurement from space. *International Journal of Remote Sensing 19*(14), 2753–2774.

Soliman, A., C. Duguay, W. Saunders, and S. Hachem (2012). Pan-Arctic land surface temperature from MODIS and AATSR: Product development and intercomparison. *Remote Sensing 4*(12), 3833–3856.

Somers, B., G. P. Asner, L. Tits, and P. Coppin (2011). Endmember variability in spectral mixture analysis: A review. *Remote Sensing of Environment 115*(7), 1603–1616.

Sonntag, D. (1990). Important new values of the physical constants of 1986, vapour pressure formulations based on the ITS-90, and psychrometer formulae. *Zeitschrift für Meteorologie 40*(5), 340–344.

Stow, D. A., A. Hope, D. McGuire, D. Verbyla, and J. Gamond (2004). Remote sensing of vegetation and land-cover change in Arctic tundra ecosystems. *Remote Sensing of Environment 89*, 281–308.

Sturm, M., C. Racine, and K. Tape (2001). Climate change: Increasing shrub abundance in the Arctic. *Nature 411*(6837), 546–547.

Tallis, J. (1959). Studies in the biology and ecology of Rhacomitrium lanuginosum Brid.: II. Growth, reproduction and physiology. *The Journal of Ecology 47*(2), 325–350.

Tape, K., M. Sturm, and C. Racine (2006). The evidence for shrub expansion in Northern Alaska and the Pan-Arctic. *Global Change Biology 12*(4), 686–702.

Tarnocai, C., J. Canadell, E. Schuur, P. Kuhry, G. Mazhitova, S. Zimov, et al. (2009). Soil organic carbon pools in the northern circumpolar permafrost region. *Global Biogeochemical Cycles 23*(2), GB2023.

Tarnocai, C. and S. C. Zoltai (1988). *Wetlands of Arctic Canada*, Volume 15, pp. 27–54. Montreal, Canada: Polyscience Publications.

Thompson, C., J. Beringer, F. , and A. McGuire (2004). Structural complexity and land-surface energy exchange along a gradient from Arctic tundra to boreal forest. *Journal of Vegetation Science 15*, 397–406.

Thuillier, G., M. Hersé, D. Labs, T. Foujols, W. Peetermans, D. Gillotay, P. Simon, and H. Mandel (2003). The solar spectral irradiance from 200 to 2400 nm as measured by the SOLSPEC spectrometer from the ATLAS and EURECA missions. *Solar Physics 214*(1), 1–22.

Traore, P., A. Royer, and K. Goita (1997). Land surface temperature time series derived from weekly AVHRR GVI composite datasets: Potential and constraints for northern latitudes. *Canadian Journal of Remote Sensing 23*(4), 390–400.

Turner, M. G., R. H. Gardner, and R. V. O'neill (2001). *Landscape ecology in theory and practice: pattern and process*. New York, USA: Springer.

Ulrich, M., G. Grosse, S. Chabrillat, and L. Schirrmeister (2009). Spectral characterization of periglacial surfaces and geomorphological units in the Arctic Lena Delta using field spectrometry and remote sensing. *Remote Sensing of Environment 113*(6), 1220–1235.

Verpoorter, C., T. Kutser, and L. Tranvik (2012). Automated mapping of water bodies using landsat multispectral data. *Limnology and Oceanography: Methods 10*, 1037–1050.

Walker, D., M. Raynolds, F. Daniëls, E. Einarsson, A. Elvebakk, W. Gould, A. Katenin, S. Kholod, C. Markon, E. Melnikov, et al. (2005). The circumpolar Arctic vegetation map. *Journal of Vegetation Science 16*(3), 267–282.

Walker, D. A., H. E. Epstein, V. E. Romanovsky, C. L. Ping, G. J. Michaelson, R. P. Daanen, Y. Shur, R. A. Peterson, W. B. Krantz, and M. K. Raynolds (2008). Arctic patterned-ground ecosystems: A synthesis of field studies and models along a North American Arctic transect. *Journal of Geophysical Research 113*, G03S01.

Walter, K., S. Zimov, J. Chanton, D. Verbyla, and F. Chapin (2006). Methane bubbling from Siberian thaw lakes as a positive feedback to climate warming. *Nature 443*(7107), 71–75.

Wan, Z. (2008). New refinements and validation of the MODIS land-surface temperature/emissivity products. *Remote Sensing of Environment 112*(1), 59–74.

Wan, Z. and J. Dozier (1996). A generalized split-window algorithm for retrieving land-surface temperature from space. *Geoscience and Remote Sensing, IEEE Transactions on 34*(4), 892–905.

Wan, Z. and Z.-L. Li (1997). A physics-based algorithm for retrieving land-surface emissivity and temperature from EOS/MODIS data. *Geoscience and Remote Sensing, IEEE Transactions on 35*(4), 980–996.

Watts, J., J. Kimball, L. Jones, R. Schroeder, and K. McDonald (2012). Satellite Microwave remote sensing of contrasting surface water inundation changes within the Arctic–Boreal Region. *Remote Sensing of Environment 127*, 223–236.

Wegmuller, U. (1999). Automated terrain corrected SAR geocoding. In *Geoscience and Remote Sensing Symposium, 1999. IGARSS'99 Proceedings. IEEE 1999 International*, Volume 3, pp. 1712–1714. IEEE.

Weiss, D. and R. Crabtree (2011). Percent surface water estimation from MODIS BRDF 16-day image composites. *Remote Sensing of Environment 115*(8), 2035–2046.

Werner, C., U. Wegmüller, T. Strozzi, and A. Wiesmann (2000). Gamma SAR and interferometric processing software. In *Proceedings of the ERS-ENVISAT Symposium, Gothenburg, Sweden*, pp. 16–20.

Westermann, S., M. Langer, and J. Boike (2011). Spatial and temporal variations of summer surface temperatures of high-arctic tundra on Svalbard-Implications for MODIS LST based permafrost monitoring. *Remote Sensing of Environment 115*(3), 908–922.

Westermann, S., M. Langer, and J. Boike (2012). Systematic bias of average winter-time land surface temperatures inferred from MODIS at a site on Svalbard, Norway. *Remote Sensing of Environment 118*, 162–167.

White, D., L. Hinzman, L. F. Alessa, Smith, et al. (2007). The Arctic freshwater system: Changes and impacts. *Journal of Geophysical Research 112*(G4), G04S54.

Wolfe, R. E., M. Nishihama, A. J. Fleig, J. A. Kuyper, D. P. Roy, J. C. Storey, and F. S. Patt (2002). Achieving sub-pixel geolocation accuracy in support of MODIS land science. *Remote Sensing of Environment 83*(1), 31–49.

Woo, M.-K. (2012). Northern Wetlands. In *Permafrost Hydrology*, pp. 347–406. Springer.

Woo, M.-K., D. Kane, S. Carey, and D. Yang (2008). Progress in permafrost hydrology in the new millennium. *Permafrost and Periglacial Processes 19*, 237–254.

Woo, M.-K. and K. Young (2006). High Arctic wetlands: Their occurrence, hydrological characteristics and sustainability. *Journal of Hydrology 320*(3-4), 432–450.

Yoshikawa, K. and L. D. Hinzman (2003). Shrinking thermokarst ponds and groundwater dynamics in discontinuous permafrost near Council, Alaska. *Permafrost and Periglacial Processes 14*, 151–160.

Young, K., Assini, A. J., Abnizova, and E. Miller (2013). Snowcover and melt characteristics of upland/lowland terrain: Polar Bear Pass, Bathurst Island, Nunavut, Canada. *Hydrology Research 44*(1), 2–20.

Young, K. and C. Labine (2010). Summer hydroclimatology of an extensive low-gradient wetland: Polar Bear Pass, Bathurst Island, Nunavut, Canada. *Hydrology Research 41*(6), 492–502.

Zhang, X., L. A. Vincent, W. Hogg, and A. Niitsoo (2000). Temperature and precipitation trends in Canada during the 20th century. *Atmosphere-Ocean 38*(3), 395–429.